UNIVERSITY OF CALIFORNIA

Los Angeles

High-throughput Quantitative Phase Imaging for Characterization of Organoid Growth, Drug Responses, and Heterogeneity

A dissertation submitted in partial satisfaction of the

requirements for the degree Doctor of Philosophy

in Bioengineering

by

Bowen Wang

2025

ABSTRACT OF THE DISSERTATION

High-throughput Quantitative Phase Imaging for Characterization of Organoid Growth, Drug Responses, and Heterogeneity

by

Bowen Wang

Doctor of Philosophy in Bioengineering

University of California, Los Angeles, 2025

Professor Michael A. Teitell, Chair

Functional precision medicine (FPM) in cancer is an emerging treatment paradigm involving exposure of patient-derived tumor material to drugs to assess their efficacy and to guide therapeutic selection. Tumor organoids, in addition to being versatile disease models for basic and translational research, are of particular interest for FPM applications. However, improved approaches for high-throughput drug screening of three-dimensional (3D) tumor organoids, capable of resolving both population-level and single organoid–level data and allowing for consideration of heterogeneity in drug screening readouts, are needed. Quantitative phase imaging (QPI) is a label-free microscopy technique for imaging optically transparent biological samples and quantifying various biophysical properties such as cell biomass, mass density, and growth. This thesis demonstrates a new application of high-speed live cell interferometry (HSLCI), a high-throughput QPI platform, for screening 3D-cultured organoid models of cancer, and describes the development of this method. The method presented combines bioprinting, HSLCI, and machine learning technologies to enable accurate, label-free, and highly time-resolved

biomass measurements of thousands of organoids in parallel, and rapid identification of drug sensitivity and resistance with temporal monitoring and single-organoid resolution. The complete QPI-based organoid screening pipeline can be leveraged for fundamental studies of disease biology, in addition to FPM studies aiming to establish clinical correlations and ultimately improve treatment selection for patients with solid cancers.

The dissertation of Bowen Wang is approved.

Alice Soragni

Pei-Yu Chiou

Jian Yu Rao

Michael A. Teitell, Committee Chair

University of California, Los Angeles

2025

DEDICATION

To my parents, for teaching me to value education and work ethic, and

for sacrificing so that I could pursue the most exciting opportunities the world has to offer;

To my professors, mentors, collaborators, and coworkers in lab, for their guidance and insight;

And to my friends who have always had my back over many years and

many games of *Super Smash Bros. Melee* (Nintendo GameCube, 2001),

for their support during my most challenging moments.

Table of Contents

List of Figures

Chapter 2

Acknowledgements

Chapter 2 is a reprinted version of a published manuscript by Peyton J. Tebon*, Bowen Wang*, Alexander L. Markowitz*, Ardalan Davarifar, Brandon L. Tsai, Patrycja Krawczuk, Alfredo E. Gonzalez, Sara Sartini, Graeme F. Murray, Huyen Thi Lam Nguyen, Nasrin Tavanaie, Thang L. Nguyen, Paul C. Boutros, Michael A. Teitell, and Alice Soragni. “Drug screening at single-organoid resolution via bioprinting and interferometry.” *Nat. Commun.* **14**, 3168 (2023). (DOI: https://doi.org/10.1038/s41467-023-38832-8). P.J.T., B.W., and A.L.M. contributed equally. P.J.T., B.W., M.A.T., and A.S. conceived the project and designed the study; P.J.T, B.W, N.T., and A.S. developed the bioprinting protocol; P.J.T., B.W, S.S., H.T.L.N., and N.T. performed cell experiments; B.W., G.F.M., and T.L.N. built the HSLCI instrument; A.L.M. and B.L.T. analyzed RNAseq data; A.D. and P.K. helped with image segmentation; A.L.M. and P.J.T. adapted and tested the organoid classifier; P.J.T., B.W., A.M., and A.E.G. developed code; P.J.T., B.W., and A.E.G. developed and ran the data analysis pipeline; P.J.T., B.W., A.L.M., B.L.T., and A.S. assembled figures; P.J.T., B.W., A.L.M., P.C.B., M.A.T., and A.S. wrote the manuscript with contributions from all authors; M.A.T., and A.S. supervised the project. We thank the UCLA Translational Pathology Core Laboratory and the UCLA Technology Center for Genomics and Bioinformatics for their assistance with this work, and Dr. Steven Jonas for his generous access to laboratory equipment.

This work was supported by NIH R01CA244729 and R01CA244729-03S1 (to A.S. and P.C.B.) a JCCC Fellowship (to P.J.T.), a National Science Foundation Graduate Research Fellowship (DGE-2034835, to B.W.), a Eugene V. Cota Robles Fellowship (to B.W.) a UCLA DGSOM Seed Award (to A.S. and P.C.B.), the Air Force Office of Scientific Research (FA9550-15-1-0406, to M.A.T.), the Department of Defense (W81XWH2110139, to M.A.T.). It was additionally supported by NIH U24CA248265 (to P.C.B.) and NIH R01GM114188, R01GM073981, R01CA185189, R21CA227480, R01GM127985, and P30CA016042 (to M.A.T.).

Chapter 3 is a version of a manuscript currently in review, by Bowen Wang, Peyton J. Tebon, Thang L. Nguyen, Graeme F. Murray, Daniel C. Guest, Jason Reed, Alice Soragni, and Michael A. Teitell. “Label-free interferometry platform for drug response profiling of bioprinted tumor organoids at single-organoid resolution.” *Nat. Protoc.* (2025). B.W., P.J.T., A.S., and M.A.T. conceived the project and designed the study; B.W, P.J.T., and A.S. developed the bioprinting protocol; B.W. and P.J.T. performed cell experiments; D.C.G. and J.R. designed the HSLCI instrument; B.W., G.F.M., and T.L.N. built the HSLCI instrument; B.W. and P.J.T. developed code; P.J.T. adapted and tested the organoid classifier; B.W. and P.J.T. developed and tested the data analysis pipeline; B.W. and P.J.T. assembled figures; B.W., P.J.T., T.L.N., G.F.M., A.S., and M.A.T. wrote the manuscript with contributions from all authors; A.S. and M.A.T. supervised the project. We would like to thank Dr. Kevin Leslie and Dr. Dian Huang for their prior contributions in testing the imaging scripts and workflow upon which ours was built. We would also like to thank Dr. Steven Jonas for generously allowing access to laboratory equipment.

This work was supported by the Air Force Office of Scientific Research (FA9550-15-1-0406, to M.A.T.), the Department of Defense (W81XWH2110139, to M.A.T.), a National Science Foundation Graduate Research Fellowship (DGE-2034835, to B.W.), a Eugene V. Cota Robles Fellowship (to B.W.), a JCCC Fellowship (to P.J.T.), and a UCLA DGSOM Seed Award (to A.S.). It was additionally supported by NIH T32HL144449 (to T.L.N.), R01CA244729 (to A.S.), R01CA244729-03S1 (to A.S.), NIH R01GM114188 (to M.A.T.), R01GM073981 (to M.A.T.), R01CA185189 (to M.A.T.), R21CA227480 (to M.A.T.), R01GM127985 (to M.A.T.), and P30CA016042 (to M.A.T.).

Vita

Education

University of California, Los Angeles — Los Angeles, CA
Henry Samueli School of Engineering and Applied Science
Master of Science in Bioengineering — December 2020

University of California, Berkeley — Berkeley, CA
College of Engineering
Bachelor of Science in Bioengineering — December 2017
High honors

Fellowships

NSF Graduate Research Fellowship, National Science Foundation — 2019 – 2022

Eugene V. Cota-Robles Fellowship, UCLA — 2018 – 2019; 2022 – 2023

Publications and Proceedings

Wang, B., Tebon, P. J., Nguyen, T. L., Murray, G. F., Guest, D. C., Reed, J., Soragni, A., & Teitell, M. A. (2025). Label-free interferometry platform for drug response profiling of bioprinted tumor organoids at single-organoid resolution. *Nature Protocols*, in review.

Tebon, P. J.*, **Wang, B.***, Markowitz, A. L.*, Davarifar, A., Tsai, B. L., Krawczuk, P., Gonzalez, A. E., Sartini, S., Murray, G. F., Nguyen, H. T. L., Tavanaie, N., Nguyen, T. L., Boutros, P. C., Teitell, M. A., & Soragni. A. (2023). Drug screening at single-organoid resolution via bioprinting and interferometry. *Nature Communications*, **14**, 3168. https://doi.org/10.1038/s41467-023-38832-8

Wang, B., Tebon, P. J., Markowitz, A. L., Murray, G. F., Nguyen, H. T. L., Tavanaie, N., Nguyen, T. L., Boutros, P. C., Soragni, A., & Teitell, M. A. (2022). Functional Drug Sensitivity Screening of Bioprinted Tumor Organoids using High-Speed Live Cell Interferometry. In *2022 Conference on Lasers and Electro-Optics (CLEO)* (pp. 1-2). IEEE.

*Authors contributed equally

Presentations

Wang, B., Tebon, P. J., Markowitz, A. L., Davarifar, A., Tsai, B. L., Krawczuk, P., Gonzalez, A. E., Sartini, S., Murray, G. F., Nguyen, H. T. L., Tavanaie, N., Nguyen, T. L., Boutros, P. C., Soragni, A., & Teitell, M. A. (2023, May 2). High-speed live cell interferometry for functional drug sensitivity screening of bioprinted tumor organoids. [Poster Presentation]. 2023 Jonsson Comprehensive Cancer Center Retreat, UCLA, Los Angeles, CA, United States.

Wang, B., Tebon, P. J., Markowitz, A. L., Davarifar, A., Tsai, B. L., Krawczuk, P., Gonzalez, A. E., Sartini, S., Murray, G. F., Nguyen, H. T. L., Tavanaie, N., Nguyen, T. L., Boutros, P. C., Soragni, A., & Teitell, M. A. (2023, February 10). High-speed live cell interferometry for functional drug sensitivity screening of bioprinted tumor organoids. [Poster Presentation]. 2023 Bioengineering Research Day, UCLA, Los Angeles, CA, United States.

Wang, B. (2022, August 21–25). High-speed live cell interferometry for functional drug sensitivity screening of bioprinted tumor organoids. [Conference Presentation]. In *Interferometry XXI* (Vol. 12223, p. 122230C). SPIE Optics and Photonics 2022, San Diego, CA, United States. https://doi.org/10.1117/12.2632405

Wang, B. (2022, May 15–20). Functional Drug Sensitivity Screening of Bioprinted Tumor Organoids using High-Speed Live Cell Interferometry. [Conference Presentation]. 2022 Conference on Lasers and Electro-Optics (CLEO), San Jose, CA, United States.

Patents

Soragni, A., Tebon, P. J., Lin, L., Tavanaie, N., **Wang, B.**, & Teitell, M. A. (2020). “Tissue organoid bioprinting and high-throughput screening methodology.” U.S. Patent Application No. 18/037,646. U.S. Patent and Trademark Office.

Chapter 1: Introduction

Precision cancer medicine is an emerging therapeutic paradigm that aims to match each unique patient with the anti-cancer treatments that are best for them on an individualized basis[1,2]. Precision oncology has traditionally involved sequencing patients' tumors, with the premise that the somatic genetic alterations that are known to drive multistep cancer progression[3] correspond to molecular vulnerabilities that can potentially be targeted to benefit those patients[2,4]. However, previous efforts in screening cancer genomes have only found a limited number of actionable genetic alterations[1,2,4–6], and recent underwhelming results using the genomic precision medicine approach have demonstrated that genomic analyses are insufficient for informing clinical decisions for most patients with cancer[1,2,5–9]. Identifying and validating unique predictive biomarkers to improve therapy selection remains an important clinical need in many disease contexts[1,10–12].

Unlike traditional genomics-based precision medicine approaches to treating cancer, functional precision medicine (FPM) involves *ex vivo* testing of patient-derived tumor material with drug treatments to assess their responses and predict drug efficacy[1,2]. FPM is a compelling approach to individualized treatment selection because FPM strategies are not necessarily limited to static measurements of initial conditions and do not require prior knowledge of the molecular features of each patient's unique disease[1,2,13]. Furthermore, the contribution of nongenetic phenotypic plasticity to drug response heterogeneity among cancer cells[1,6,14] suggests that compared to genomic approaches, functional drug response profiling could provide readouts with greater relevance for optimizing treatment selection[1,2]. While recent advances have encouragingly culminated in the first prospective FPM clinical trials showing that *ex vivo* functional drug testing could guide therapy for patients with advanced hematologic malignancies[13,15], there remains a critical need to develop and validate additional and

improved FPM approaches to improve therapeutic outcomes for more individuals with cancer, and particularly for patients with solid cancers[1,2].

Organoids are multicellular structures derived from cells of high proliferative potential, either adult stem cells or cancer cells, cultured within a three-dimensional (3D) biomimetic matrix such that they recapitulate the 3D architecture and physiology of the source tissue[16–19]. 3D organoid models of cancer are promising tools that are becoming widely used for drug discovery[18–26] and precision medicine[18,19,22–29]. While high-throughput compound screening for drug discovery has traditionally used cancer cell line models cultured in two-dimensional (2D) monolayers[18,21,30], cells cultured in 2D fail to recapitulate the 3D organization and cellular relationships observed *in vivo* in solid tumors, limiting the utility and predictive potential of assay results[21,24,30–33]. 2D cancer cell line models are additionally unsuitable for FPM applications because establishment of primary cell lines from patient tumors is highly inefficient[18,25,34,35]. Contrastingly, tumor organoids can be derived quickly and readily from cell lines[36,37] or small samples of primary patient material[18,19,23–28,38]. Analogously to using cancer cell line models, tumor organoid models can also easily be expanded *in vitro*, cultured long-term, cryopreserved, or subjected to experimental manipulations[18,24–26]. Evidence is mounting that the results of functional drug response assays on individualized patient-derived tumor organoid (PDTO) models of solid cancers are concordant with patients' responses to drug treatments[27,28,39–43], and could potentially be used as predictive biomarkers[29,44]. Development and validation of improved high-throughput FPM approaches compatible with tumor organoid models has enormous potential to benefit many additional patients with cancer[1,2].

Quantitative phase imaging (QPI) is a set of label-free optical microscopy techniques, including but not limited to phase-shifting interferometry, wavefront sensing, digital holographic microscopy, and differential phase contrast microscopy, which can be used to quantify the biophysical properties and behaviors of cells, tissues, and other transparent

biological samples by measuring the phase shift of light as it passes through these materials[45–48]. This phase shift represents the difference in optical path length caused by the presence of the sample of interest, and is given by the following equation (1):

$$\phi = \frac{2\pi}{\lambda}\int_{z=0}^{h}[n(z) - n_{medium}]dz \quad (1)$$

where Φ is the measured phase shift in radians, λ is the illumination wavelength, $n(z)$ is the refractive index of the sample as a function of height, n_{medium} is the refractive index of the surrounding medium, and integration is performed across the height h of the sample in the z direction, which is the direction of light propagation[45–47]. The refractive indices of mammalian cells and their constituent biomolecules have been demonstrated to be linearly proportional with concentration, with the proportionality constant α known as the specific refractive increment[46,47,49,50]. Because the specific refractive increments of the proteins, nucleic acids, and sugars that make up most of a cell's dry biomass fall within a narrow range[46,50–53], α can be assumed to have an average value of 1.8×10^{-4} m^3/kg[46,50–53], and the measured phase shift Φ can be used to calculate the dry mass content of the sample, using the following equation (2):

$$m = \frac{\lambda}{2\pi\alpha}\int \phi \, dA \quad (2)$$

where m is dry biomass and integration is performed over the area A of imaged objects[45–47].

QPI has been utilized in many biomedical studies for measurements of various characteristics and behaviors of cells of interest, including cell size, morphology, motion, viscoelasticity, biomass accumulation or loss, and responses to experimental perturbations such as drug treatments[45–48]. It is of interest for applications in FPM because repeated, time-resolved QPI measurements can quantify increases in cell biomass during cell growth[54–57] or the characteristic decreases in cell biomass that occur during cell death[58–61]; both are direct indicators of cell fitness, as changes in biomass accumulation dynamics depend on the balance of anabolic and catabolic cellular processes[45]. Time-resolved biomass measurements showing growth or

responses to drug treatments are especially intriguing for FPM because they enable resolution of more subtle changes in biological activity than traditional endpoint viability assays[2,62–66], and treatment-induced changes in growth rates *in vitro* are relevant to the clinical acquisition of drug resistance in patients with cancer[67–70]. Additionally, QPI is capable of obtaining growth and drug response data from single cells or cell clusters, and therefore can resolve sample heterogeneity within cancer models[46,58,66,71–74].

The advance in QPI technology foundational to this thesis is high-speed live cell interferometry (HSLCI), a high-throughput imaging platform which uses repeated, time-resolved QPI to longitudinally track biomass accumulation dynamics in thousands of discrete cells or cell clusters, with picogram sensitivity[66,71,74–76]. HSLCI was developed with the goal of increasing the throughput, time resolution, and number of cells or cell clusters imaged in each imaging experiment, to maximize the utility of high-content QPI data for drug screening and informing subsequent therapeutic decisions[66,71]. HSLCI has previously been used to identify rare drug-resistant outlier cells among heterogeneous populations of melanoma or lymphoma cells within hours of treatment[66,73], and to confirm concordance between *in vitro* and *in vivo* biomass growth rates of patient-derived xenograft (PDX) models of breast cancer in response to drug treatments, demonstrating its potential as a functional assay for screening drug efficacy[71]. Although the characteristics described make HSLCI uniquely suited for FPM using organoids, high throughput imaging–based drug screening of organoids is technically challenging[21,77,78]. This doctoral thesis describes the development and adaptation of the high-speed live cell interferometry platform toward high-throughput biomass profiling and drug screening of organoid models of cancer and explores the future directions of this method and its potential to influence treatment decisions.

Chapter 2: Drug screening at single-organoid resolution via bioprinting and interferometry

Introduction

Functional approaches in precision oncology entail exposing tumor cells to therapeutic interventions to identify drug candidates and to rapidly assess the potential efficacy of drugs for individual patients and therapy selection[2,22,27,39,79–82]. While a small number of actionable mutations are known, the majority of newly-diagnosed tumors lack any currently actionable genomic alteration[7]. By directly measuring the effect of drugs on tissues or cells, functional precision medicine methods can inform on the therapeutic resistance and sensitivity landscape of tumors without requiring full knowledge of the underlying molecular vulnerabilities a priori[13,15,20,27,39,79,82–86].

The broadly adopted model systems for screening assays each have limitations. Two-dimensional (2D) cell lines are relatively simple and inexpensive to culture but fail to represent the architecture, behavior, and drug response of native tissue[31,32,87,88]. Mouse models have additional complexity but carry inherent, species-specific variations that limit their translation to human patients[89,90]. Patient-derived xenograft (PDX) models aim to better recapitulate human cancers yet are still constrained by the large cost and time associated with their use which translates to the impracticality of performing large drug screenings[2,91,92]. Three-dimensional (3D) tumor organoids are promising models for precision medicine that can be established rapidly and effectively from a variety of cell lines[36,37] and tissue sources[18,24], and accurately mimic a patient's response to therapy[18,23–25,27,39,81–85,93]. They are physiologically-relevant, personalized cancer models well-suited for drug development and clinical applications[18,24,25,81]. We previously developed a screening platform that takes advantage of patient-derived tumor organoids seeded in a mini-ring format to automate high throughput drug testing, with results available within one

week from surgery[20,27,38]. The key outstanding limitations to the broad adoption of organoid-based screenings remain the time-intensive and operator-to-operator susceptibility of the cell seeding steps as well as destructive, population-level approaches required for subsequent organoid analysis[21,94].

To overcome these limitations, we developed an organoid screening approach that combines automated cell seeding via bioprinting with high-speed live cell interferometry (HSLCI) for non-invasive, label-free, time-resolved imaging. Bioprinting, a technique for precise, reproducible deposition of cells in bioinks onto solid supports, is rapidly gaining traction in cancer biology[95–99]. Within the deposited bioink, embedded cells can interact with physiological microenvironment components[94]. We then use HSLCI, a type of quantitative phase imaging (QPI)[66,71,73,100,101], to rapidly monitor changes in dry biomass and biomass distribution of single organoids over time. The HSLCI measures the phase shift of light transmitted through the sample which is used to calculate the mass density of each organoid[45,46]. Biomass is an important metric of organoid fitness as its dynamics are the direct result of biosynthetic and degradative processes within cells[45,46]. HSLCI uses a wavefront sensing camera to enable reconstruction of the phase shift of light as it passes through a cell and interacts with matter[45,46,100]. Due to the defined linear relationship between the mass density and refractive index of biomolecules in solution, which is invariant with respect to changes in cellular content[50,51,102–104], measured phase shifts can be integrated across the area of an image and multiplied by a conversion factor to obtain the dry biomass density of imaged cells[45,46]. This conversion factor is the inverse of the specific refractive increment, defined as the slope of the relationship between the refractive index and mass concentration of a solution[45,46,51]. QPI measurements of biomass changes allowed resolution of drug-resistant and drug-sensitive cells in 2D cell culture models within hours of treatment[54,56,59,66,71,73,75,105]. HSLCI-measured response profiles matched drug sensitivity from PDX mouse models of breast cancer[71]. However, HSLCI has so far been applied exclusively to

screening of cancer cell lines grown in 2D or single-cell suspensions of excised PDX tumors[66,71,73,101].

Here, we introduce a comprehensive pipeline that combines bioprinting, HSLCI, and machine learning-based organoid tracking and classification. Using cell lines as a model for 3D tumor cell growth, we demonstrate that bioprinted cells deposited in uniform, flat layers of extracellular matrix allow label-free, time-resolved, non-destructive quantification of growth patterns and drug responses at single-organoid resolution.

Results

Bioprinting enables seeding cells in Matrigel in suitable geometries for quantitative imaging applications.

To address current limitations[20,27,38] and facilitate non-invasive, label-free imaging of 3D organoids by HSLCI, we created an automated cell printing protocol using an extrusion bioprinter. As a base, we used an organoid screening platform in which organoids are grown from cells seeded in mini-rings of Matrigel around the rim of 96-well plates, with the empty center allowing the use of automated liquid handlers, facilitating media exchanges and addition of perturbagens[20,27,38,93]. We retained the empty center architecture but altered the geometry to bioprint mini-squares of cells in Matrigel (**Figure 2.1A**). Positioning the sides of the square in the HSLCI imaging path allows sampling of a larger area and limits imaging artifacts caused by uneven illumination at well edges[100] (**Figure 2.1A**). Our bioprinting protocol entails suspending cells in a bioink consisting of a 3:4 ratio of medium to Matrigel. We then transferred this material to a print cartridge, incubated at 17 °C for 30 minutes, and bioprinted into each well at a pressure between 7 and 15 kPa, resulting in <200 μm prints on standard glass-bottom plates (**Figure 2.1B**).

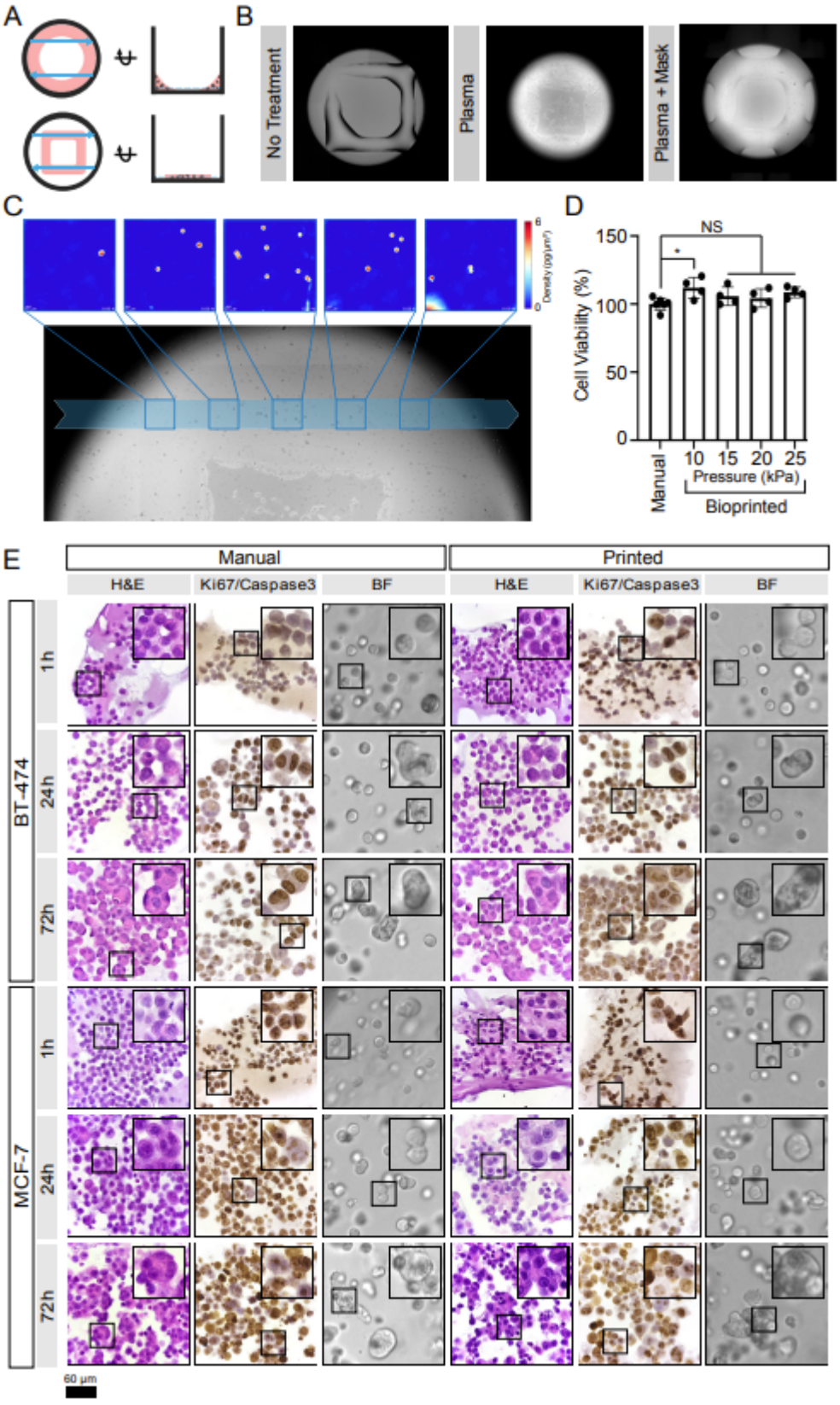
A
B
No Treatment
Plasma
Plasma + Mask
C
D
NS
*
Cell Viability (%)
150
100
50
0
Manual
10
15
20
25
Pressure (kPa)
Bioprinted
E
Manual
Printed
H&E
Ki67/Caspase3
BF
BT-474
MCF-7
1h
24h
72h
60 µm

Figure 2.1: Bioprinting enables the seeding of Matrigel-encapsulated cells optimized for efficient high-speed live cell interferometry (HSLCI). (A) Schematic of wells with mini-rings (top) and mini-squares (bottom) relative to HSLCI imaging path (blue arrows). The top views (left) demonstrate that transitioning from rings to squares increases the area of material in the HSLCI imaging path. The side views (right) show that organoids in the square geometry align to a single focal plane better than organoids in a ring. **(B)** Plasma treatment of the well plate prior to printing optimizes hydrogel construct geometry. Bioprinting Matrigel onto untreated glass (left) generates thick (~ 200 µm) constructs that decreases the efficiency of organoid tracking by increasing the number of clusters out of the focal plane. Whole well plasma treatment (middle) increases the hydrophilicity of all well surfaces causing the Matrigel to spread thin (~ 50 µm) over the surface; however, the increased hydrophilicity also draws bioink up the walls of the well. Plasma treatment with a well mask facilitates the selective treatment of a desired region of the well (right). This leads to optimal constructs with a uniform thickness of approximately 75 µm across the imaging path. **(C)** Individual organoids can be tracked over time across imaging modalities. Five representative HSLCI images are traced to the imaging path across a brightfield image. **(D)** Cell viability of printed versus manually seeded MCF-7 cells in a Matrigel-based bioink, 1 h after plating. Data are presented as mean values ± SD. A one-way ANOVA was performed ($n = 4$, $p = 0.0605$) with post-hoc Bonferroni's multiple comparisons test to compare all bioprinted conditions against the manually seeded control. Adjusted p-values were 0.0253, 0.6087, >0.9999, 0.1499 for print pressures 10, 15, 20, 25 kPa, respectively. **(E)** H&E staining shows the development of multicellular organoids over time regardless of seeding method. The prevalence and size of multicellular structures increases with culture time. Ki-67/Caspase-3 staining demonstrates that most cells remain in a proliferative state throughout culture time. While some apoptotic cells were observed in organoids cultured for 72 hours, the majority of cells show strong Ki-67 positivity. Ki-67 is stained brown, and Caspase-3 is stained pink. Scale bar is 60 µm. Source data is provided as a Source Data file.

We next coupled bioprinted cell lines grown in 3D clusters to an HSLCI platform. HSLCI uses a wavefront sensing camera and a dynamic focus stabilization system to perform continuous, high throughput, label-free, QPI of biological samples, tracking their biomass changes over time[66,71]. However, efficient high throughput QPI of 3D organoids using HSLCI is hindered by geometry considerations; when an object of interest is out of focus, measured phase shifts cannot be assumed to maintain a direct relationship with mass density[100]. Thus, we attempted to generate thinner layers of Matrigel to yield a relatively greater number of organoids in focus that can be quantitatively assessed at any given time. To generate thinner (<100 µm) constructs amenable to

efficient, label-free HSLCI imaging, we increased the hydrophilicity of the surface of 96-well glass-bottom plates by oxygen plasma treatment[106]. We developed 3D masks composed of BioMed Amber Resin (FormLabs) to selectively functionalize the region of interest (**Figure S2.1A–C**). Bioprinting post-plasma treatment generated uniform mini-squares with organoids closely aligned on a single focal plane at ~70 µm thickness (**Figure 2.1B**). The printed structures are consistent (**Figure S2.1D**) and amenable to massively parallel QPI by HSLCI as we aligned the legs of the bioprinted mini-square construct with the HSLCI imaging path (**Figure 2.1C**).

Lastly, we verified that the printing parameters used did not alter cell viability by directly comparing MCF-7 cells manually seeded according to our established protocol[20,27,38] to cells printed through a 25 gauge needle (260 µm inner diameter) using extrusion pressures ranging from 10 to 25 kPa. We did not observe any reduction in cell viability as measured by ATP release assay (**Figure 2.1D**). These results are consistent with the existing literature as reductions in cell viability are often associated with higher print pressures (50–300 kPa)[107,108]. Taken together, this describes a method for bioprinting layers suitable for HSLCI imaging without impacting cell viability, while supporting automated liquid-handling for high throughput applications[20,27,38,109,110].

Bioprinted tumor cells maintain histological features of manually seeded 3D cultures.

To verify that bioprinting did not perturb tumor biology, we directly compared the histology and immunohistochemical profiles of bioprinted and hand-seeded cells from two breast cancer cell lines, BT-474 and MCF-7. These lines were selected for their differing molecular features such as their human epidermal growth factor receptor 2 (HER2) and estrogen receptor (ER) status[35,111]. We grew organoids from cells seeded in maxi-rings (1×10^5 cells/ring) to obtain sufficient material for downstream characterization. Cells were either manually seeded into 24 well plates[20,27,38] or bioprinted into 8-well plates at an extrusion pressure of 15 kPa. The bioprinted cells and cell clusters were morphologically indistinguishable from manually seeded ones in brightfield images

and hematoxylin and eosin (H&E)-stained sections taken 1, 24, and 72 hours after cell seeding (**Figure 2.1E**). Both bioprinted and manually seeded cell clusters grew in size over time and bioprinting did not alter their proliferation rates (Ki-67 staining) or apoptosis (cleaved caspase-3; **Figure 2.1E**). Hormone receptor status was in agreement with literature reports for both cell types[35,112–114] and unaltered between bioprinted and manually seeded cells as shown by immunohistochemistry (IHC) for HER2 and ER (**Figure S2.2**). Chaperone protein expression also remained consistent with manually printed cells (**Figure S2.3**). Thus, bioprinting did not influence histology for the tested cell types.

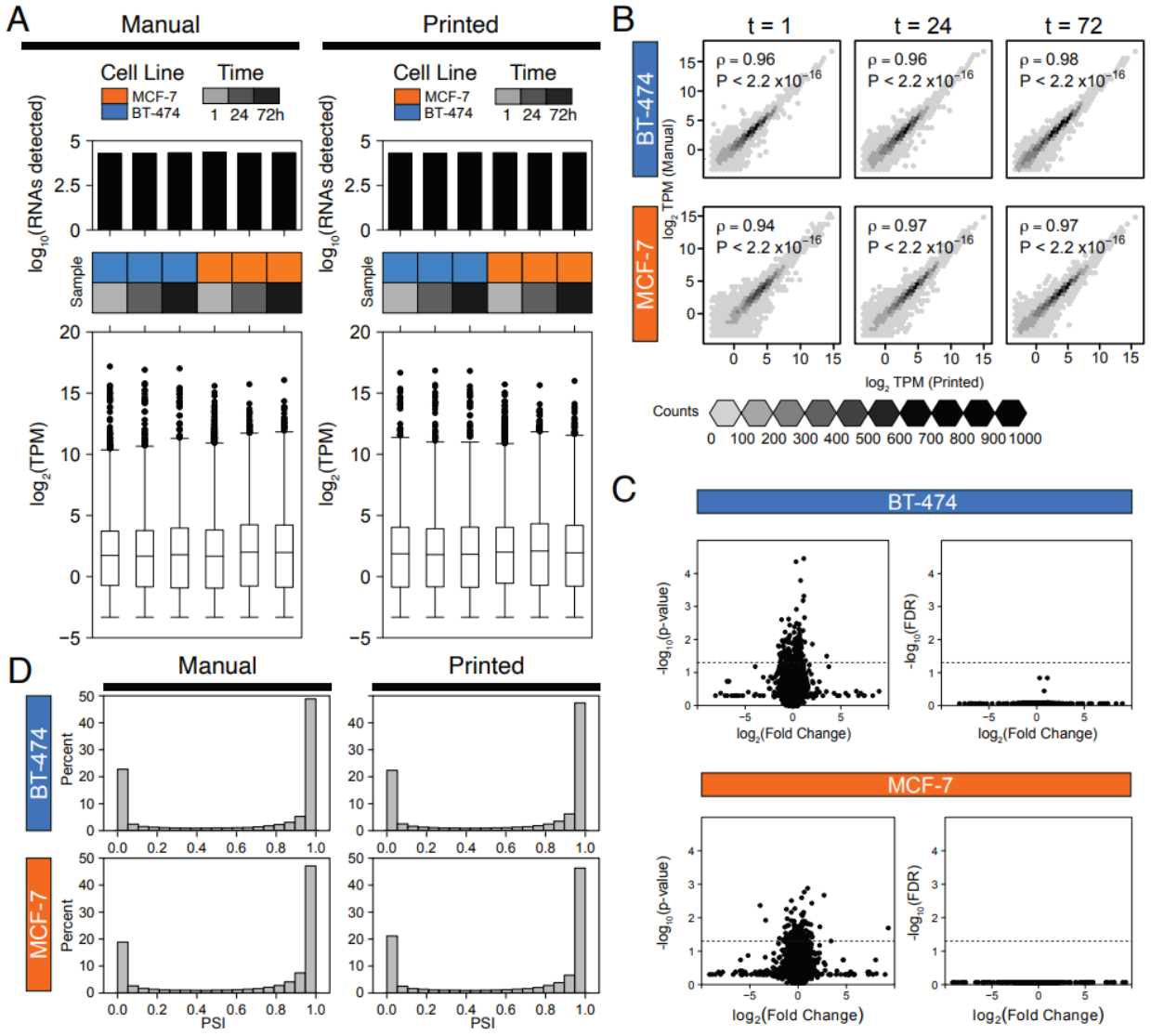

Figure 2.2: Bioprinting does not significantly alter transcriptomes. (A) Distributions of total number of RNAs detected (above) and RNA abundance (below) measured as transcripts per million (TPM) are similar between manually seeded (left) and bioprinted (right) cells. $n = 30,544$ transcripts were assessed across two independent experiments. Boxplot centers represent each median, edges of the boxes represent the 25th and 75th quartiles, whiskers represent the range of the data, and individually plotted points are outliers greater than 1.5 times the interquartile range from the median. **(B)** Spearman's rank correlation of RNA abundance of manually seeded and bioprinted cell line 3D models at three time points (t = 1, 24, and 72 hours post-seeding). We found strong correlations between RNA abundance in manually seeded and bioprinted cells for both cell lines. *p*-values are derived from a two-tailed test of correlation between paired samples. **(C)** Volcano plots of paired, two-tailed t-test results comparing the RNA abundance of manually seeded and bioprinted MCF-7 and BT-474 with unadjusted *p*-values (left) and false discovery rate (FDR) adjusted *p*-values (right). No transcripts were preferentially expressed based upon the seeding method for either cell line ($n = 0$ out of 30,544 genes, FDR < 0.05, t-test). **(D)** Distribution of percent spliced in (PSI) exons are similarly distributed among BT-474 (top) and MCF-7 (bottom). The distribution of PSI is similar between manually seeded (left) and bioprinted (right) cells. PSI of 1 indicates that the exon is exclusively included, while a PSI of 0 indicates that the exon is exclusively excluded. Source data is provided as a Source Data file.

Bioprinted and manually seeded cells are molecularly indistinguishable.

While bioprinted cells are histologically indistinguishable from manually seeded ones, this does not preclude molecular changes caused by the printing process. We therefore performed a detailed analysis of the transcriptomes of manually seeded and bioprinted cells 1, 24 and 72 hours post-seeding. By pooling RNA sequencing (RNAseq) data across two independent experiments, we assessed the distributions of 30,544 RNA transcripts and found no significant differences between seeding approaches (**Figure 2.2A**). The overall transcriptomes of manually seeded and bioprinted cells were highly correlated (**Figure 2.2B**), with no individual transcripts differing significantly in abundance for either cell line (FDR < 0.05, *t*-test; **Figure 2.2C**).

We next examined pre-mRNA alternative splicing events since these can induce functional changes even in the absence of variations in mRNA levels[115–117]. We found that the density of exon-inclusion and exon-skipping isoforms was unchanged (**Figure 2.2D**). Similarly, we found no

association between the seeding method and the number of fusion transcripts ($p = 0.0519$, Mann-Whitney U-test), although a fraction of samples had large numbers of RNA fusions, reflecting the wide-spread trans-splicing and genomic instability of immortalized cell lines[118] (**Figure S2.4A**). Finally, there were no significant differences in the number or nature of RNA editing sites between printed and manually seeded samples ($p = 0.977$, Mann-Whitney U-test; **Figure S2.4B**). These findings demonstrate that the bioprinting protocol does not significantly impact the molecular characteristics of tumor cells as measured by bulk RNA sequencing.

Machine learning-based image segmentation and classification enables single-organoid analysis.

Our complete pipeline includes cell bioprinting (day 0), organoid establishment (day 0-3), and full media replacement (day 3, **Figure 2.3A**) followed by transfer to the HSLCI incubator. Within 6 hours of media exchange, we started to continuously image the plates through 72 hours post-treatment. At the end of the imaging period, we performed an endpoint ATP release assay to assess cell viability (**Figure 2.3A**). For downstream data processing, we first converted interferograms collected by HSLCI to phase shift maps using the SID4 software development kit (GPU version, v741)[100]. Then we performed image segmentation and single-organoid level analyses using two types of machine learning algorithms (**Figure 2.3A**).

To reliably identify unique cell clusters within each imaging frame despite the presence of background noise, debris, and out-of-focus organoids, we performed image segmentation using a U-Net architecture[119] with ResNet-34[20,120] as the backbone. U-Net, a type of convolutional neural network (CNN), consists of an encoder that extracts rich feature maps from an input image and a decoder that expands the resolution of the feature maps back to the image's original size. The long skip connections between the encoder and decoder propagate pixel-level contextual information into the segmented organoid masks. The resulting segmentation images are very detailed even when provided small training datasets. We used a training dataset consisting of

manually labeled organoids in 100 randomly selected imaging frames. This model created binary masks indicating whether each pixel of the image belonged to an organoid or the background with a mean Jaccard Index of 0.897 ± 0.109 at the 95% confidence level. The CNN reliably created

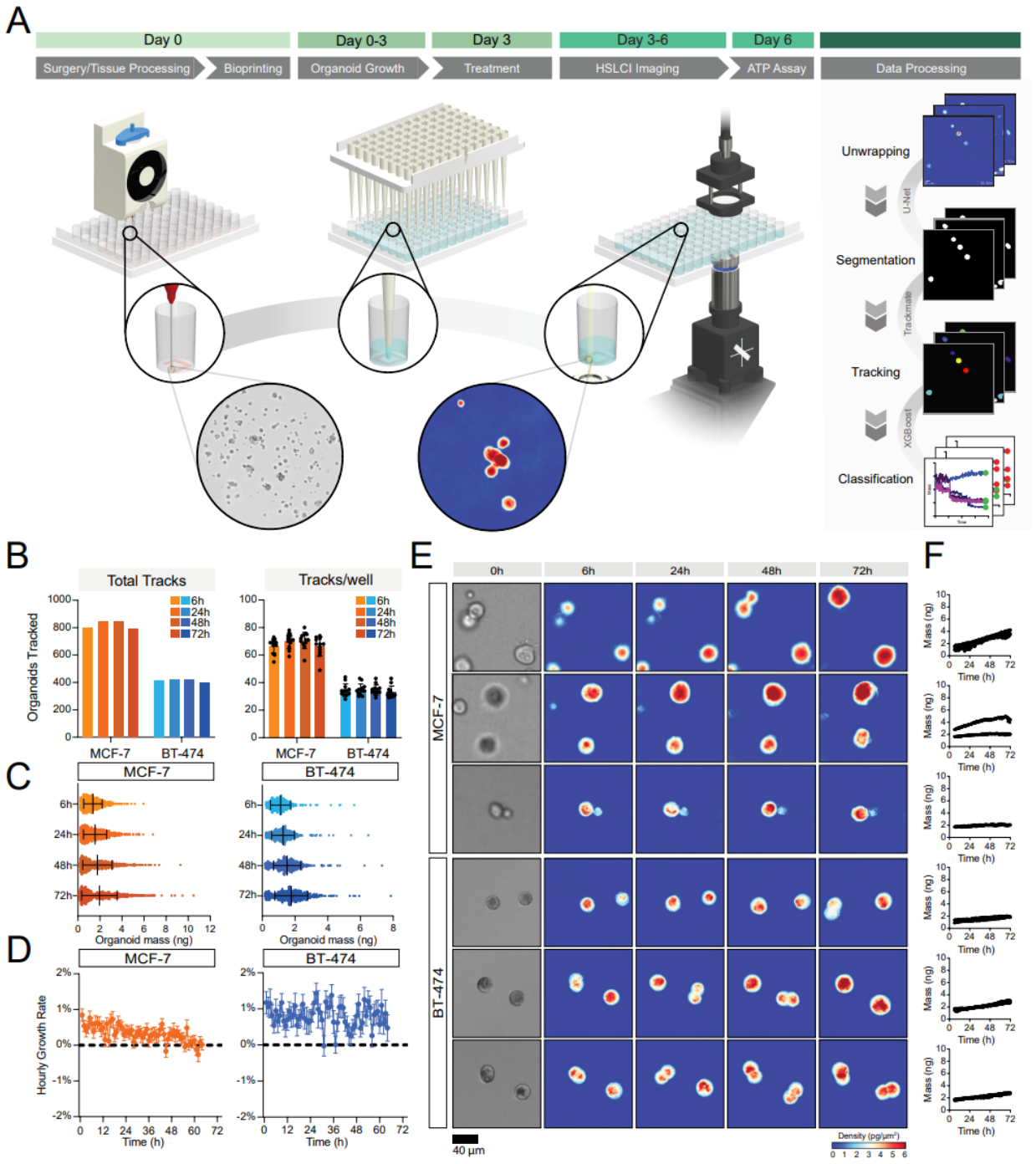

Figure 2.3: Bioprinting enables single-organoid tracking with HSLCI. (A) General schematic of the pipeline. Extrusion-based bioprinting is used to deposit single-layer Matrigel constructs into a 96-well plate (Day 0). Organoid model establishment and growth (Day 0–3) can be monitored through brightfield imaging. After treatment (Day 3), the well plate is transferred to the high-speed live cell interferometer for phase imaging (Day 3–6). Coherent light illuminates the bioprinted construct and a phase image is obtained. Organoids are tracked up to three days using the HSLCI and changes in organoid mass are measured to observe response to treatment. **(B)** Total number of tracks (left) and mean number ± SD of tracks per well (right) for cell clusters from each cell line at four time points (t = 6, 24, 48, and 72 hours after treatment). The total number of tracks across replicate wells treated with vehicle (1% DMSO) was 921 for MCF-7 (n = 12 wells) and 438 for BT-474 (n = 12 wells) **(C)** Mass distribution at four time points (t = 6, 24, 48, and 72 hours after treatment). Black bars represent the mean with error bars representing the standard deviation. Mean and standard deviation calculated based on n = 804, 855, 859, 803 for MCF-7 and n = 421, 420, 423, 402 for BT-474 cell clusters at t = 6, 24, 48, and 72 hours, respectively. **(D)** Hourly growth rate (percent mass change per hour) of tracked MCF-7 (left) and BT-474 (right) cultured in 1% DMSO. Data presented as mean ± SEM for each hour calculated based on growth rate data for n = 921 MCF-7 and n = 438 BT-474 tracked clusters. **(E)** Representative HSLCI-acquired phase images at four time points (t = 6, 24, 48, and 72 hours after treatment). Brightfield images taken immediately before treatment are shown on the left. **(F)** Calculated mass of each representative organoid over time. Source data is provided as a Source Data file.

masks omitting phase artifacts resulting from aberrant background or out-of-focus organoids (**Figure S2.5**).

Next, we determined the mass of each cluster in segmented masks by integrating the phase shift over the organoid area and multiplying by the experimentally determined specific refractive increment[51,54,102,103,121]. We assembled data from discrete segmented cell clusters and organoids into time-coherent tracks using TrackMate[122,123] and filtered mass versus time data for each tracked object using a XGBoost classifier[124] trained to exclude organoids moving in and out of focus, frequently overlapping and/or separating from neighboring clusters, or incorporating debris (**Table S2.1**). We validated the model via cross-validation with 3-fold resampling of the sample population. The 3-fold resampling cross-validation score of the classifier was 93.1 ± 1.3% with a 0.966 ± 0.020 AUC (**Table S2.2**). We also observed trends in the features used to classify

each track, with excluded tracks typically having an increased number of missing frames as well as smaller interquartile ranges, and smaller initial mass (**Figure S2.6**).

Trends in mass accumulation can be quantified by HSLCI with single-organoid resolution.

HSLCI-based imaging allowed continuous tracking of n = 921 MCF-7 cell line-derived organoids in 12 replicate wells (median: 78.5/well) and n = 438 BT-474 in 12 replicate wells (median: 36/well, **Figure 2.3B**). Due to cells moving in and out of the field-of-view (FOV), the number of tracked objects at each time point varied slightly. Overall, we tracked an average of 821 ± 28 MCF-7 and 412 ± 9 BT-474 cell clusters at any given time throughout imaging (**Figure 2.3B**).

Unlike chemical endpoint assays or other live imaging modalities, HSLCI-based imaging facilitates parallel mass measurements of individual cells and organoids. The initial average measured mass at the start of imaging, corresponding to approximately 78 h total in culture, was larger for MCF-7 (1.36 ± 0.84 ng) than BT-474 (1.12 ± 0.61 ng, **Figure 2.3C**). Considering a single cell mass of 200–300 pg[105], clusters contained ~4–7 cells after 3 days in culture as measured by HSLCI, consistent with the observed histopathology (**Figure 2.1E**). The difference in size between MCF-7 and BT-474 persisted throughout the entire imaging duration (**Table S2.3**). BT-474 grew at a rate of 0.80 ± 6.07% per hour while MCF-7 demonstrated slower average hourly growth rates (0.33 ± 4.94% per hour, **Figure 2.3D**). The growth rate of the BT-474 in 3D was slightly slower than BT-474 cells observed after 6 hours in 2D culture (~ 1.3%), while the MCF-7 in 3D showed a much lower growth rate than previously reported 2D cultures (~ 1.7%)[105]. We also observed positive associations between initial mass and growth rate in organoids originating from both lines; however, the association between these factors is stronger for MCF-7 cells (**Figure S2.7**). The data presented provides evidence that cell-line specific 3D growth characteristics can be quantified by HSLCI.

Drug responses in 3D cultures can be quantified by HSLCI.

We then tested the utility of our platform in detecting drug responses in high throughput 3D organoid screenings (**Figure 2.3A**). As proof-of-principle we tested staurosporine, a non-selective protein kinase inhibitor with broad cytotoxicity[125], neratinib, an irreversible tyrosine kinase inhibitor targeting EGFR and HER2[126], and lapatinib, a reversible tyrosine kinase inhibitor also targeting EGFR and HER2[127]. We tested staurosporine at 0.1, 1, and 10 μM, while neratinib and lapatinib were screened at 0.1, 1, 10, and 50 μM (**Figure 2.4**, **Figure S2.8**). The concentration ranges tested include and extend beyond the maximum plasma concentrations reported for both lapatinib (4.2 μM)[128] and neratinib (0.15 μM)[129]. We excluded wells treated with 50 μM neratinib from image analysis because drug precipitation at this concentration resulted in optical opacity. Precipitates and other opaque materials limit data acquisition by causing uninterpretable phase images.

Representative HSLCI images demonstrate a range of responses to treatment (**Figure 2.4A**). Six hours post-treatment, we detected a significant decrease in the average mass of BT-474 clusters treated with 10 μM neratinib relative to the control. The average masses at the start of the imaging window (6 hours post-treatment) did not significantly differ from the vehicle control for all other conditions (**Figure 2.4B**, **Table S2.3**). After 24, 48, and 72 hours, we observed significant differences in a number of treated samples (**Table S2.3**). After 24 hours, control MCF-7 cell clusters averaged 1.56 ± 1.05 ng, while those treated with 1 μM and 10 μM staurosporine showed significant reductions in average mass to 1.18 ± 0.77 ng ($p = 1.93 \times 10^{-9}$, Mann-Whitney U-test) and 1.11 ± 0.69 ng ($p = 1.49 \times 10^{-13}$, Mann-Whitney U-test), respectively. BT-474 showed a similar pattern after 24 hours with control organoids averaging masses of 1.27 ± 0.69 ng while staurosporine-treated clusters averaged 0.76 ± 0.39 ng (1 μM, $p = 2.27 \times 10^{-32}$ Mann-Whitney U-

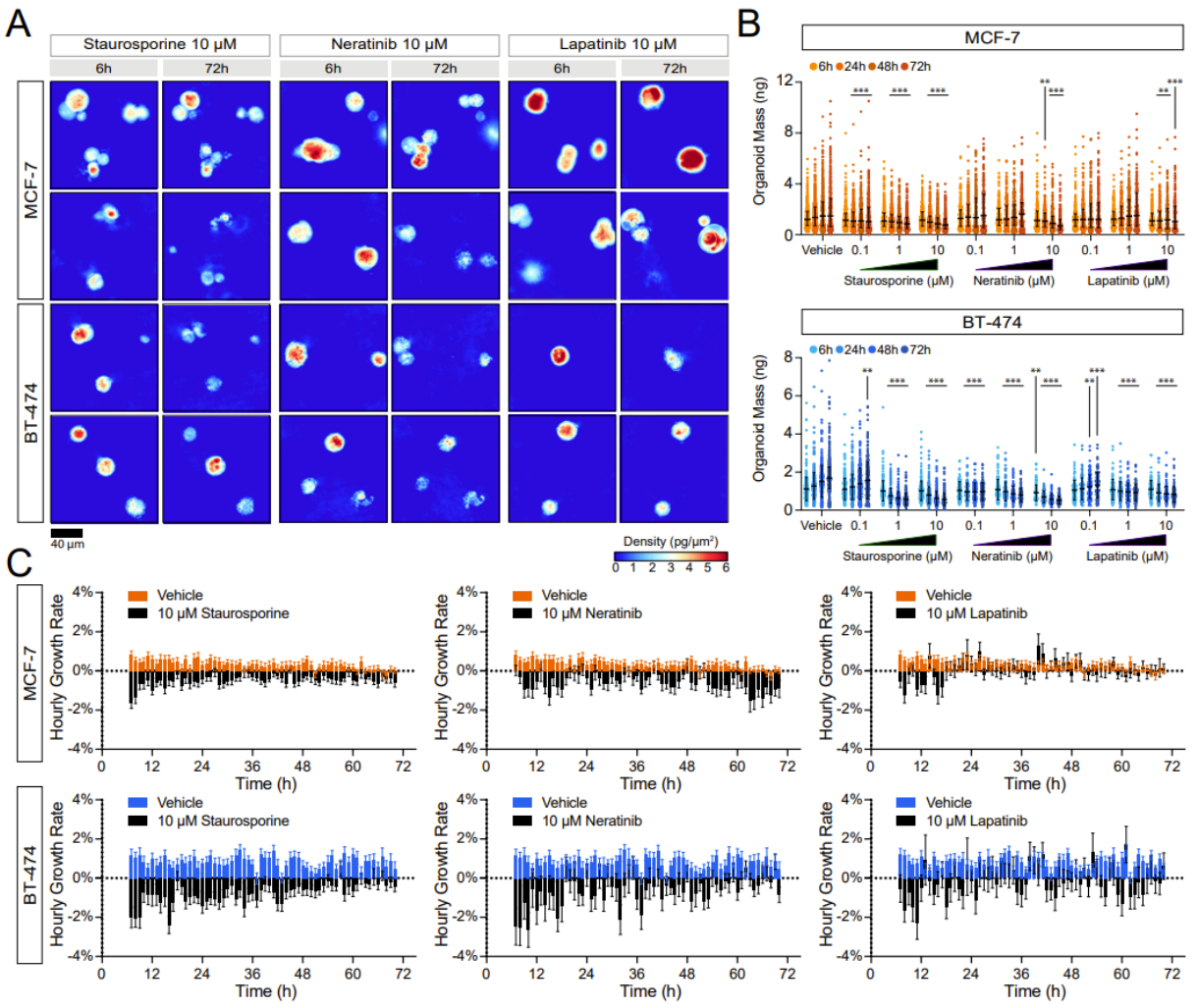

Figure 2.4: HSLCI enables high-throughput, longitudinal drug response profiling of 3D models of cancer. (A) Representative HSLCI-acquired phase images of MCF-7 and BT-474 grown in 3D and treated with 10 µM staurosporine, 10 µM neratinib, or 10 µM lapatinib. **(B)** Each bar represents the mass distribution at 6-, 24-, 48-, and 72 hours post-treatment (left to right). Black horizontal bars represent the median with error bars representing the interquartile range of the distribution. Sample sizes, summary statistics, and exact *p*-values for each condition are available in **Table S2.3**. Statistical significance was assessed using Kruskal-Wallis tests. For samples with *p*-values lower than 0.05, we performed two-tailed Mann-Whitney U-tests against the vehicle control at the respective time points. $p < 0.05$ is denoted by *, $p < 0.01$ is denoted by **, and $p < 0.001$ is denoted by ***. **(C)** Hourly growth rates, calculated as percent mass change per hour, are compared between organoids treated with 10 µM staurosporine and vehicle, 10 µM neratinib and vehicle, and 10 µM lapatinib and vehicle. Data are presented as mean growth rate ± SEM. Growth rate data is derived from $n = 921$, 592, 249, and 292 MCF-7 cell clusters and $n = 438$, 299, 110, and 127 BT-474 clusters treated with the vehicle, 10 µM staurosporine, 10 µM neratinib, and 10 µM lapatinib, respectively. Source data is provided as a Source Data file.

test) and 0.79 ± 0.44 ng (10 μM, $p = 1.59 \times 10^{-28}$, Mann–Whitney U-test). Both MCF-7 and BT-474 rapidly responded to treatment with 1 μM staurosporine, as visualized by plotting normalized growth curves (**Figure S2.9**) and by the reduction in the average growth rate (**Figure 2.4C**).

Responses to lapatinib and neratinib reflected cell line-specific trends consistent with HER2 expression (**Figure S2.2**). BT-474 quickly showed sensitivity to both neratinib and lapatinib, while MCF-7 only exhibited sensitivity to 10 μM lapatinib and neratinib (**Figure 2.4B**, **Table S2.3**). After 24 hours, the mean mass of BT-474 clusters treated with 0.1 μM neratinib decreased to 0.97 ± 0.44 ng from 1.27 ± 0.69 ng ($p = 4.86 \times 10^{-6}$, Mann-Whitney U-test) and those treated with 1 μM lapatinib decreased to 1.00 ± 0.49 ($p = 3.37 \times 10^{-5}$, Mann–Whitney U-test). When comparing EC_{50}s of 2D cultures, manually seeded, and bioprinted 3D cultures, we found no significant change, albeit we observed a trend toward lower EC_{50} for bioprinted MCF-7 treated with neratinib (**Figure S2.10**, **Table S2.4**). Results were consistent across independent experiments (**Figure S2.11**).

Intra-sample heterogeneity of drug responses.

Our combination of HSLCI with machine learning-based tools provides mass tracking of individual cell clusters and organoids, allowing quantitation of intra-sample heterogeneity (**Figure 2.4B**, **Video S2.1**, **Video S2.2**). We assessed the ratio of imaged 3D clusters that gained, lost, and maintained mass over 12, 24, 48, and 72 hours for both control and treated samples (**Figure 2.5A**, **Table S2.5**). In the absence of drug treatment, 11.9% of BT-474 3D clusters lost more than 10% of their initial mass and 80.9% gained more than 10% of their initial mass over 72 hours. In contrast, only 50.8% of MCF-7 gained mass, and 32.6% lost mass. This heterogeneity in populations increases over time, with 23.2% of MCF-7 gaining more than 10% mass within 12 hours. This proportion nearly doubles to 44.8% after 24 hours but remains consistent at 48.6% and 50.8% after 48 and 72 hours, respectively. This pattern differs from BT-474 as the population of organoids that gained mass continually increases over the first 48 hours

before plateauing between 48 and 72 hours. BT-474 that gained >10% mass increased from 30.1% after 12 hours, to 62.4% after 24 hours, and 80.9% after 72 hours.

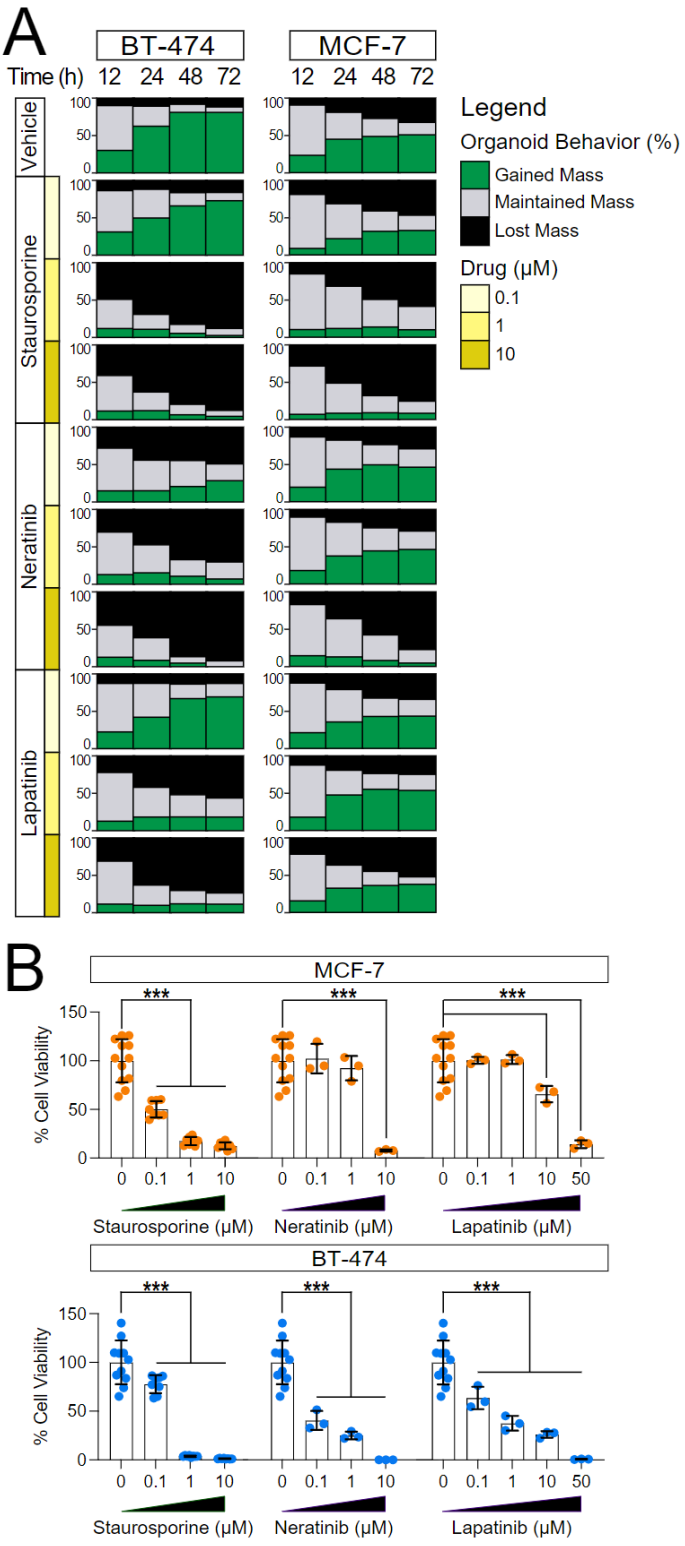

Figure 2.5: HSLCI enables identification of resistant and sensitive 3D cluster subpopulations and discerns response to treatment earlier than endpoint assays. (A) Plots showing the percentage of tracked clusters in each condition that gain (green) or lose (black) more than 10% of their initial mass 12, 24, 48, 72 hours after treatment. **(B)** Relative viability of treated wells in HSLCI-imaged plates of bioprinted MCF-7 and BT-474, determined by endpoint ATP release assays. Bars represent the mean and error bars represent the standard deviation. Each point represents the normalized luminescence signal from independent replicates. $n = 12$ and $n = 11$ wells were treated with the vehicle control for MCF-7 and BT-474, respectively. For treated wells in both experiments, $N = 8$ replicates were screened for each concentration of staurosporine and $N = 3$ replicate wells were screened for each concentration of both lapatinib and neratinib. Statistical significance was assessed using a two-tailed, unpaired t-test with Welch's correction. $p < 0.05$ is denoted by *, $p < 0.01$ is denoted by **, and $p < 0.001$ is denoted by ***. Exact *p*-values are reported in **Table S2.6**. Source data is provided as a Source Data file.

Upon treatment, we observed both inter-sample (MCF-7 vs BT-474) and intra-sample heterogeneity. In the presence of the HER2-targeting lapatinib (10 µm), 37.7% of MCF-7 continued to grow and an additional 10.0% maintained their mass after 72 hours of treatment (**Figure 2.5A**, **Table S2.5**). When treated with 10 µM neratinib, only 4.5% of MCF-7 clusters gained mass, while 18.1% remained stable. In contrast, BT-474 showed greater sensitivity to both drugs, with 11.4% of cell clusters growing and 73.7% losing mass with 10 µM lapatinib treatment (vs 11.9% for controls), and no cell cluster growing after exposure to 10 µM neratinib for 72 hours (**Figure 2.5A**, **Table S2.5**). A subset of BT-474 cells showed high sensitivity to 0.1 µM of both lapatinib and neratinib. In response to lapatinib, 12.8% of BT-474 clusters lost mass, while 17.9% maintained stable mass. When treated with neratinib, 49.1% lost mass and 22.4% maintained stable mass. Both responses contrasted with organoids treated with vehicle, of which 11.9% lost and 7.2% maintained mass. The heightened sensitivity of BT-474 cells to lapatinib and neratinib is expected given the higher expression of HER2 found in these cells[111] (**Figure S2.3**).

A fraction of cells in all treatment-cell combinations were unresponsive to the drugs tested (**Figure 2.5A**, **Figure S2.9**, **Table S2.5**). These grew at similar rates to their vehicle-treated counterparts and comprised between 7.8 and 87.1% of all organoids depending on the cell line

and drug. For example, 37.7% of MCF-7 cell clusters treated with 10 μM lapatinib grew after 72 hours, while an additional 10% maintained stable mass (**Table S2.5**). Similarly, when treated with 10 μM neratinib for 72 hours, nearly 8% of BT-474 maintained their mass, and when exposed to 10 μM lapatinib for 72 hours, the proportion increased to over 25% (**Table S2.5**). Our findings are indicative of a resistant population of organoids that can be rapidly identified by HSLCI imaging. These persisters may provide a unique model for understanding de novo and acquired treatment resistance.

Lastly, to validate the responses measured by HSLCI, we performed an endpoint ATP release assay on the same plates used for HSLCI imaging and assessed viability at the end of the 72-hour treatment (**Figure 2.5B**). The ATP assays confirmed that both cell lines are highly sensitive to staurosporine, with near-zero viability at the 1 and 10 μM concentrations. Additionally, BT-474 showed significant reductions in viability when treated with 0.1 μM lapatinib and 0.1 μM neratinib for 72 hours (**Table S2.6**). Overall, the results of the cell viability assays after 72 hours confirmed the trends observed in as little as 6 hours by HSLCI but fail to capture intra-sample variability.

Discussion

Cancer therapy is increasingly moving towards treatments tailored to each patient's unique and heterogeneous disease[130,131]. Molecular precision medicine requires knowledge of the associations between molecular features and drug response;[2,132] however, many of these relationships have yet to be established[133]. Functional precision medicine bypasses the need to have prior knowledge of these associations and several studies have related in vitro response with patient outcomes[39,83,84,93]. Key limitations towards the broad adoption of functional precision medicine have been the creation of physiological culture models, the development of high throughput systems, and the difficulty in measuring organoid heterogeneity[21,25,80,94,134]. Our pipeline overcomes each of these barriers by incorporating a robust 3D organoid bioprinting

protocol and an imaging approach that facilitates single-organoid analysis of response to treatment.

We introduced bioprinting to enhance the throughput and consistency of our previously published organoid screening approaches[20,27,38]. We opted to print a Matrigel-based bioink due to its ability to preserve tumor characteristics ex vivo[27,31]. Matrigel behaves as a liquid in a narrow temperature range under its gelation temperature of 6–8 °C. Above these values, it shows time- and temperature-dependent changes in viscosity while it thermally crosslinks[135,136]. Without strict control of temperature and bioprinting preparation procedures, bioink can vary in viscosity. As a result, extrusion pressure may need to be adjusted with each print. Although these physical properties complicate its suitability for bioprinting, we show that bioprinting simple, single-layer Matrigel structures is attainable with strict temperature regulation. We further enhanced the quality of the Matrigel deposition by selectively modifying the print substrate with oxygen plasma treatment. The introduction of 3D plasma masks (**Figure S2.1**) facilitated the selective treatment of a square region in each well. The increased hydrophilicity of the substrate in the exposed region guides the spreading of the material to maximize consistency in deposition volume and construct thickness while preventing obstruction of the center of the well. Bioprinting allowed us to finely control the size and shape of the deposited gel constructs, facilitating the use of HSLCI for downstream analysis (**Figure 2.1**).

We have optimized a low pressure, temperature-controlled extrusion-based bioprinting protocol to avoid altering tumor cells. Though it is possible that a subset of cells may be influenced by the bioprinting process, our bulk RNAseq analysis suggests this would be limited to a very small subpopulation. Overall, the sum of our orthogonal findings supports the conclusion that the cells we tested were largely unaffected by the mild bioprinting conditions used in our studies. This applies to the specific combination of bioprinting parameters and cell models included in this work. It will be important to continue evaluating the biological effects of bioprinting in the context of

future studies that either use alternative printing protocols or are focused on different patient-derived samples.

Previous studies have used interferometry to quantify the mass of individuals cells cultured on 2D substrates to study cell division[137], cytoskeletal remodeling[138], mechanical properties[139], and response to treatment[54,66,71]. Tomographic QPI has also been used to obtain high-resolution images of 3D objects such as cerebral organoids[140] and cancer organoids[64]. An enduring challenge of adapting high throughput quantitative imaging techniques to organoid models of cancer is efficient visualization of 3D clusters[21,141]. HSLCI imaging records 2D projections of the phase shift of incident light caused by cultured cells or organoids at a single focal plane relative to the plate surface[66]. 2D phase shift maps only provide accurate biomass measurements for objects in focus[100,142]. When using HSLCI to measure biomass, efficiency can be reduced by organoids moving orthogonally to the focal plane over the duration of imaging. We mitigated this challenge by using bioprinting to generate uniform, thin constructs that maximized the number of organoids that could be tracked in parallel, coupled with a machine learning-based organoid classifier that excludes out-of-focus objects from the analysis. Alternatively, an imaging system capable of capturing multiple z-planes across the plate could address this issue. Such an approach, however, would decrease the frequency of organoid imaging and increase the size of the resulting dataset, which poses different challenges for timely and efficient data analysis.

By introducing region-specific reference images and machine learning-based methods for image segmentation and track filtering, we have been able to increase the number of organoids tracked approximately 15-fold from initial analyses in which only approximately 1% of organoids analyzed were retained using standard approaches (**Figure S2.11**). Further improvements will include shortening the 6-hour delay between drug treatment and imaging start, which will allow us to capture highly sensitive organoids undergoing cell death within that timeframe. Lastly, due

to the large amount of data generated using HSLCI (approximately 250 GB per plate/day), data analysis remains a time-limiting factor.

Our work uses bioprinting in combination with time-resolved HSLCI for high throughput, label-free biomass profiling of 3D models of cancer. While other groups have previously bioprinted organoid models[143–146] to assess drug treatments[144–146], most of these systems, like other screening approaches, used endpoint chemosensitivity assays that return well-level average measurements at a single time point[141]. These endpoint assays are limited in their ability to uncover transient responses and heterogeneity in growth and drug sensitivity phenotypes[141]. In contrast, the time-resolved, organoid-level information returned by HSLCI enables the characterization of rare, drug-resistant cell subpopulations, providing additional insight that cannot be resolved by population-based assays. Genomic characterization of tumors has demonstrated that these malignancies are collections of evolutionarily-related subclones, rather than homogeneous populations[147–150]. This genetic diversity is one of the several factors that contributes to differential response to treatment. Endpoint assays, such as live-dead staining or ATP release quantification, characterize the average response to treatment. Though they may be useful for identifying drug sensitivity in majority cell populations, they fail to account for the response of resistant clones that may also be present. In the clinical setting, failure to treat the resistant populations may cause recurrence and long-term disease progression after initial responses[151–153]. Despite the development of 3D cancer models with varying extents of complexity and scalability, functional screening assays have been hindered by their inability to consider this heterogeneity of tumor responses. HSLCI allows non-invasive, label-free tracking of various features of bioprinted organoids over time, including size, motility, and mass density at single-organoid resolution. Because of the ability to quantitatively measure time-resolved, individual mass changes in response to treatment, it is possible to identify and isolate responsive and resistant subpopulations of cells which can lead to more informed clinical decision making when

selecting a treatment approach[73]. The combination of throughput, time resolution, and number of organoids sampled[64,154,155], paired with our short experimental time frame from seeding to drug sensitivity results[20,27,38,72], make our HSLCI-based method valuable for screening tumor organoid models for research and, in the future, for possible clinical applications.

Methods

2D cell culture

MCF-7 and BT-474 breast adenocarcinoma cell lines were obtained from the American Type Culture Collection (ATCC). All cell lines were grown for a maximum of 10 passages in RPMI 1640 medium (Gibco 22400-089) supplemented with 10% fetal bovine serum (FBS, Gibco 16140-071) and 1% antibiotic-antimycotic (Gibco 15240-062). Both cell lines were periodically authenticated by short tandem repeat profiling using the GenePrint 10 kit (Laragen). For all 2D drug screening experiments, MCF-7 and BT-474 cells were plated manually in 96-well plates (Corning 3603) at 2500 cells/100 µL per well in RPMI 1640 medium with 10% FBS and 1% antibiotic-antimycotic, and then incubated at 37 °C and 5% CO_2 for 3 days.

Manually seeded 3D organoids

Organoids were seeded manually according to our previously published protocols[20,27,38]. Briefly, single cells suspended in a 3:4 mixture of Mammocult (StemCell Technologies 05620) and Matrigel (Corning 354234) were deposited around the perimeter of the wells of either 24-well or 96-well plates. The cell suspension was kept on ice throughout the seeding process to prevent the gelation of the Matrigel. To seed organoids in a 96-well plate (Corning 3603), a pipette was used to distribute 5 µL of cell suspension (5×10^5 cells/mL) along the bottom perimeter of each well. Once all mini-rings were generated, plates were incubated at 37 °C and 5% CO_2 for 20 minutes to solidify the Matrigel, and 100 µL of pre-warmed Mammocult medium was added to

the center of each well using an epMotion 96 liquid handler (Eppendorf). To generate larger rings (maxi-rings) in 24-well plates (Corning 3527), 70 µL of cell suspension (1.4×10^6 cells/mL) was deposited around the perimeter of each well. Following seeding, the plate was incubated at 37 °C and 5% CO_2 for 45 minutes to solidify the Matrigel, and 1 mL of pre-warmed Mammocult was added to the center of each well. Plates were imaged daily using a Celigo S Imaging Cell Cytometer (Nexcelom) in brightfield mode.

3D printing plasma masks

Custom well masks were designed to meet the specifications of the well plates that were used in these experiments (**Figure S2.1**). The design was generated in Inventor 2020 (Autodesk) and printed using a Form3B (FormLabs) using the Biomed Amber resin (FormLabs). The design was exported as an STL file and imported into the PreForm (FormLabs) software to arrange the parts. After printing, parts were post-processed in two washes of isopropanol, air-dried for at least 30 minutes, and cured for an additional 30 minutes at 70 °C in the Form Cure (FormLabs).

Bioprinted 3D organoids

Cells were bioprinted using a CELLINK BioX with a Temperature-Controlled Printhead. G-code files were written to print the desired single-layer geometry. MATLAB (MathWorks) was used to integrate these standardized blocks into full G-code files with the defined coordinates for each well. 8-well plates were used when printing the maxi-rings for IHC and RNAseq as the depth of the well in a standard 24-well plate prohibited the use of 0.5” length needles. For each time point, four rings with a diameter of 14.5 mm were printed for RNAseq (~ 2×10^5 cells total), while four sets of concentric 14.5 mm, 12.5 mm, and 10.5 mm diameter rings were used for IHC analysis (~ 5×10^5 cells total). Mini-squares with side length 3.9 mm were printed into glass-bottom plates (Cellvis P96-1.5H-N) for drug screening and HSLCI imaging. The mini-squares were inscribed within the circular well with sides parallel to the sides of the well plate. All bioprinting processes

utilized the same material deposited for manually seeded organoids: a single-cell suspension in a 3:4 mixture of Mammocult and Matrigel on ice. After vortexing briefly, the mixture was transferred into a 3 mL syringe to remove air bubbles. The mixture was then transferred to a room temperature 3 mL bioprinter cartridge (CELLINK) by connecting the syringe and cartridge with a double-sided female Luer lock adapter (CELLINK). The loaded cartridge was incubated in a rotating incubator (Enviro-Genie, Scientific Industries) for 30 minutes at the print temperature.

During the incubation period, the printer was sterilized with the built-in UV irradiation function, the printhead was set to the print temperature, and the masked 96-well plates were treated with oxygen plasma. Briefly, well masks were autoclaved prior to use, inserted into the well plate, and pressed in contact with the glass surface. Masked plates were treated with oxygen plasma in a PE-25 (Plasma Etch) for 30–90 seconds, 15 minutes prior to bioprinting. After plasma treatment, the well plate was placed in the bioprinter, and Automatic Bed Levelling was performed.

Once the incubation period ended, a 0.5” 25-gauge needle (CELLINK) was attached to the cartridge which was loaded into the pre-cooled printhead. The printer was primed by extruding a small volume of material at 10–15 kPa prior to calibrating the printer. The material in the needle gelled during the printer calibration which took approximately 2 minutes. After calibration, a second extrusion using 40 kPa was performed to clear the needle of the gelled material prior to starting the print and ensure unobstructed material extrusion. To create constructs of the appropriate thicknesses, prints in 8-well plates were extruded at 15 kPa while prints in 96-well plates were extruded at 7–15 kPa. Each print of mini-squares in a 96-well plate is deposited by the bioprinter in approximately four minutes. After printing, the constructs were imaged and incubated at 37 °C for at least 30 minutes to solidify the matrix and 100 µL of Mammocult medium was then added.

Sample preparation for RNA sequencing

Two independent experiments were conducted using an identical protocol. In each experiment, four maxi-rings were printed and manually seeded for each cell line and time point. Printed and manually seeded samples were seeded from a single bioink preparation for each cell line to preclude batch-to-batch variation from analysis. All organoids were seeded at the same time and the collection protocol was performed at 1-, 24-, and 72-hour time points, harvesting four rings each time. Organoids were released from the Matrigel in preparation for RNAseq. After media was aspirated from each ring, 1 mL of pre-chilled dispase (5 mg/mL, Life Technologies 17105-041) was added to each ring. After a 20-minute incubation at 37 °C, the cell suspension was collected and pelleted by centrifugation at 1500xg for 5 minutes and washed with 45 mL of PBS before centrifuging again at 2000xg for an additional 5 minutes. Once all liquid was aspirated, the tubes were rapidly frozen and stored at −80 °C. Frozen cell pellets (~ 2×10^5 cells) were then transferred to the Technology Center for Genomics & Bioinformatics (TCGB) at UCLA for RNAseq. Sequencing was performed on a NovaSeq SP (Illumina) using the 2 ×150 bp paired-end protocol.

Library preparation

Libraries for RNAseq were prepared with a KAPA Stranded mRNA-Seq Kit (Cat.KK8420). The workflow consisted of mRNA enrichment and fragmentation, first-strand cDNA synthesis using random priming followed by second-strand synthesis converting cDNA:RNA hybrids into double-stranded cDNAs (dscDNA), with dUTP incorporation into the second cDNA strand. cDNA generation was followed by end repair to generate blunt ends, A-tailing, adaptor ligation, and PCR amplification. Different adaptors were used for multiplexing samples in one lane. Data quality was checked using Illumina SAV. Demultiplexing was performed with the Illumina Bcl2fastq v2.19.1.403 software.

RNA sequencing data processing and analysis

FASTQ files were processed using UCLA-CDS pipelines to align and quantify RNA-seq data. Pipeline-align-RNA v6.2.2 performs quality control with FastQC, trims reads with FASTP v0.21.0[156], aligns with STAR v2.7.6[157], marks duplicates with Picard tools MarkDuplicates Spark v4.1.4.1[158], checks duplication rate with dupRadar v1.24.0[159] and outputs sorted BAM files. Reads were aligned to human genome GRCh38.p13. Pipeline-quantitate-RNA v2.0.0 performs isoform and gene quantitation with RSEM v1.3.3[160]. Transcripts with low abundance in all samples (TPM < 0.1; transcripts per million) were excluded resulting in 30,544 transcripts included in the analysis. Pipeline-quantitate-SpliceIsoform v2.0.5 quantitates the relative usage of splice isoforms with rMATS v4.1.0[161]. Pipeline-call-RNAEditingSite v5.6.0 calls RNA editing events with REDItools2 v1.0.0[162]. Pipeline-call-FusionTranscript calls gene fusion events with FusionCatcher v1.33[163]. RNA editing sites were filtered to include adenosine to inosine events with sufficient coverage (Q30 > 10) and frequencies above 0.9. Raw and processed data is available on GEO.

RNA abundance was averaged across replicates. We used a paired t-test to perform hypothesis statistical testing on RNA abundance and Mann Whitney U-tests on the number of fusion transcripts and editing sites between bioprinted and manually seeded tumor organoids. We adjusted for multiple hypothesis testing using the false discovery rate (FDR) method, using threshold FDR < 0.05. Statistical analyses and data visualization were performed in the R statistical environment (v4.0.2) using the BPG[164] (v6.0.1) package.

Germline variants from our samples were called using the GATK RNAseq short variant discovery (SNPs + Indels) pipeline[165] and compared to those from the CCLE cell lines using vcfeval (rtg-tools v3.12.1)[166] to validate sample cell line identity post-hoc.

Immunohistochemistry

Immunohistochemical staining was performed on manually seeded and bioprinted organoids seeded in 24 or 8-well plates, respectively. A detailed procedure has been published[38].

Briefly, samples were prepared for histological analysis by carefully aspirating all media from the well without disrupting the construct and fixing in 10% buffered formalin (VWR 89370-094). The fixed organoids were harvested, transferred to a conical tube and pelleted by centrifugation at 2000xg for 5 minutes. HistoGel (Thermo Scientific HG-40000-012) was then added to the pellet. Once solidified, the cell pellet in HistoGel was placed in a histologic cassette and sent to the UCLA Translational Pathology Core Laboratory (TPCL) for dehydration and paraffin embedding.

Slides (8 µm thin sections) were baked for 20 minutes at 45 °C and de-paraffinized in xylene followed by washes in ethanol and deionized water. For H&E staining, a Hematoxylin and Eosin Stain Kit (Vector Labs H-3502) was used according to the manufacturer's protocol. For Ki-67/Caspase-3, HER2, ER staining and chaperone staining, Peroxidazed-1 (Biocare Medical PX968M) was applied for 5 minutes at room temperature to block endogenous peroxidases. Next, antigen retrieval was performed using Diva Decloaker (Biocare Medical DV2004LX) in a 2100 Retriever (Prestige Medical) heating at 110 °C for 15 minutes. Blocking was performed at room temperature for 5 minutes with Background Punisher (Biocare Medical BP947H) for all antibodies beside Hsp27, 70 and 90 beta that were incubated for 30 minutes. Primary Ki-67/Caspase-3 staining was performed overnight with commercially available pre-diluted Ki-67/Caspase-3 (Biocare Medical PPM240DSAA) solution at 4 °C after an additional 2-minute Background Punisher treatment post-antigen retrieval, and secondary staining was performed with Mach 2 Double Stain 2 (Biocare) solution for 40 minutes at room temperature. Primary antibodies for HER2 (Novus Biologicals, CL0269) and ER (Abcam, E115) staining were diluted 1:100 in Da Vinci Green Diluent (Biocare Medical PD900L). The HER2 antibody was incubated overnight at 4 °C while the ER antibody was incubated at room temperature for 30 minutes. Secondary staining was performed with Mach 3 Mouse Probe and Mach 3 Mouse HRP-Polymer for HER2 and Mach 3 Rabbit Probe and Mach 3 Rabbit HRP-Polymer for ER (10 minutes). Hsp27 (Invitrogen, G3.1), Hsp70 (Invitrogen, MB-H1) and Hsp90 beta (Invitrogen, H9010) were diluted 1:100 in Da Vinci

Green Diluent and incubated overnight at 4 °C followed by Mach 3 mouse HRP probe and Mach 3 mouse HRP-polymer incubated for 20 minutes at room temperature.

Chromogen development was performed with Betazoid DAB (Biocare Medical, BDB2004) followed by counterstaining with 20% hematoxylin (Thermo Scientific #7221). Slides were dehydrated in ethanol and xylene and coverslipped with Permount (Fisher Scientific SP15-100). Imaging was performed with a Revolve microscope (Echo Laboratories). Whole image white balancing was performed in Photoshop (Adobe).

Drug screening

A detailed protocol for the 3D drug screening has been published previously[27,38]. Briefly, the culture medium was fully removed three days after seeding and replaced with 100 µL of Mammocult medium containing the indicated drug treatments using a liquid handler (Eppendorf). After treatment, we transferred the plates to the HSLCI platform for imaging. Staurosporine was tested at concentrations of 0.1, 1, and 10 µM, while neratinib and lapatinib were tested at 0.1, 1, 10, and 50 µM; all drugs were dissolved in DMSO at a final vehicle concentration of 1%. Staurosporine at 1 and 10 µM were used as positive controls, while a 1% DMSO treatment condition was used as a negative control. For HSLCI drug screening experiments, plates were transferred to the HSLCI platform immediately following treatment addition. The content of this article reflects data collected from one HSLCI-based drug screening experiment using organoids derived from each cell line (except for **Figure S2.11**) to illustrate the power of the method to gather extensive data from a single well plate. All replicate wells for a given condition were seeded from the same sample preparation and a single cartridge of bioink.

For all drug screening experiments using 2D cultures, the culture medium was removed three days after seeding using the liquid handler and analogously replaced with 100 µL of Mammocult containing the indicated drug treatments. All drug-treated plates were subsequently

incubated at 37 °C, 5% CO_2 for three continuous days. EC_{50} values are reported for all culture conditions for both cell lines in **Figure S2.10** and **Table S2.4**.

High-speed live cell interferometry

HSLCI has been described previously[66,71]. The HSLCI platform is a custom-built inverted optical microscope coupled to an off-axis quadriwave lateral shearing interferometry (QWLSI) camera (SID4BIO, Phasics, Inc.)[100]. This wavefront sensing camera incorporates a modified Hartmann mask that splits the incident wave front into four tilted replica wavefronts that interfere with one another. The resulting interferograms are recorded and used to recover phase gradients along two perpendicular directions, allowing for the reconstruction of a phase shift map and subsequent calculation of dry mass of discrete objects within imaging fields of view (FOVs)[46,100]. Measured phase shifts are proportional to mass density[46,45,102,51,103,167] and are converted to mass using Eq. (3)[45,46,54],

$$m = \frac{1}{\alpha}\int \phi\lambda \mathrm{d}A \tag{3}$$

where m is dry biomass, Φ is the measured phase shift as a fraction of wavelength, λ is illumination wavelength, integration is performed over the area A of imaged objects, and α is the specific refractive increment, defined as the slope of the relationship between the refractive index and mass concentration of a solution[45,46,51]. Because the specific refractive increments of the biomolecules that constitute most of a cell's dry mass fall within a narrow range[46,50–52,54,103], α can be assumed to have an average value of 1.8×10^{-4} m^3 kg^{-1} [46,50–52,54,103,167,168].

Illumination is provided by a 660 nm fiber-coupled LED (Thorlabs). The HSLCI platform captures images from a standard-footprint (128 × 85 mm) glass-bottom multiwell plates. Motorized stages (Thorlabs) control the xy-motion of a single glass-bottom plate above the microscope objective and, in combination with a piezo-actuated dynamic focus stabilization system, enable continuous and repeated image collection over many FOVs within each row of

wells. The HSLCI platform is installed inside of a standard cell culture incubator to enable long-term imaging of samples in physiology-approximating conditions (37 °C, 5% CO_2). All hardware and software components are available commercially.

For all growth kinetics and drug screening studies, organoids were imaged in 96-well glass-bottom plates (Cellvis P96-1.5H-N) using a 40× objective (Nikon, NA 0.75). Plates of bioprinted organoids were prepared as described and wrapped with parafilm to limit evaporation during imaging. Organoids were imaged continuously from 6 hours to 72 hours following the administration of drug treatments. During imaging, the sample plate was translated along each row of wells such that about 25 images per well were collected on each imaging loop, and that imaging FOVs overlapped with areas of wells in which bioprinted matrix and organoids were present. The typical imaging interval was 10 minutes between successive frames at the same FOV.

Machine learning–based analysis of HSLCI images

Images were acquired using the SID4Bio software (v2.4.2.93, Phasics). After image collection, interferograms captured by the QWLSI camera were converted to phase shift images using the SID4 software development kit for MATLAB (GPU version, v741, Phasics), in a process called phase unwrapping. A custom analysis pipeline was developed in Python and can be run using Nextflow (see the Code Availability section for accession information). For every frame at each FOV, phase shift maps were processed by converting to optical path difference[100], and then subtracting the fourth-order Zernike polynomial[58] fit to each frame using least-squares over a cartesian grid to remove refractive aberrations.

The processed images were then segmented into individual cells or organoids using a convolutional neural network (U-Net architecture[119] with a ResNet-34 encoder[20,120]). The model was initialized with weights derived from a model pretrained on the ImageNet dataset[169]. The training dataset consisted of a randomly selected set of 50 images from the BT-474 dataset, and

50 from the MCF-7 dataset encompassing images taken at all wells, intra-well imaging positions, and timepoints within each experiment. Each 514 × 514 pixel image was overlaid with a binary mask that marks each pixel as either part of an organoid or the background. Using the training dataset, the weights were refined using a cross-entropy loss function over 80 epochs. Phase images and their corresponding masks were organized into one stack per imaging FOV with each layer sorted by time of imaging. TrackMate (v7.6.1)[122,123] was used to track the organoids over time using a Sparse LAP Tracker with a maximum linking distance of 90 pixels and feature penalties of 4.0 for both the major ellipse axis and organoid area. These parameters were selected based on optimal performance on a set of 12 representative image stacks. Gaps of up to 30 frames were tolerated to maximize track continuity between organoids. Tracks composed of fewer than 10 frames were excluded. Labeled image stacks were exported and mass was extracted from the segmented regions by integrating the phase shift over the area and multiplying by the refractive increment of 1.8×10^{-4} m^3 kg^{-1} [51,54,103,121].

An XGBoost-based classifier (v1.5.2.1, probability prediction type, log-loss evaluation metric)[124] was used to predict permissibility of organoid tracks using R package mlr3 (v0.13.2). For the supervised learning model, a subset of the tracks was labelled for permissibility ($n = 846$) from four wells: 1) BT-474 well treated with vehicle, 2) BT-474 well treated with 10 µM staurosporine, 3) MCF-7 well treated with vehicle, and 4) MCF-7 well treated with 10 µM staurosporine. It was manually determined that $n = 250/846$ tracks were acceptable for downstream analysis. A set of time-series based features were extracted from the mass reconstruction data to use in our classifier model. The features were number of missing frames, initial size, interquartile range (IQR), IQR of the first 12 points, and IQR of the last 12 points (**Figure S2.6**). Initial size was calculated based on the median mass of the first two timepoints. Area under the curve (AUC) measurements were calculated using R package (bayestestR v0.11.5) (**Figure S2.12**). Pair-wise correlation plots comparing the void and valid track features were

generated using mlr3viz R package (v0.5.7) (**Figure S2.6**). Probability was used as the learner prediction type and log-loss (log_{10}) as the evaluation metric. All default hyperparameters were used (**Table S2.1**). To validate the model, 3-fold cross-validation with resampling was performed. The trained model had excellent accuracy and specificity with an AUC of 0.966 ± 0.020 and a cross-validation score of $93.1 \pm 1.3\%$ (**Table S2.2**). The model was applied to the whole dataset and predicted $n = 8{,}590/29{,}137$ tracks to be permissible for downstream analysis.

ATP release assay

Manually seeded organoids, bioprinted organoids, and 2D-cultured cell lines were prepared in accordance with the protocols described above and published[20,27,38]. For drug screenings, plates were retrieved from the HSLCI incubator and processed as briefly described. After a PBS wash, 50 µL of 5 mg/mL Dispase (Life Technologies 17105-041) solution was added to each well and incubated for 25 minutes. After shaking for 5 minutes on an orbital shaker (Corning 6780-4) at 800 RPM, we added 30 µL of CellTiter-Glo® Luminescent Cell Viability Reagent (Promega G968B) to each well and followed the manufacturer's instructions. For 2D drug screening experiments, 30 µL per well of CellTiter-Glo® 3D Luminescent Cell Viability Reagent (Promega G968B) was added directly to the drug-treated media at the conclusion of the experiment. Luminescence was measured using a SpectraMax iD3 (Molecular Devices) plate reader (parameters: read all wavelengths, signal integration of 500 ms). The viability of each well was calculated by normalizing the luminescent signal to the average signal from the manually seeded control wells. An unpaired t-test with Welch's correction was performed in Prism 9 (GraphPad). p-values less than 0.05 were deemed significant. EC50 values for each drug-organoid model combination were computed by interpolating the drug concentrations that would yield 50% relative viability in treated organoids. For each drug, results from all tested concentration conditions were used to compute EC50 values from ATP-catalyzed luminescence data, including from 50 µM neratinib-treated wells that were excluded from HSLCI data analysis.

To assess the viability of bioprinted organoids (as shown in **Figure 2.1D**), the bioink and bioprinter were prepared as previously described. Then, 100 µL of bioink was extruded into an Eppendorf tube for each print pressure (10, 15, 20, and 25 kPa). Using a pipette, four 10 µL rings were seeded in a 96-well plate using the extruded bioinks and non-extruded bioink from the same batch. Cells were then released from Matrigel, CellTiter-Glo® 3D Luminescent Cell Viability Reagent (Promega G968B) was added to each well, and ATP-catalyzed luminescence values were obtained as described above. The viability of each well was calculated by normalizing its luminescence signal to the average luminescence signal from the manually seeded control wells. Statistical analyses were performed in Prism 9 (GraphPad). *p*-values less than 0.05 were deemed significant.

Statistics and reproducibility

At the end of each set of experiments, cell identity was confirmed by STR profiling (Laragen). Three independent bioprinting experiments per cell line were used to evaluate organoid properties using IHC, with similar results. We pooled $n = 4$ maxi rings for each condition with the exception of BT-474 24h from experiment #2, with $n = 3$ and proceeded to the library preparation and sequencing for RNAseq experiments. This was repeated on two independent sets of samples by two different operators, and data was aggregated for analysis. HSLCI data presented in **Figures 2.3–2.5** shows an individual experiment for each cell line to demonstrate the quantity of information that can be gathered from a single run. Each HSLCI experiment was repeated a minimum of two times, with similar results as visible in **Figure S2.11** which shows a comparison of two independent BT-474 organoid HSLCI datasets. Statistical tests are described within figure captions, where applicable, with exact *p*-values listed either in the figure legends or within supplementary tables. A significance threshold of $p < 0.05$ was used for all statistical tests. No statistical method was used to predetermine the sample size. We excluded neratinib 50 µM HSLCI data points from the analysis because significant drug precipitates

deteriorate image quality to the point the data measured is not quantitative and thus unusable for image analysis purposes.

Data availability

HSLCI imaging data and training datasets as presented in **Figures 2.3–2.5** are deposited in the BioImage Archive on Biostudies under accession code S-BIAD616 (https://www.ebi.ac.uk/biostudies/bioimages/studies/S-BIAD616). Sequencing data are deposited and available on GEO under accession number GSE218693 (https://www.ncbi.nlm.nih.gov/geo/query/acc.cgi?acc=GSE218693). Source data for all figure components are provided with this paper (https://doi.org/10.1038/s41467-023-38832-8).

Code availability

Code for the data analysis pipeline is publicly available on GitHub at https://github.com/uclahs-soragnilab/hslci_pipeline or Zenodo[170] (https://doi.org/10.5281/zenodo.7787339). A ready-to-use, publicly available Docker image is hosted on Dockerhub at: https://hub.docker.com/r/soragnilab/unetsegmentation.

Supplementary Information

Supplementary Results: Mass reconstruction data extracted for classifier

Mass reconstruction data of n = 8,590 tracked BT-474 and MCF-7 breast cancer cell line-derived organoids were assessed for change in mass over 72 hours following treatment. BT-474 and MCF-7 lines were treated with a series of concentrations of 0.1 to 50 μM of vehicle (n = 1,593), lapatinib (n = 1,650), neratinib (n = 1,626) and staurosporine (n = 2,920). We assessed the cell cluster growth patterns using z-transformed measurements of area under the curve (AUC), linear growth rate, interquartile range, initial and final mass (**Figure S12A**). Sampled BT-474 and MCF-7 under various pharmacological treatments display a diverse set of growth patterns, arranged by AUC metric. Cell line and treatment type were dispersed across the sample population, thus supporting our choice to use a single set of classifier training data for both cell lines and all treatment conditions. We tested whether cell clusters derived from BT-474 cells displayed differences in their growth patterns compared to clusters derived from MCF-7 cells (**Figure S12B**). We found significant differences in growth patterns of BT-474 and MCF-7 across treatments (**Figure S12C**). In most conditions (9 out of 11 conditions), the z-transformed initial size, final size and linear growth rate of MCF-7 clusters were larger than BT-474 in all three pharmacological treatment conditions (**Figure S12B–C**) ($p < 0.0001$, Mann-Whitney U-test). In two conditions, the linear growth rate of BT-474 in the presence of 1 μM lapatinib (fold change = -0.70, $p = 2.76 \times 10^{-2}$) and 0.1 μM neratinib (fold change = -0.82, $p = 3.82 \times 10^{-3}$) were found to be greater than MCF-7. We did not find strong differences in growth patterns among BT-474 and MCF-7 treated with 0.1 μM lapatinib.

Supplementary Figures

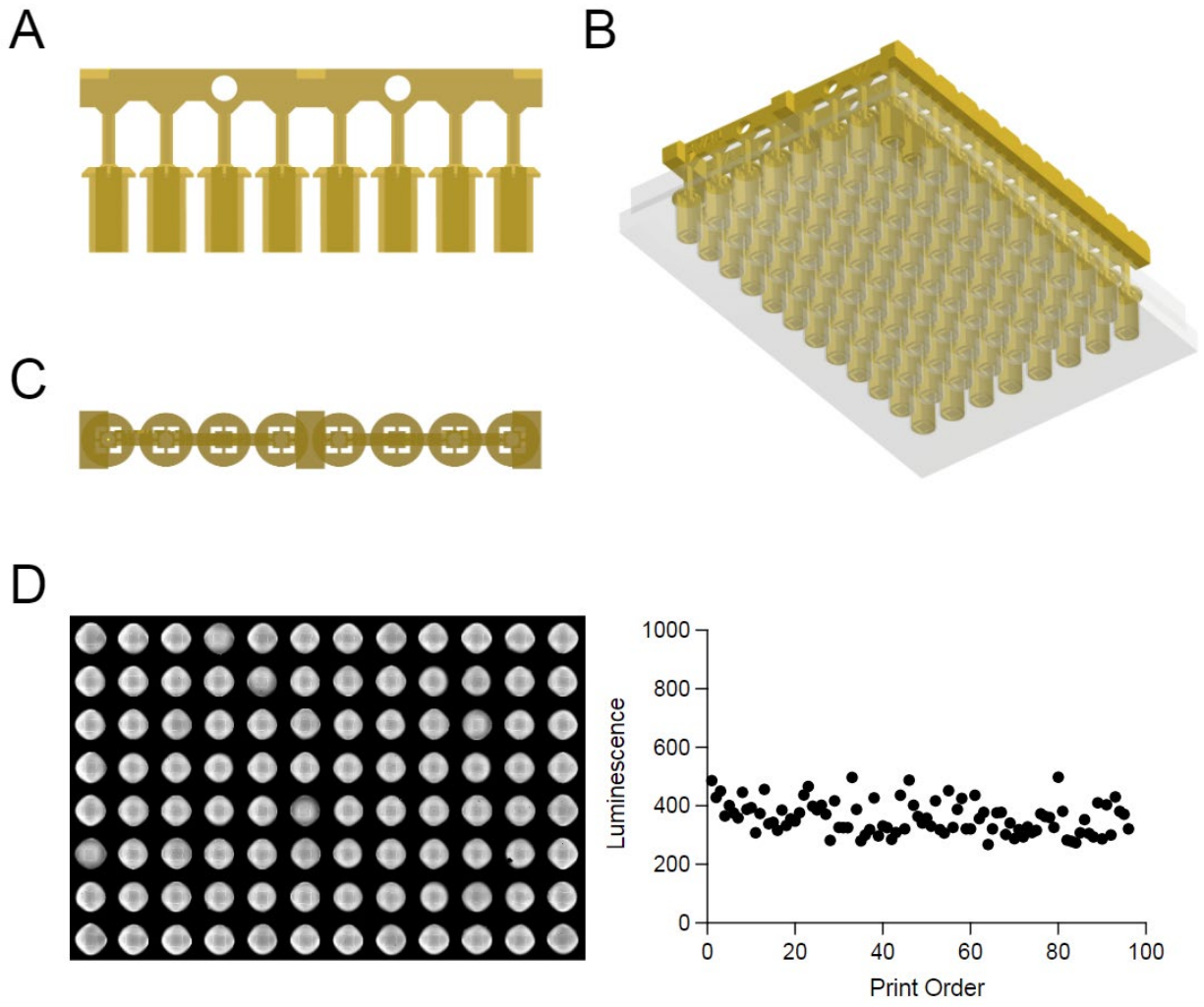

Figure S2.1: Schematics of well mask and representative bioprint and assessment of bioprinting consistency. (A) Side view of plasma masks. **(B)** Bottom view of plasma masks. **(C)** Plasma masks inserted into 96-well plate viewed from bottom. **(D)** Stitched, contrast-enhanced whole-well brightfield images of a representative bioprint of cell-laden Matrigel bioink into a 96-well glass bottom plate. A post-print ATP-release assay was performed, with data plotted on the right. The coefficient of variation (CV%) for the plate shown is 15.6%. The average CV% for bioprinted plates (20.3±6.9) and manually seeded plates (13.8±7.0) used in this study are not statistically different (p=0.34, Mann-Whitney).

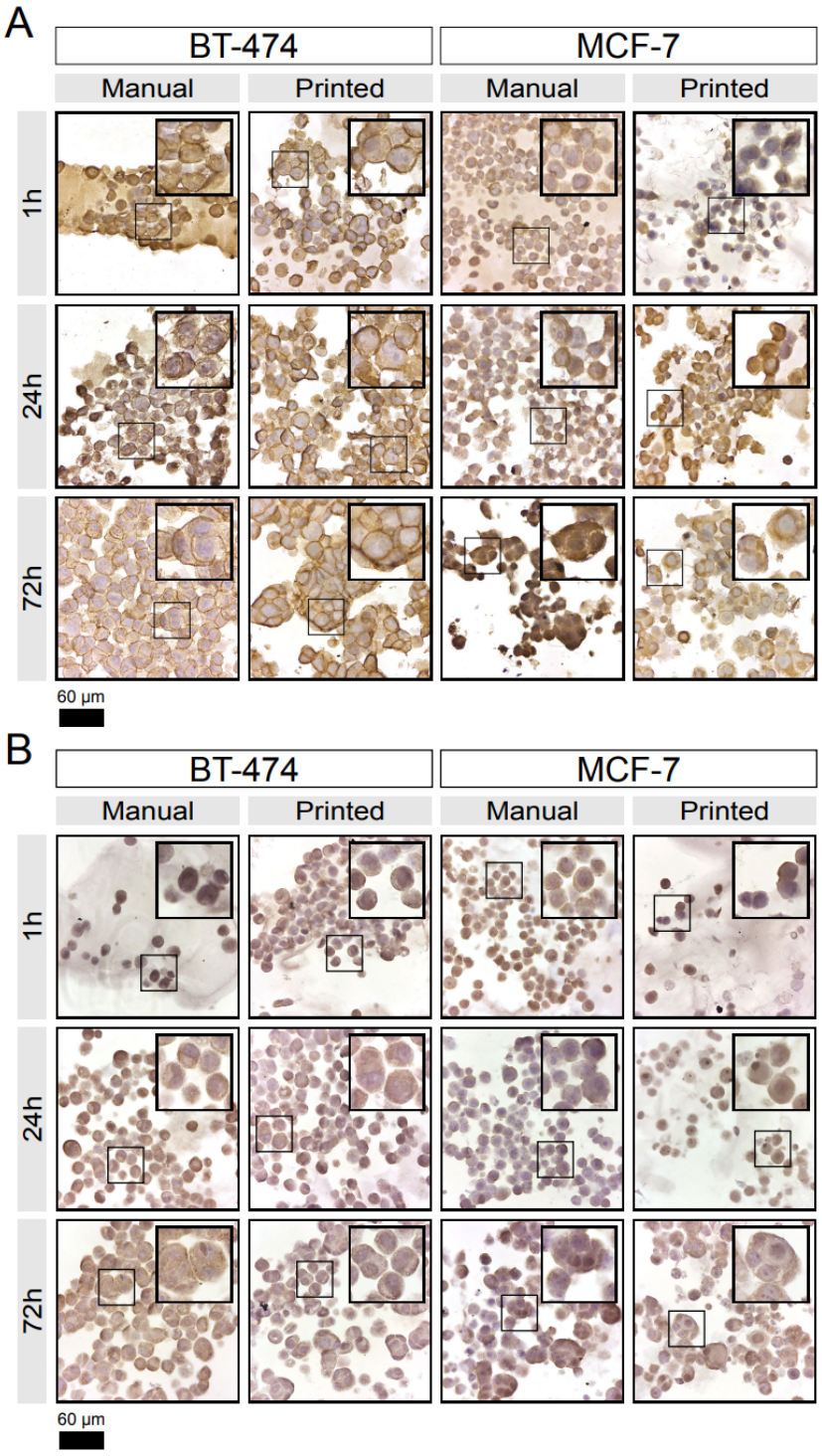

Figure S2.2: HER2 and ER expression in BT-474 and MCF-7 lines is not altered by bioprinting. **(A)** Immunohistochemistry staining of 3D cultures for HER2. BT-474 cells have amplified HER2 expression while MCF-7 cells express lower levels of HER2 and lack HER2 amplification. **(B)** Immunohistochemistry staining of 3D cultures for ER. Both BT-474 and MCF-7 cell lines are ER-positive.

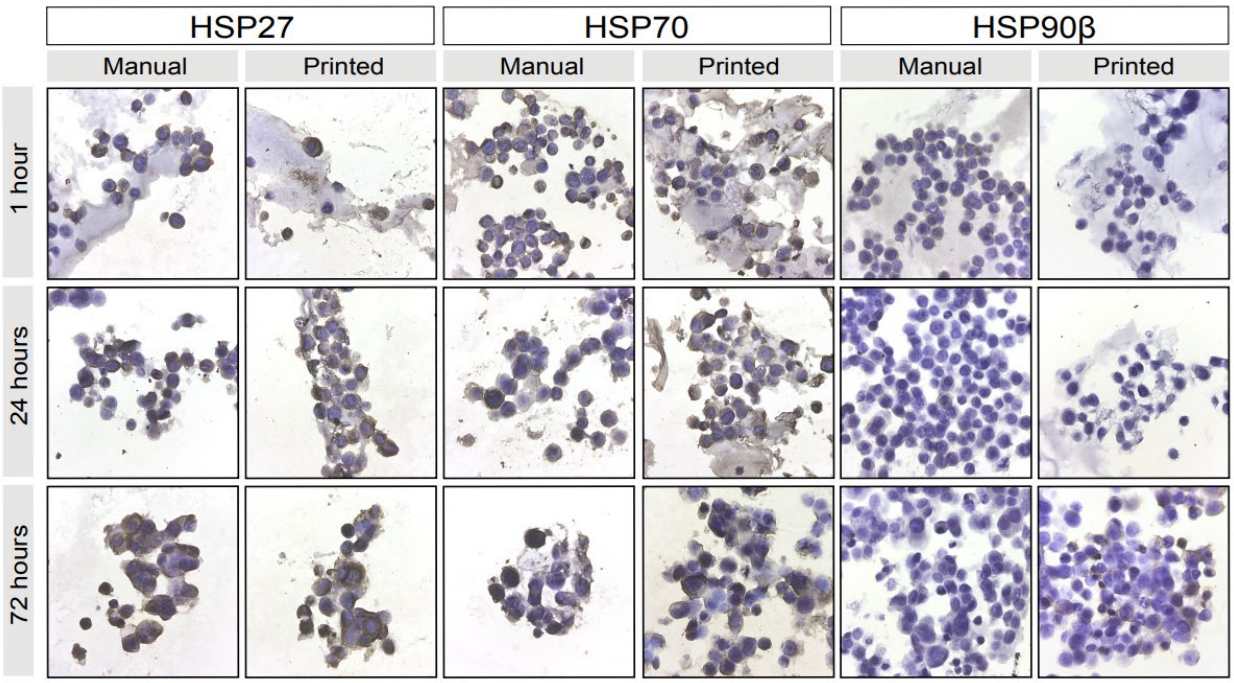

Figure S2.3: Chaperone expression is not altered by bioprinting. Comparison of HSP27, HSP70 and HSP90 staining in BT474 cells 1, 24 and 72 hours after manually seeding or bioprinting. We found no detectable difference in protein levels.

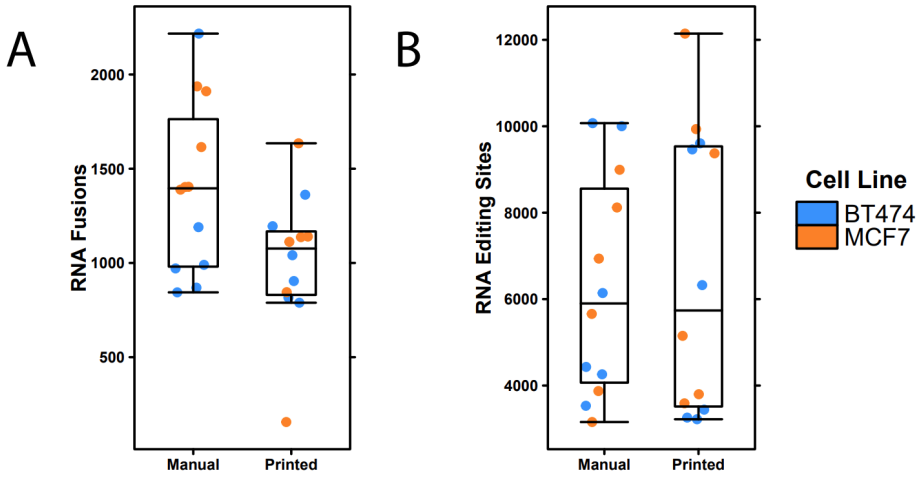

Figure S2.4: Bioprinting did not significantly alter the number of RNA fusions or editing sites. **(A)** Number of RNA fusions detected by FusionCatcher. The number of RNA fusions did not significantly differ between manually seeded and bioprinted organoids ($p = 0.0519$, Mann-Whitney U-test). **(B)** Number of adenosine-to-inosine (A-to-I) RNA editing sites detected by REDItools2. The number of RNA editing sites did not significantly differ between manually seeded and bioprinted organoids ($p = 0.977$).

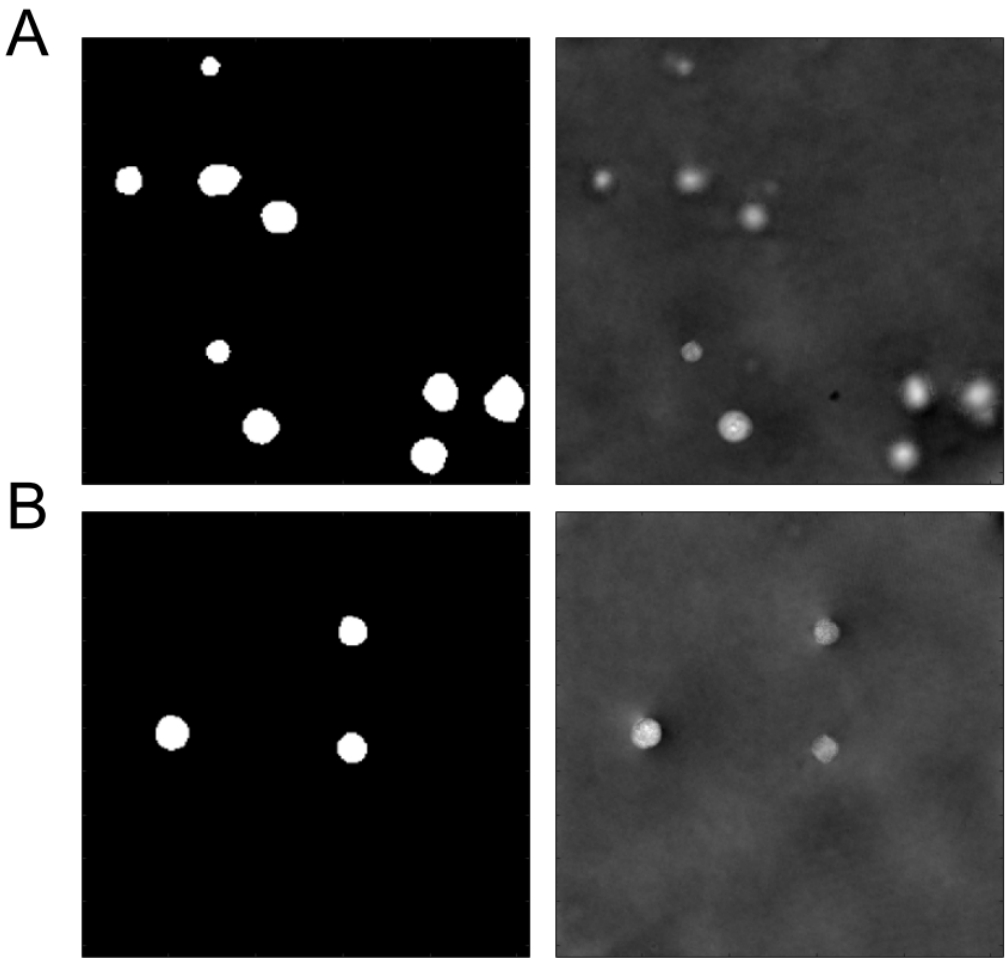

Figure S2.5: Image segmentation using a U-Net convolutional neural network. Representative masks (left) predicted by the U-Net-based segmentation algorithm for the background-corrected phase images (right).

Figure S2.6: Pair-wise correlation matrix of classifier data. Extracted time-series analytical features of tumor growth patterns over recorded time. The number of missing frames (na.count), initial mass (initial.size.sample), interquartile range (sample.IQR), and interquartile range of the first and last 12 data points (start.IQR and end.IQR) were measured for each tracked tumor organoid. We labelled (n = 250 out of 846) tracked organoids as valid for downstream analysis. Pair-wise correlations are shown of the valid (label = 1, green) and void (label = 0, purple) tracked organoids. Void tracks showed an increased number of missing frames, smaller overall IQR, and smaller initial size. Correlation of the classification data are shown within the paired subplots. Overall and end IQR were strongly correlated (R^2 = 0.954). An XGBoost classifier was used to train a model to classify organoids as valid or void. We validated the model via cross-validation with 3-fold resampling of the sample population. The cross-validation score of the classifier was 93.1% with 96.6% AUC (**Table S2.2**).

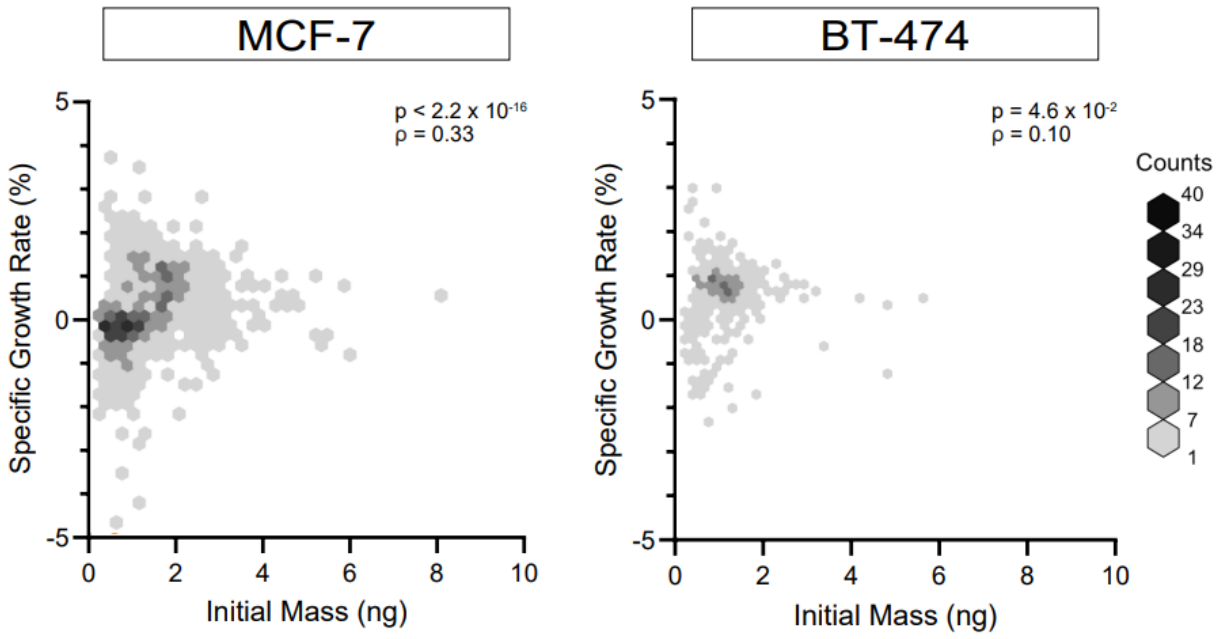

Figure S2.7: Specific growth rate correlates to initial organoid mass. Specific growth rate (growth in mass as a percentage of total mass) versus initial organoid mass was plotted for all organoids tracked. For both MCF-7 and BT-474 cell line-derived organoids, we observed a positive relationship between initial organoid mass and specific growth rate. This association is stronger for MCF-7 cells (Spearman's $\rho = 0.33$, $p < 2.2 \times 10^{-16}$) compared to BT-474 ($\rho = 0.10$, $p = 4.6 \times 10^{-2}$).

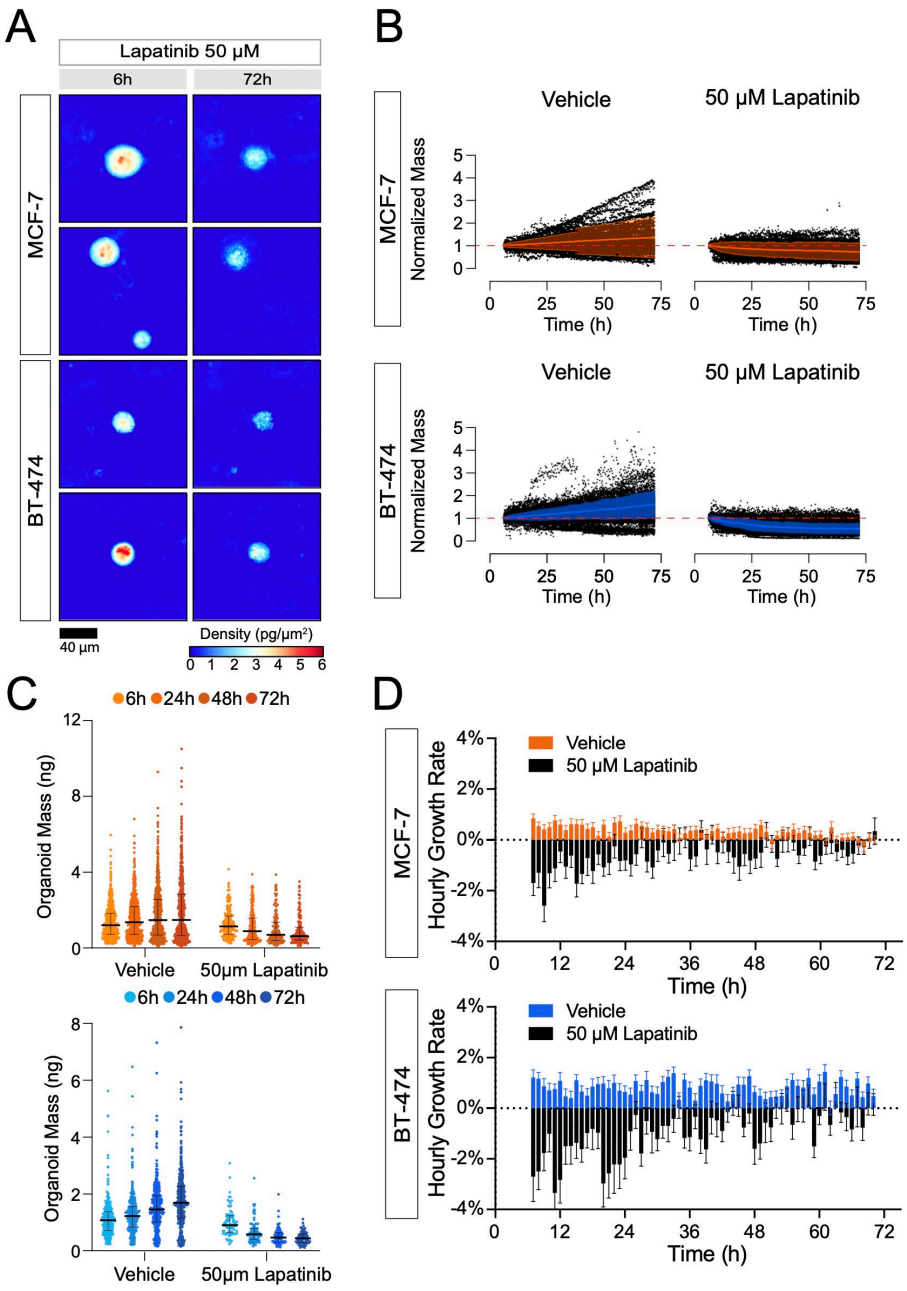

Figure S2.8: Response of bioprinted organoids to 50 μM lapatinib. (A) Representative HSLCI-acquired phase images of organoids treated with 50 μM lapatinib. **(B)** The mean normalized mass ± standard deviation is shown in orange (MCF-7) and blue (BT-474). 100 organoid tracks are shown on each plot. **(C)** Mass distribution of tracked MCF-7 and BT-474 by treatment. Each column represents the mass distribution at 6-, 24-, 48-, and 72-hours post-treatment (left to right). Black horizontal bars represent the median with error bars representing the interquartile range of the distribution. **(D)** Hourly growth rate comparisons (percent mass change) between organoids treated with 50 μM lapatinib and vehicle.

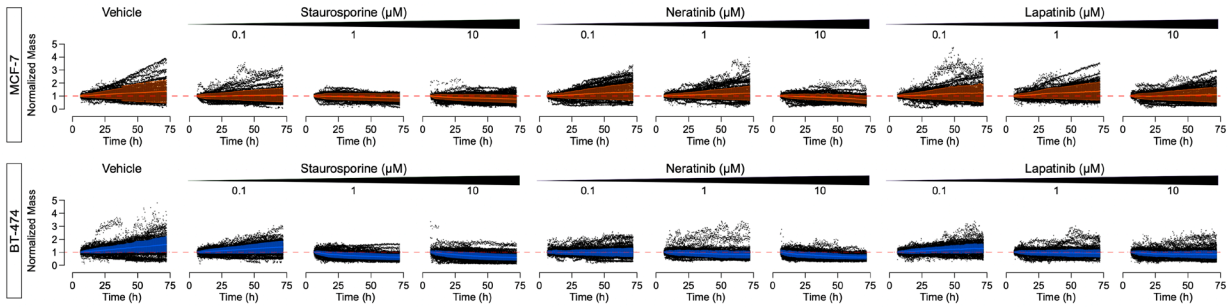

Figure S2.9: Representative normalized mass tracks by treatment condition. The mean normalized mass ± standard deviation is shown in orange (MCF-7) and blue (BT-474). 100 organoid tracks for each treatment condition are shown on each plot.

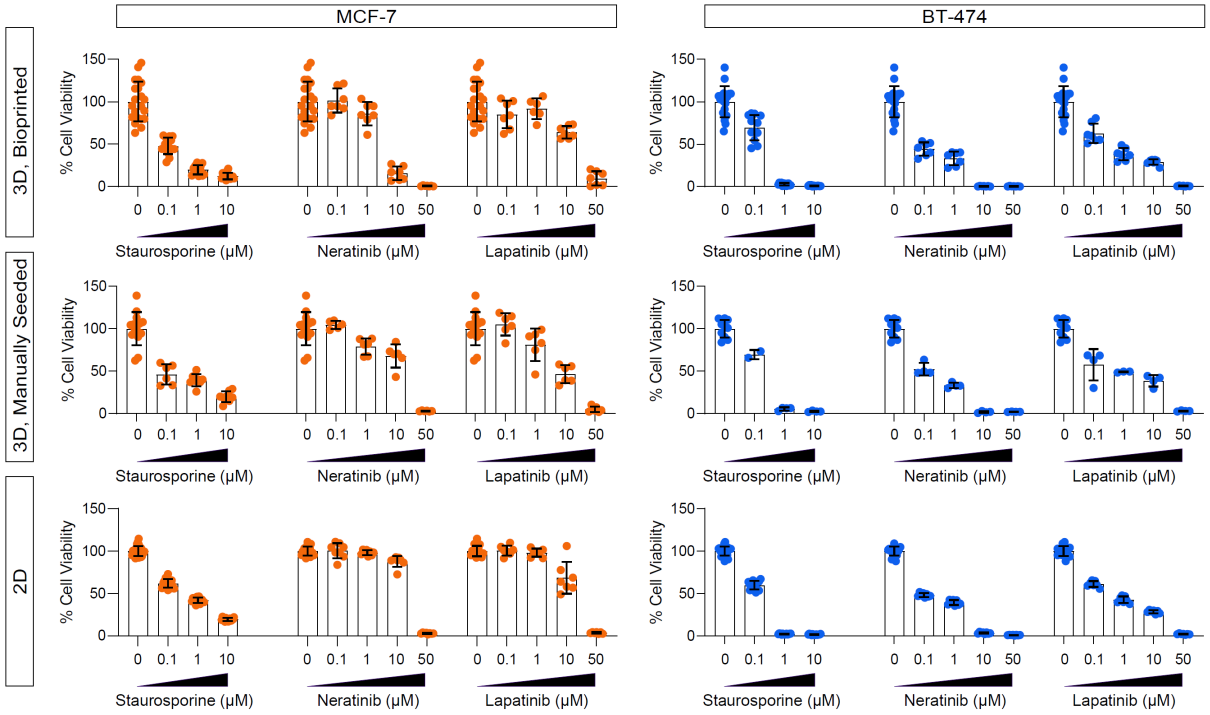

Figure S2.10: ATP assay readout in multiple culture conditions. ATP-release assay quantifies cell viability for staurosporine, neratinib, and lapatinib- treated MCF-7 and BT-474 breast cancer models in 3D culture following bioprinting, 3D culture following manual seeding, or 2D monolayer cell culture. Data shown were merged from a minimum of n=2 independent experiments. Bars represent mean values, and error bars represent standard deviation (SD).

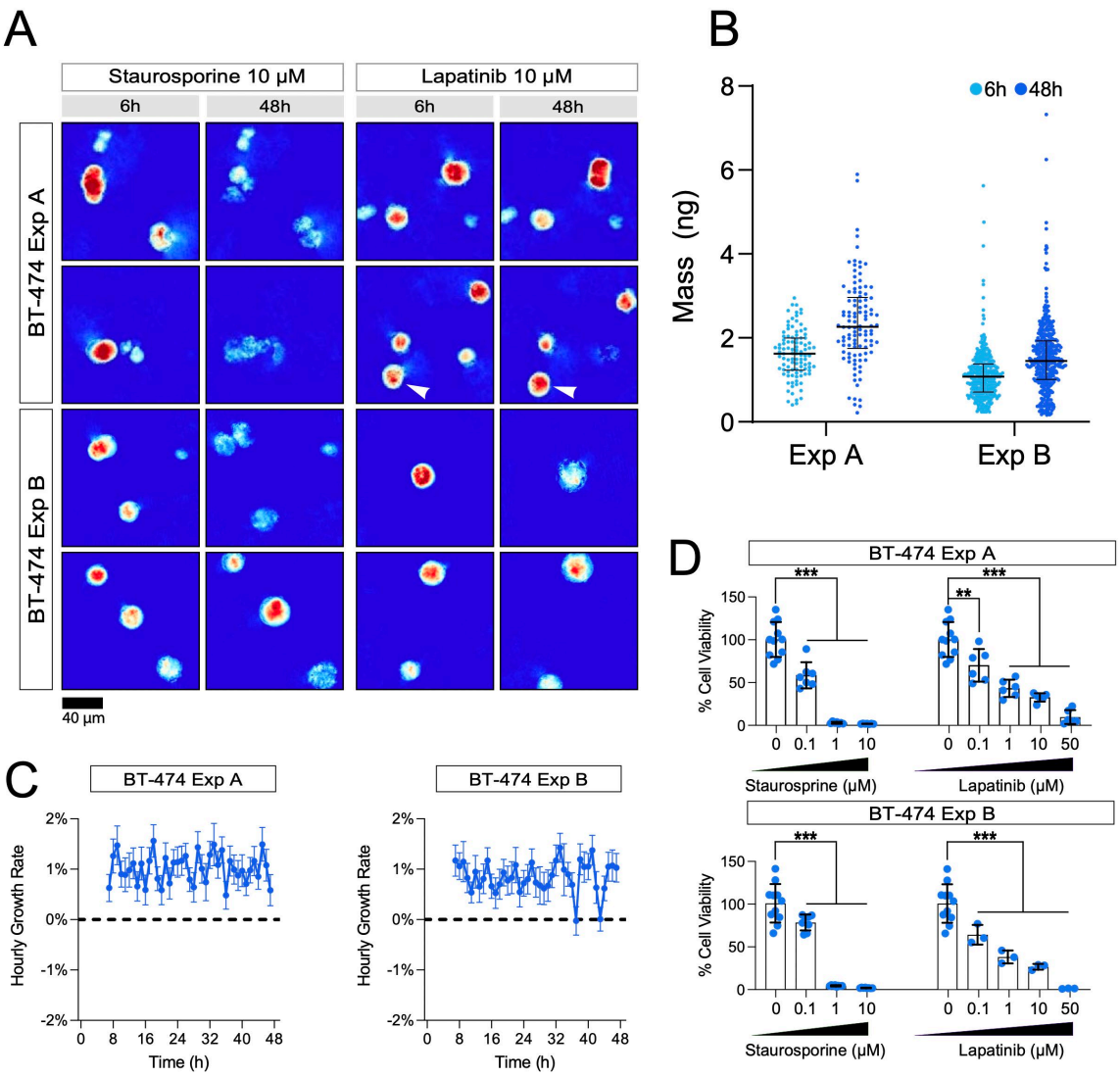

Figure S2.11: Comparison of BT-474 organoid datasets. Experiment A and B were independently performed and followed the same protocols with three exceptions. Experiment A had a shorter total duration (48h of HSLCI imaging) and was analyzed with a legacy pipeline (see Tebon et al v1, bioRxiv 2021). **(A)** Representative images of BT-474 organoids treated with 10 µM staurosporine and 10 µM lapatinib. The white arrow indicates a treatment-resistant organoid. **(B)** Mass distribution of tracked BT-474 organoids by treatment. The left column (pale blue) represents the mass distribution 6 hours post-treatment, while the right column (dark blue) represents the mass distribution 48 hours after treatment. Black horizontal bars represent the median with error bars showing the interquartile range of the distribution. **(C)** Hourly growth rate comparisons (percent mass change per hour) between 50 µM lapatinib and vehicle-treated cells. **(D)** An ATP-release assay was performed on the same plates imaged by HSLCI at the end of imaging. Statistical significance was assessed using an unpaired t- test with Welch's correction. $p<0.05$ is denoted by *, $p<0.01$ is denoted by **, and $p<0.001$ is denoted by ***.

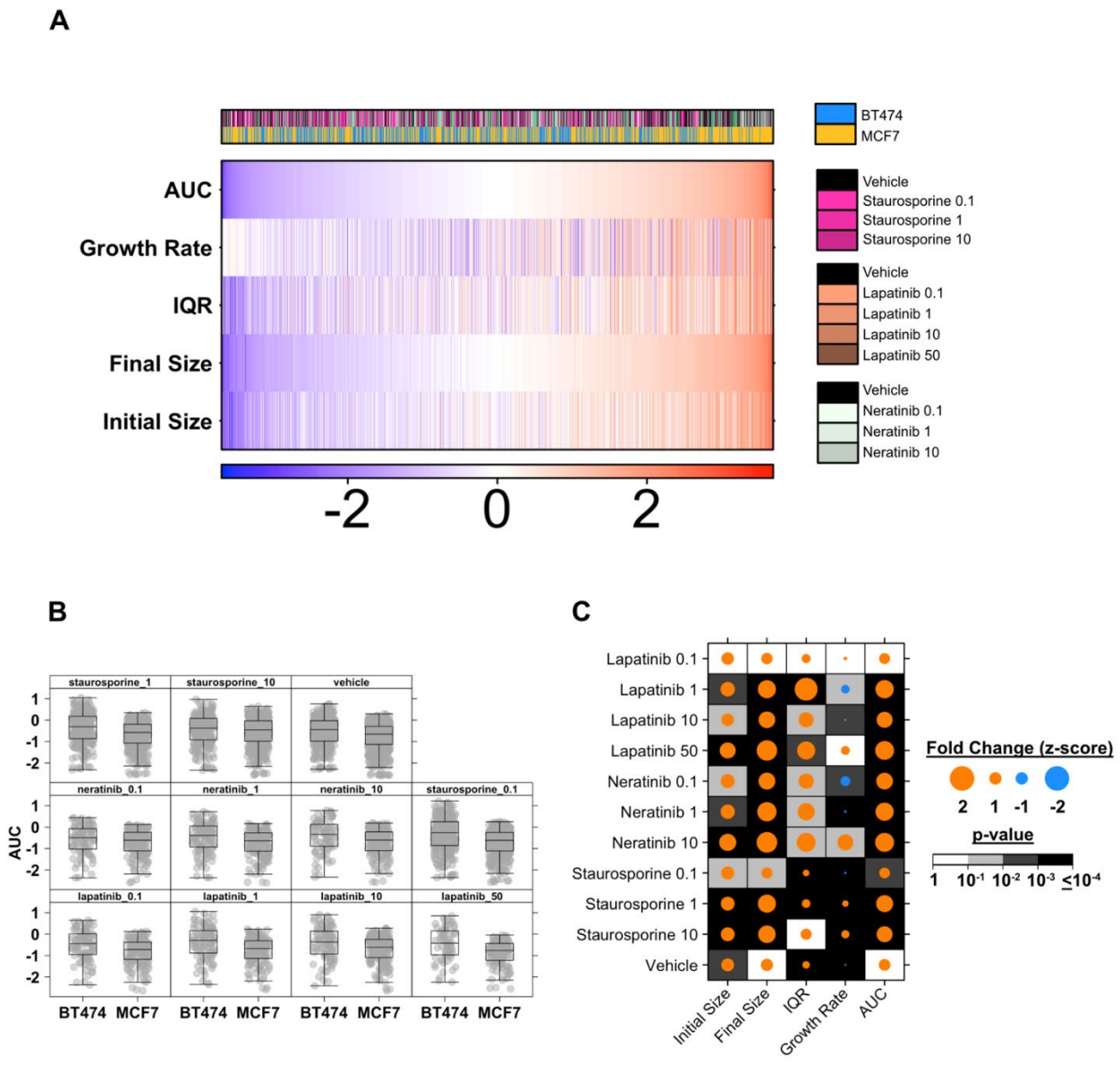

Figure S2.12: Growth patterns of MCF-7 and BT-474 upon pharmacological treatments. We assessed the 3D growth patterns of MCF-7 and BT-474 breast cancer cell lines. Both cell lines were treated with various concentrations of lapatinib, neratinib and staurosporine ranging from 0.1 to 10 μM. **(A)** Growth patterns of tumor organoids are arranged by area under the curve (AUC) metric measured by the integration of a fitted time-series step function. Z-transformed measurements of organoid AUC, linear growth pattern (R^2 of a linear fit), initial size, final size and interquartile range (IQR) varied among sample population. **(B)** Overall growth patterns measured as AUC differed among each treatment condition. **(C)** Fold change of growth patterns features were found to be significantly different among MCF-7 and BT-474 in all conditions.

Supplementary Tables

Parameter Name	Setting
alpha	0
approxcontrib	FALSE
base_score	0.5
booster	gbtree
colsample_bylevel	1
colsample_bynode	1
colsample_bytree	1
disable_default_eval_metric	FALSE
eta	0.3
feature_selector	cyclic
gamma	0
grow_policy	depthwise
lambda	1
lambda_bias	0
max_bin	256
max_delta_step	0
max_depth	6
max_leaves	0
min_child_weight	1
missing	NA
monotone_constraints	0
normalize_type	tree
nthread	1
num_parallel_tree	1

Parameter Name	Setting
objective	binary:logistic
one_drop	FALSE
outputmargin	FALSE
predcontrib	FALSE
predictor	cpu_predictor
predinteraction	FALSE
predleaf	FALSE
print_every_n	1
process_type	default
rate_drop	0
refresh_leaf	TRUE
reshape	FALSE
seed_per_iteration	FALSE
sample_type	uniform
sampling_method	uniform
scale_pos_weight	1
skip_drop	0
strict_shape	FALSE
subsample	1
top_k	0
training	FALSE
tree_method	auto
tweedie_variance_power	1.5
verbose	1

Table S2.1: Hyperparameters used for XGBoost Classifier. The default hyperparameters were used for all settings.

Resampling	Accuracy	AUC
1	0.926	0.967
2	0.922	0.945
3	0.947	0.984
Average ± SD	0.931 ± 0.013	0.966 ± 0.020

Table S2.2: 3-fold resampling cross-validation scores of the XGBoost classifier. We report model accuracy as the average accuracy and AUC of the three resampled test sets.

A

		6 hours	24 hours		48 hours		72 hours	
MCF-7		Mean mass ± SD	Mean mass ± SD	p-value	Mean mass ± SD	p-value	Mean mass ± SD	p-value
Vehicle	1% DMSO	1.36 ± 0.84	1.56 ± 1.05	-	1.77 ± 1.33	-	1.95 ± 1.61	-
Staurosporine	0.1 μM	1.30 ± 0.84	1.27 ± 0.89	2.11×10^{-5}	1.39 ± 1.07	1.31×10^{-5}	1.44 ± 1.21	2.49×10^{-6}
	1 μM	1.28 ± 0.84	1.18 ± 0.77	1.93×10^{-9}	1.10 ± 0.73	2.24×10^{-17}	1.03 ± 0.70	2.80×10^{-21}
	10 μM	1.30 ± 0.78	1.11 ± 0.69	1.49×10^{-13}	1.01 ± 0.65	6.73×10^{-24}	0.93 ± 0.64	3.24×10^{-30}
Neratinib	0.1 μM	1.47 ± 1.03	1.62 ± 1.18	1	1.86 ± 1.51	1	2.03 ± 1.74	1
	1 μM	1.45 ± 0.96	1.57 ± 1.09	1	1.68 ± 1.22	1	1.79 ± 1.40	1
	10 μM	1.39 ± 1.07	1.30 ± 0.98	0.0036	1.16 ± 0.92	2.90×10^{-9}	0.92 ± 0.77	6.82×10^{-19}
Lapatinib	0.1 μM	1.38 ± 1.03	1.49 ± 1.19	0.9072	1.73 ± 1.47	1	1.79 ± 1.56	1
	1 μM	1.40 ± 0.83	1.61 ± 1.11	1	1.84 ± 1.38	1	2.02 ± 1.69	1
	10 μM	1.29 ± 0.83	1.30 ± 0.98	0.0011	1.42 ± 1.11	0.0013	1.50 ± 1.29	0.0006
Kruskal-Wallis p-value		0.3169	2.21×10^{-22}		4.57×10^{-45}		5.13×10^{-60}	

B

		6 hours		24 hours		48 hours		72 hours	
BT-474		Mean mass ± SD	p-value	Mean mass ± SD	p-value	Mean mass ± SD	p-value	Mean mass ± SD	p-value
Vehicle	1% DMSO	1.12 ± 0.61	-	1.27 ± 0.69	-	1.52 ± 0.84	-	1.77 ± 1.00	-
Staurosporine	0.1 μM	1.10 ± 0.57	1	1.22 ± 0.67	1	1.39 ± 0.82	0.0756	1.56 ± 0.96	0.0093
	1 μM	1.02 ± 0.53	0.0901	0.76 ± 0.39	2.27×10^{-32}	0.63 ± 0.34	1.28×10^{-57}	0.57 ± 0.32	3.03×10^{-62}
	10 μM	1.02 ± 0.51	0.1342	0.79 ± 0.44	1.59×10^{-28}	0.63 ± 0.36	4.55×10^{-56}	0.56 ± 0.32	2.52×10^{-62}
Neratinib	0.1 μM	1.04 ± 0.46	1	0.97 ± 0.44	4.86×10^{-6}	0.97 ± 0.45	5.09×10^{-14}	0.98 ± 0.46	6.93×10^{-18}
	1 μM	1.08 ± 0.54	1	0.98 ± 0.49	4.34×10^{-7}	0.86 ± 0.40	1.19×10^{-20}	0.81 ± 0.36	1.48×10^{-27}
	10 μM	0.92 ± 0.42	0.0043	0.70 ± 0.31	3.73×10^{-21}	0.59 ± 0.28	1.99×10^{-31}	0.53 ± 0.21	4.71×10^{-34}
Lapatinib	0.1 μM	1.05 ± 0.52	1	1.13 ± 0.57	0.2512	1.23 ± 0.61	0.0025	1.31 ± 0.67	1.83×10^{-5}
	1 μM	1.08 ± 0.54	1	1.00 ± 0.49	3.37×10^{-5}	0.96 ± 0.45	1.80×10^{-14}	0.93 ± 0.43	1.70×10^{-21}
	10 μM	1.09 ± 0.47	1	0.91 ± 0.45	7.72×10^{-10}	0.86 ± 0.40	3.31×10^{-20}	0.83 ± 0.41	2.13×10^{-24}
Kruskal-Wallis p-value		0.0007		4.25×10^{-70}		1.38×10^{-141}		7.68×10^{-168}	

Table S2.3: Mass distributions for MCF-7 and BT-474 cancer cells grown in 3D. (A) Comparisons of mean mass of MCF-7 cells and cell clusters calculated via HSLCI. **(B)** Comparisons of mean mass of BT-474 cells and cell clusters calculated via HSLCI. For both (**A**) and (**B**), statistical significance was assessed using Kruskal-Wallis tests. For samples with Kruskal Wallis test p-values lower than 0.05, we performed Mann-Whitney U-tests against the vehicle control at the respective time points. Data are presented in **Figure 2.4B**.

		MCF-7				BT-474			
		3D, Bioprinted	3D, Manually Seeded	2D		3D, Bioprinted	3D, Manually Seeded	2D	
Drug	C_{max}	EC_{50} ± SD	EC_{50} ± SD	EC_{50} ± SD	Kruskal-Wallis p-value	EC_{50} ± SD	EC_{50} ± SD	EC_{50} ± SD	Kruskal-Wallis p-value
Staurosporine	-	0.08 ± 0.03	0.28 ± 0.30	0.40 ± 0.01	0.36	0.14 ± 0.05	0.08 ± 0.11	0.12 ± 0.01	0.89
Neratinib	0.15 µM	3.28 ± 0.26	16.54 ± 0.82	29.61 ± 0.62	0.07	0.08 ± 0.05	0.15 ± 0.07	0.12 ± 0.01	0.80
Lapatinib	4.2 µM	12.60 ± 1.27	9.57 ± 4.43	16.67 ± 7.58	0.80	0.48 ± 0.03	1.07 ± 0.96	0.59 ± 0.26	1

Table S2.4: EC_{50} values of MCF-7 and BT-474 breast cancer models in multiple culture conditions. Comparisons of staurosporine, neratinib, and lapatinib treatment efficacy on MCF-7 and BT-474 breast cancer models in 3D culture following automatic seeding using bioprinting, 3D culture following manual seeding, or 2D monolayer cell culture, as measured by ATP-release assay. Data were obtained from two to three independent experiments. All concentration values are shown in µM. EC_{50} values were computed using data points from all tested concentration conditions, including 50 µM neratinib that was excluded from HSLCI analyses due to drug precipitation that resulted in unquantifiable phase images. Statistical significance was assessed using Kruskal-Wallis tests. For all model-drug combinations, no significant differences were observed in average EC_{50} values among different culturing methods. The peak serum concentrations (C_{max}) of neratinib and lapatinib as reported in Keyvanjah et al, 2017 and Liston et al, 2017 respectively are included for reference.

A

MCF-7		Time (h)	n	Organoid Behavior (%)		
				Gained Mass	Stable	Lost Mass
Vehicle	1% DMSO	12	800	23.2	67.4	9.4
		24	794	44.8	36.0	19.1
		48	764	48.6	24.1	27.4
		72	715	50.8	16.6	32.6
Staurosporine	0.1 µM	12	481	8.7	72.3	18.9
		24	481	21.8	46.8	31.4
		48	458	31.7	27.3	41.0
		72	436	32.8	20.4	46.8
	1 µM	12	508	10.2	74.6	15.2
		24	505	11.7	56.6	31.7
		48	490	13.7	36.9	49.4
		72	460	10.0	31.3	58.7
	10 µM	12	539	6.9	64.7	28.4
		24	538	8.4	40.3	51.3
		48	523	9.0	22.9	68.1
		72	494	8.3	16.2	75.5
Neratinib	0.1 µM	12	205	19.5	67.3	13.2
		24	206	43.7	38.8	17.5
		48	196	49.5	27.0	23.5
		72	184	49.5	21.7	28.8
	1 µM	12	222	18.0	71.6	10.4
		24	221	37.6	45.2	17.2
		48	214	44.4	30.8	24.8
		72	203	46.3	24.6	29.1
	10 µM	12	223	14.3	68.6	17.0
		24	219	12.8	51.1	36.1
		48	213	8.0	34.3	57.7
		72	199	4.5	18.1	77.4
Lapatinib	0.1 µM	12	218	21.1	66.5	12.4
		24	214	35.5	43.5	21.0
		48	203	42.9	24.6	32.5
		72	187	43.3	22.5	34.2
	1 µM	12	202	17.8	69.8	12.4
		24	202	47.5	33.2	19.3
		48	190	55.3	21.1	23.7
		72	177	53.7	21.5	24.9
	10 µM	12	251	15.5	62.5	21.9
		24	252	32.5	31.0	36.5
		48	238	36.1	18.9	45.0
		72	220	37.7	10.0	52.3

B

BT-474		Time (h)	n	Organoid Behavior (%)		
				Gained Mass	Stable	Lost Mass
Vehicle	1% DMSO	12	419	30.1	59.9	10.0
		24	415	62.4	26.7	10.8
		48	409	80.9	10.8	8.3
		72	387	80.9	7.2	11.9
Staurosporine	0.1 μM	12	335	31.0	55.2	13.7
		24	334	49.7	38.3	12.0
		48	334	65.9	17.7	16.5
		72	327	72.8	11.0	16.2
	1 μM	12	277	11.9	39.0	49.1
		24	276	10.9	19.9	69.2
		48	275	5.5	12.0	82.5
		72	266	2.6	9.4	88.0
	10 μM	12	276	11.6	47.5	40.9
		24	273	12.1	24.9	63.0
		48	273	6.6	13.9	79.5
		72	266	4.5	7.9	87.6
Neratinib	0.1 μM	12	121	14.9	57.0	28.1
		24	120	15.0	40.8	44.2
		48	121	20.7	34.7	44.6
		72	116	28.4	22.4	49.1
	1 μM	12	132	12.9	56.8	30.3
		24	131	15.3	37.4	47.3
		48	131	10.7	22.1	67.2
		72	128	7.0	22.7	70.3
	10 μM	12	103	12.6	42.7	44.7
		24	106	8.5	30.2	61.3
		48	105	4.8	8.6	86.7
		72	103	0.0	7.8	92.2
Lapatinib	0.1 μM	12	125	22.4	64.8	12.8
		24	126	42.1	45.2	12.7
		48	124	66.9	19.4	13.7
		72	117	69.2	17.9	12.8
	1 μM	12	126	12.7	65.1	22.2
		24	126	18.3	39.7	42.1
		48	125	18.4	29.6	52.0
		72	126	18.3	25.4	56.3
	10 μM	12	122	11.5	57.4	31.1
		24	122	9.8	27.0	63.1
		48	118	11.9	17.8	70.3
		72	114	11.4	14.9	73.7

Table S2.5: Proportions of organoids that gained, lost, and maintained mass by treatment condition. (A) Percentage of tracked MCF-7 cell clusters in each condition that gained more than 10% of their initial mass (green), lost more than 10% of their initial mass (black), or maintained a mass within 10% of their initial measured value (gray) at 12, 24, 48, and 72 hours after treatment addition. **(B)** Percentage of tracked BT-474 organoids in each condition that gained more than 10% of their initial mass (green), lost more than 10% of their initial mass (black), or maintained a mass within 10% of their initial mass (gray) at 12, 24, 48, and 72 hours after treatment addition. Data are plotted in **Figure 2.5A**.

		MCF-7		BT-474	
		Viability ± SD	p-value	Viability ± SD	p-value
Vehicle	1% DMSO	1.00 ± 0.22		1.00 ± 0.22	
Staurosporine	0.1 µM	0.50 ± 0.08	<0.0001	0.78 ± 0.09	0.0006
	1 µM	0.17 ± 0.04	<0.0001	0.04 ± 0.01	<0.0001
	10 µM	0.13 ± 0.04	<0.0001	0.01 ± 0.00	<0.0001
Neratinib	0.1 µM	1.02 ± 0.15	0.8463	0.40 ± 0.10	<0.0001
	1 µM	0.92 ± 0.12	0.4623	0.25 ± 0.04	<0.0001
	10 µM	0.08 ± 0.01	<0.0001	0.13 ± 0.05	<0.0001
Lapatinib	0.1 µM	1.00 ± 0.04	0.9452	0.64 ± 0.11	0.0004
	1 µM	1.01 ± 0.05	0.8598	0.38 ± 0.08	<0.0001
	10 µM	0.66 ± 0.08	0.0018	0.26 ± 0.03	<0.0001
	50 µM	0.14 ± 0.04	<0.0001	0.01 ± 0.00	<0.0001

Table S2.6: Organoid viability analysis by endpoint ATP assay. Comparisons of cell viability measured by ATP assay. P-values calculated by unpaired t-test with Welch's correction. Data are presented in **Figure 2.5B**.

Supplementary Videos

Video S2.1: MCF-7 organoids treated with vehicle control. Scan the QR code to access the video or visualize at the following link: https://youtu.be/bUBq-ZChFM0

Video S2.2: BT-474 organoids treated with vehicle control. Scan the QR code to access the video or visualize at the following link: https://youtu.be/AzSc8WW5KBA

Acknowledgements

We would like to acknowledge the UCLA Translational Pathology Core Laboratory and the UCLA Technology Center for Genomics and Bioinformatics for their assistance with this work. Additionally, we would like to thank Dr. Steven Jonas for his generous access to laboratory equipment. This work was supported by NIH R01CA244729 and R01CA244729-03S1 (to A.S. and P.C.B.) a JCCC Fellowship (to P.J.T.), a National Science Foundation Graduate Research Fellowship (DGE-2034835, to B.W.), a Eugene V. Cota Robles Fellowship (to B.W.) a UCLA DGSOM Seed Award (to A.S. and P.C.B.), the Air Force Office of Scientific Research (FA9550-15-1-0406, to M.A.T.), the Department of Defense (W81XWH2110139, to M.A.T.). It was additionally supported by NIH U24CA248265 (to P.C.B.) and NIH R01GM114188, R01GM073981, R01CA185189, R21CA227480, R01GM127985, and P30CA016042 (to M.A.T.). A.S., P.J.T., N.T., B.W., and M.A.T. are inventors on a patent application (U.S. Patent Application No. 18/037,646) filed by The Regents Of The University Of California covering some aspects of the bioprinting process. A.S. and P.C.B. are the founders and owners of Icona BioDx. All other authors declare no competing interests.

Chapter 3: Label-free interferometry platform for drug response profiling of bioprinted tumor organoids at single-organoid resolution

Introduction

Tumor organoids are three-dimensional (3D) multicellular structures derived from cancer cells that grow and self-organize within an extracellular matrix (ECM) to recapitulate the 3D architecture and molecular features of the tumor tissue of origin[19]. Due to their tractability for experimental manipulations and efficiency of derivation from many tumor types and tissue sources[19,20,27,28,171], they have become useful research tools for applications including disease modelling[16,19,171], drug discovery[19–21], and personalized medicine[19,27–29]. There is increasing interest in using patient-derived tumor organoid (PDTO) models for functional precision medicine (FPM), involving *ex vivo* testing of patient-derived tumor material to predict drug efficacy[1,25,29]. This approach is motivated by growing evidence that drug responses in PDTOs are concordant with patients' responses to treatments across a number of cancer types[27,28,39,41]. The accuracy of therapeutic predictions provided by any FPM drug screening approach depends on the drug testing platform and readouts adopted, and therefore there is a critical need to develop robust, scalable drug screening strategies using 3D organoid models of cancer, and to validate these strategies for individualized therapy selection[1,25,29].

Quantitative phase imaging (QPI) is a set of label-free, wide-field microscopy methods that measure the phase shift of light as it passes through the height of a transparent biological sample in the z -direction[45]. Using QPI, a two-dimensional (2D) phase shift map of single cells or cell clusters within each imaging field of view (FOV) can be reconstructed for multiparametric quantitative analyses, including measurements of cell growth and biomass accumulation or loss in response to drug treatment[45]. The measured phase shift is directly proportional to the dry

biomass content of the biological sample; dry biomass can be calculated from the measured phase shift using the following equation (4)

$$m = \frac{1}{\alpha}\int \phi\lambda dA \tag{4}$$

where m is dry biomass, Φ is the measured phase shift as a fraction of wavelength, λ is illumination wavelength, integration is performed over the area A of imaged objects, and α is the specific refractive increment, defined as the slope of the relationship between the refractive index and biomass concentration of a solution[45]. Because the specific refractive increment of both whole mammalian cells and the proteins, lipids, sugars, and nucleic acids that constitute the bulk of their biomass fall within a narrow range, 1.8–2.0 × 10^{-4} m^3/kg, α can be assumed to have a constant average value within this range over live-cell imaging time scales[45]; in our analyses of previous QPI experiments, we used α = 1.8 × 10^{-4} m^3/kg[45,58,66,71,137]. QPI is of interest for applications in FPM because it is conducive to long-term and time-resolved imaging studies of cells and cell clusters[58,59,66,71,74,76]. Through its capacity to elucidate single cell–level growth and drug response data, it can readily quantify response heterogeneity and identify rare subpopulations of drug-sensitive and drug-resistant cancer cells within larger cell populations[58,66,71,74,76]. Biomass measurements are especially useful for FPM because they are direct indicators of cell fitness. Unlike other biophysical measurements such as volume or shape, changes in biomass accumulation dynamics directly result from changes in the balance of biosynthetic and degradative cellular processes[45,49,172]. Moreover, treatment-induced growth rate changes are relevant to the development of drug resistance[67].

Our group previously developed high-speed live cell interferometry (HSLCI), a high-throughput, label-free optical imaging platform, for repeated QPI to enable massively parallel, highly time-resolved monitoring of cellular biomass accumulation or loss dynamics in thousands

of discrete 2D cellular entities with picogram sensitivity[66,71]. More recently, we developed a unique approach to apply HSLCI for high throughput drug screening of tumor organoid models by incorporating 3D bioprinting[173] to generate models in a modified geometry favorable for both efficient imaging and compatibility with automation for drug screening (**Figure 3.1A**). Our published platform includes a downstream analysis pipeline implementing machine learning (ML) tools to analyze acquired HSLCI datasets, which enabled quantification of biomass dynamics in response to targeted drug treatments for thousands of organoids at single-organoid resolution[174] (**Figure 3.1A**). Our complete protocol generates organoid growth and drug response data within one week of organoid establishment[174], which is compatible with therapeutic decision-making timeframes and functional precision medicine efforts, and could be leveraged clinically[27,174]. In this protocol, we present a detailed list of core components and instructions for assembling the HSLCI platform and preparing it for high-throughput QPI. We present step-by-step instructions for automatically bioprinting cells in ECM in defined patterns within the wells of 96-well glass-bottom plates to establish 3D cultures of human cancer organoids or 3D models for high throughput studies using the HSLCI platform (**Figure 3.1B**). We provide specific details for culturing plates of bioprinted 3D models established from cancer cell lines, and for performing automated drug treatments and label-free, high-throughput QPI using the HSLCI platform, as well as validation combining a conventional endpoint ATP release assay (**Figure 3.1B**). Our bioprinting method generates organoids that grow robustly within drug screening experimental timeframes without altering the histopathological or molecular features of cancer cells[174]. Finally, we provide details on running the downstream, open-source pipeline for analyzing large datasets of HSLCI-acquired phase images and quantifying drug responses against chemotherapies, targeted therapies, and biologics. We include examples in which we identified rare drug response phenotypes within single organoid-resolution data[174].

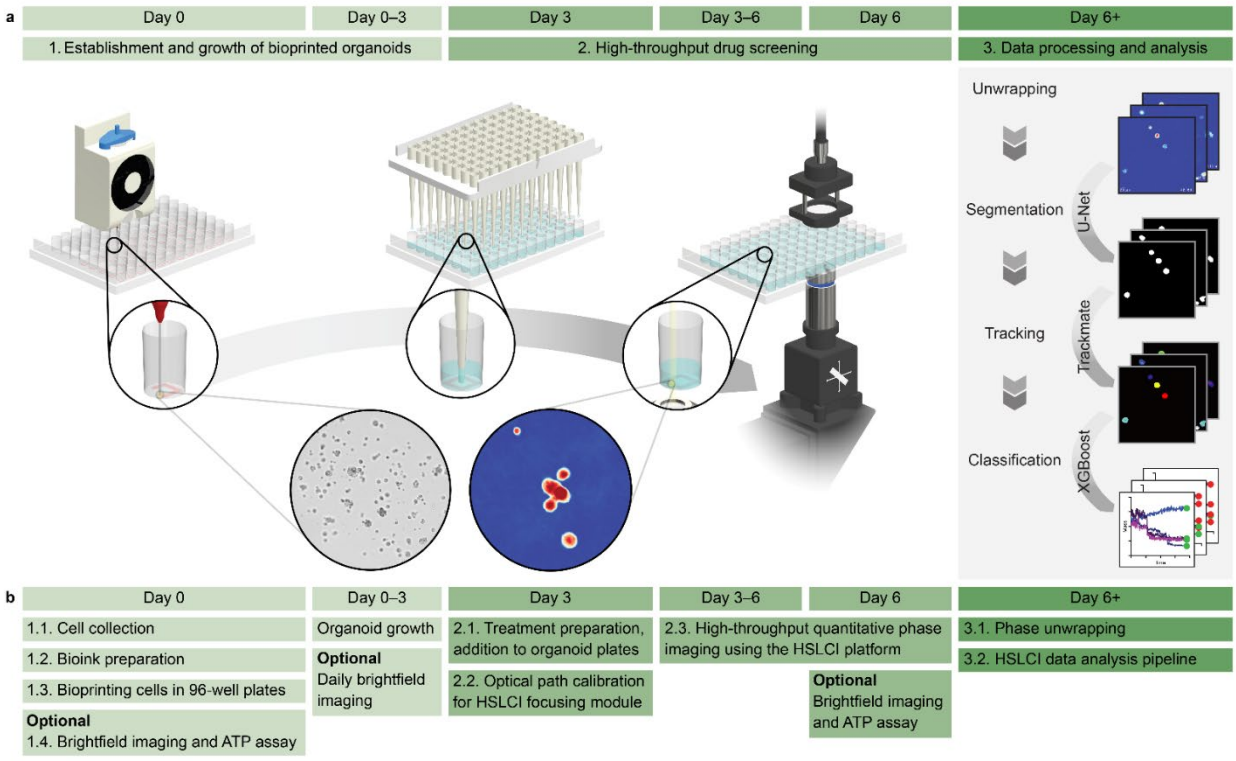

Figure 3.1: Overview of organoid bioprinting, high-throughput drug screening, and analysis workflows. (A) Overview of the central high-throughput drug screening workflow (Procedures 1–3) for obtaining highly time-resolved organoid-level biomass change and drug response data. Extrusion-based bioprinting is used to seed organoid models of cancer as cells in uniform, single-layer Matrigel constructs in a 96-well glass-bottom plate (Day 0). Organoid model establishment and growth (Days 0–3) can be monitored through brightfield imaging before automated addition of drug-treated media (Day 3). After treatment, organoid plates are transferred to the high-speed live cell interferometry (HSLCI) platform for three days of high-throughput, label-free quantitative phase imaging (QPI; Days 3–6). At the conclusion of HSLCI imaging (Day 6), brightfield imaging is performed at a final timepoint, followed by an endpoint ATP assay to validate HSLCI drug screening results. HSLCI illuminates the bioprinted organoid-laden constructs using coherent light and repeatedly captures interferograms at 1000+ fields of view (FOVs) per experiment, which can be converted into phase shift images in a process called phase unwrapping. From measured phase shifts, the biomass of individual organoids was calculated and tracked over time to characterize growth and response to treatment (Day 6+). Reprinted with permissions from Tebon et al, 2023. **(B)** Graphical summary of the main experimental workflows for bioprinted tumor organoids. The methods are split into three main procedures: (1) bioprinting to establish 3D organoid models of cancer in 96-well glass-bottom plates, (2) high-throughput drug screening of bioprinted organoids using the HSLCI platform, and (3) multistep, automated analysis of the acquired QPI data.

Development of the protocol

We previously developed the HSLCI platform with the aim of achieving a sufficiently high combination of imaging throughput, time resolution, and sampling depth necessary for a functional assay of drug sensitivity that can decipher the heterogeneity of cancer models. We built a scanning interferometry system using a quadriwave lateral shearing interferometry (QWLSI) camera because, among other advantages, QWLSI is a QPI modality that is compatible with an automated, linear plate scanning device[66]. The current HSLCI configuration (**Figure 3.2A–B**) we use consists of a QWLSI camera (SID4 Bio, Phasics) coupled to a custom-built inverted optical microscope with a 40× objective (CFI Plan Fluor 40X, NA 0.75, Nikon) and a plate holder that fits a 128×85 mm standard-footprint multi-well plate[174]. The camera consists of a charge-coupled device (CCD) image sensor (IGV-B2020, Imperx) fitted with a modified Shack-Hartmann mask that splits the incident wave front into four replica wave fronts that interfere with one another. The resulting interferograms are recorded, and after phase unwrapping, can be deconvoluted in the Fourier domain and used to reconstruct a phase shift map, in turn enabling dry biomass calculations of discrete objects in an imaging FOV[100]. Sample illumination is provided by a collimated 660 nm LED light source (ThorLabs), and the plate holder is secured to three linear translation stages (ThorLabs) that control movement of the biological samples of interest along three orthogonal movement axes (**Figure 3.2A–B**). To enable automated, high throughput image acquisition, we constructed the HSLCI optical configuration with an autofocusing system that incorporates a custom-built, automatic feedback control mechanism coupled to a one-dimensional piezo actuator on which the microscope objective is mounted. This setup enables continuous imaging at a constant, user-determined focal height by ensuring that the distance between the objective and the glass bottom surface of the sample plate is automatically kept constant during lateral plate scanning (**Figure 3.2C**). Finally, we installed the HSLCI platform

inside of a standard, non-humidified cell culture incubator (Steri-Cult, Thermo Scientific) to enable long-term imaging of samples in standard cell culture conditions of 37°C and 5% CO_2[66].

To address the clinical need for scalable organoid screening strategies to guide treatment selection in patients with cancer, we sought to develop a method for high throughput drug screening of organoid models of cancer using the HSLCI platform[174]. Common 3D seeding approaches severely impede imaging efficiency by generating organoid models in thick domes or droplets of an ECM[19,77,78,174], resulting in structures growing at random positions throughout the full thickness of the matrix[77,78,174]. In these seeding geometries, images at a single focal plane include many organoids at z-heights that are out of focus[44,77,78,174], and organoids at different z-heights often physically overlap with one another within imaging FOVs, causing difficulties in interpreting discrete objects in images[78,174]. Furthermore, in thicker layers of ECM, such as those achieved by manual organoid seeding methods, image quality is adversely affected by light scattering[21,45,78,174].

To overcome these challenges, we introduced 3D bioprinting to automatically seed cancer cells in Matrigel in ultra-thin, flat “mini-square” constructs with typical thicknesses of approximately 70 μm (**Figure 3.3A–H**), a geometry that enables efficient imaging of thousands of organoids per experiment on the HSLCI platform[174] and facilitates the use of liquid handlers and automation for drug treatment protocols[27,174]. This protocol for organoid establishment, 3D culture, and drug screening (**Figure 3.1A–B**) is a modification of our prior mini-ring drug screening platform, in which organoids are grown from cells seeded in thin rings of Matrigel around the rims of each well of 96-well plates[20,27,28,38,171,174]. We bioprinted cells in a Matrigel-based bioink because embedded cells can interact with microenvironment components in Matrigel to create physiologically representative tumor models[19,31,136]. The empty center of each well due to the square geometry is essential to perform robust and automated high throughput drug screening[20,27,28,38,171,174].

We aimed to print thin, flat constructs because HSLCI cannot generate interpretable quantitative information from out of focus objects, and imaging efficiency is reduced by organoids moving orthogonally to the focal plane during experiments[174]. We tested a range of bioprinting conditions in attempts to maximize consistency in patterning temperature-sensitive Matrigel-based bioink. We determined that the use of oxygen plasma treatment to modify the glass

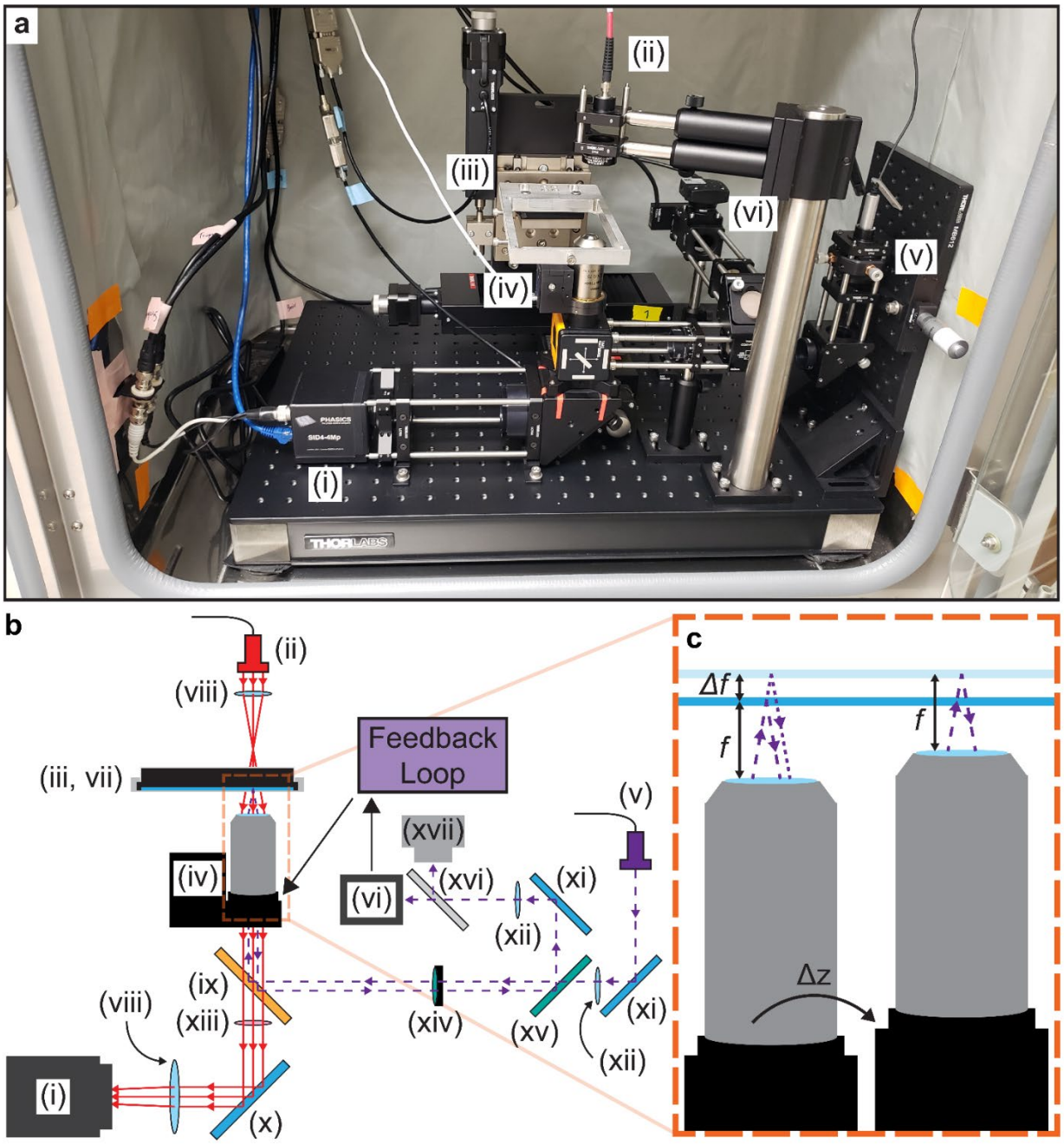

Figure 3.2: Overview of high-speed live cell interferometry (HSLCI) system configuration. (A) Image of HSLCI system hardware. The HSLCI system is assembled inside of a non-humidified cell culture incubator to enable long-term imaging of biological samples in conditions that approximate physiology. Labeled components include (i) a quadriwave lateral shearing interferometry (QWLSI) camera for wide-field phase detection, (ii) a collimated 660 nm LED illumination source, (iii) a 96-well plate holder with movement in the x-, y-, and z- directions controlled by three stepper motors, and (iv) a 40× objective coupled to a piezo actuator that is used for continuous focus adjustment during scanning and imaging of the sample plate. (v) A 980 nm infrared (IR) laser secured to an adjustable mount and (vi) a quadrant photodiode detector (QPD) are also used in the HSLCI system's autofocusing mechanism. **(B)** Diagram showing HSLCI system hardware and optical paths. Solid red arrows indicate the light path of the 660 nm illumination LED. Phase images are acquired using a QWLSI camera. Dotted purple arrows indicate the light path of the 980 nm IR laser used for dynamic focus control during plate scanning. Labeled parts include (i–vi) in addition to (vii) a 96-well glass-bottom plate containing biological samples for imaging, (viii) two focusing lenses for imaging, (ix) a dichroic mirror, (x) a 2" reflecting mirror, (xi) two 1" reflecting mirrors, (xii) two adjustable focusing lenses, (xiii) a hot mirror, (xiv) a quarter-wave plate, (xv) a polarizing beam splitter, and (xvi) a 90/10 beamsplitter that reflects 10% of the IR laser signal directed toward the QPD at (xvii) a USB camera for user visualization of this signal. **c,** Schematic showing the autofocusing mechanism that is built into the HSLCI system. Focus is maintained throughout automated plate scanning and high-throughput quantitative phase imaging by using a feedback loop to maintain the distance (f) between the microscope objective and the glass bottom of the multi-well plate. Changes in this distance (Δf) are detected using an IR laser and a QPD, and a piezo actuator coupled to the objective sensitively and precisely compensates for any detected changes by adjusting the position of the objective in the z-axis (Δz).

surfaces of 96-well glass-bottom assay plates was essential to obtain constructs of Matrigel bioink that adhered to the bottom of wells and maintained structural integrity over the duration of a drug screening experiment[174], with oxygen radicals chemically functionalizing the plate well surface to increase its hydrophilicity and wettability[106]. We achieved additional control over deposition patterns by using 3D printed masks during oxygen plasma treatment to selectively modify the glass substrate and, in turn, to guide the spreading of the bioink into contiguous square-shaped constructs desired for downstream imaging and drug screening applications (**Figure 3.3A–B**). We seeded cells into successive wells ordered in a snaking pattern to minimize the time interval between successive bioprinter extrusions, and to maximize volume consistency of Matrigel bioink

and the number of cells seeded into each well across an entire 96-well glass-bottom plate (**Figure 3.3C–E**). Furthermore, we seeded into the outermost wells relatively earlier during the bioprinting procedure to minimize temperature-dependent variations across the inner 60 wells, which are the wells selected for high throughput drug screening and HSLCI imaging (**Figure 3.3D–E**). When necessary, before beginning the subsequent high throughput drug screening workflow, we performed post-print ATP assays to confirm the consistency in bioink volumes and cell seeding densities across entire plates (**Figure 3.1B**, **Figure 3.3E**). We typically include whole-well brightfield imaging (**Figure 3.3C**, **Figure 3.3F**) to confirm that the bioprinting protocol generated the desired geometry, with squares whose legs are parallel to the edges of the plate. By aligning the legs of the mini-square constructs with the movement of the plate during imaging on the HSLCI platform (**Figure 3.3G–H**), we maximized the number of imaging FOVs with focused objects trackable over time.

To optimize imaging throughput, time resolution, and sampling depth, we repeatedly scanned a sample plate four times at 6 mm/s along each of six columns of wells while the camera and LED illumination were concurrently triggered for imaging at eight frames per second. These imaging parameters enabled collection of about 25 unique images per well in the interior 60 wells (wells B2–G11) of each 96-well plate of bioprinted organoids, or about 1,500 unique FOVs per experiment, with a typical imaging interval of 10 minutes between successive frames at the same FOV. We skipped scanning and collecting data from wells on the edge of the 96-well plate both due to geometric constraints and the greater propensity for media to evaporate during long term experiments. Furthermore, immediately prior to each organoid imaging experiment using the HSLCI platform, we acquired reference interferograms required for phase unwrapping and downstream data analysis. Because the 2D phase shift maps generated from phase unwrapping represent the total optical path difference at each pixel caused by a combination of the sample and the optics of the imaging system, we captured these images in intact, cell-free FOVs

overlapping with one of the subsequent scanning interferometry imaging paths across the bioprinted mini-square constructs (**Figure 3.3G–H**). Non-negligible differences in the contribution of the imaging setup to the computed phase shifts from FOVs in opposite legs of bioprinted mini-square constructs necessitated acquisition of at least two suitable reference FOVs – one overlapping with the user-programmed imaging paths closer to the wells of column A, and one overlapping with those closer to the wells of column H (**Figure 3.3G–H**).

Lastly, we developed a custom downstream analysis workflow to overcome challenges in data analysis specific to our imaging platform (**Figure 3.1A**). First, we unwrapped HSLCI-acquired interferograms into phase images using the manufacturer's software in a custom-written script. We saved successive frames from each imaging FOV in a single experiment into one image stack in a .mat file; this output file format was necessary to prevent severe slowdowns in analysis due to an excessive number of files in each dataset. We then implemented a custom, multistep data analysis pipeline, in which outputted phase images from each FOV are background-corrected by subtracting noise from refractive aberrations, and then organoids are segmented and integrated over their area to calculate their dry biomass before being tracked in each time course image stack and analyzed for biomass accumulation and loss dynamics in response to drug treatment (**Figure 3.1A**). We found that threshold-based image segmentation algorithms that are standard for images of cells in 2D were not readily applicable to more complex imaging datasets of 3D organoids[44,78,175]. Because segmentation of 3D organoid imaging datasets usually requires adaptation of ML algorithms by training them to recognize desired objects in the specific organoid imaging dataset[44], we applied a U-Net convolutional neural network (CNN) algorithm[20,119] to segment organoids in large, feature-rich HSLCI imaging datasets prior to tracking organoids through time course image stacks[174]. We used the TrackMate program for tracking organoids through time course image stacks because of the multiparametric information provided for each object track[176,177]. Finally, when imaging with the QWLSI camera, interpretable quantitative

information cannot be acquired from out of focus objects, and imaging efficiency is reduced by organoids moving orthogonally to the focal plane during experiments[100]. We determined that an additional ML-based track classification algorithm was necessary to exclude tracks of out of focus

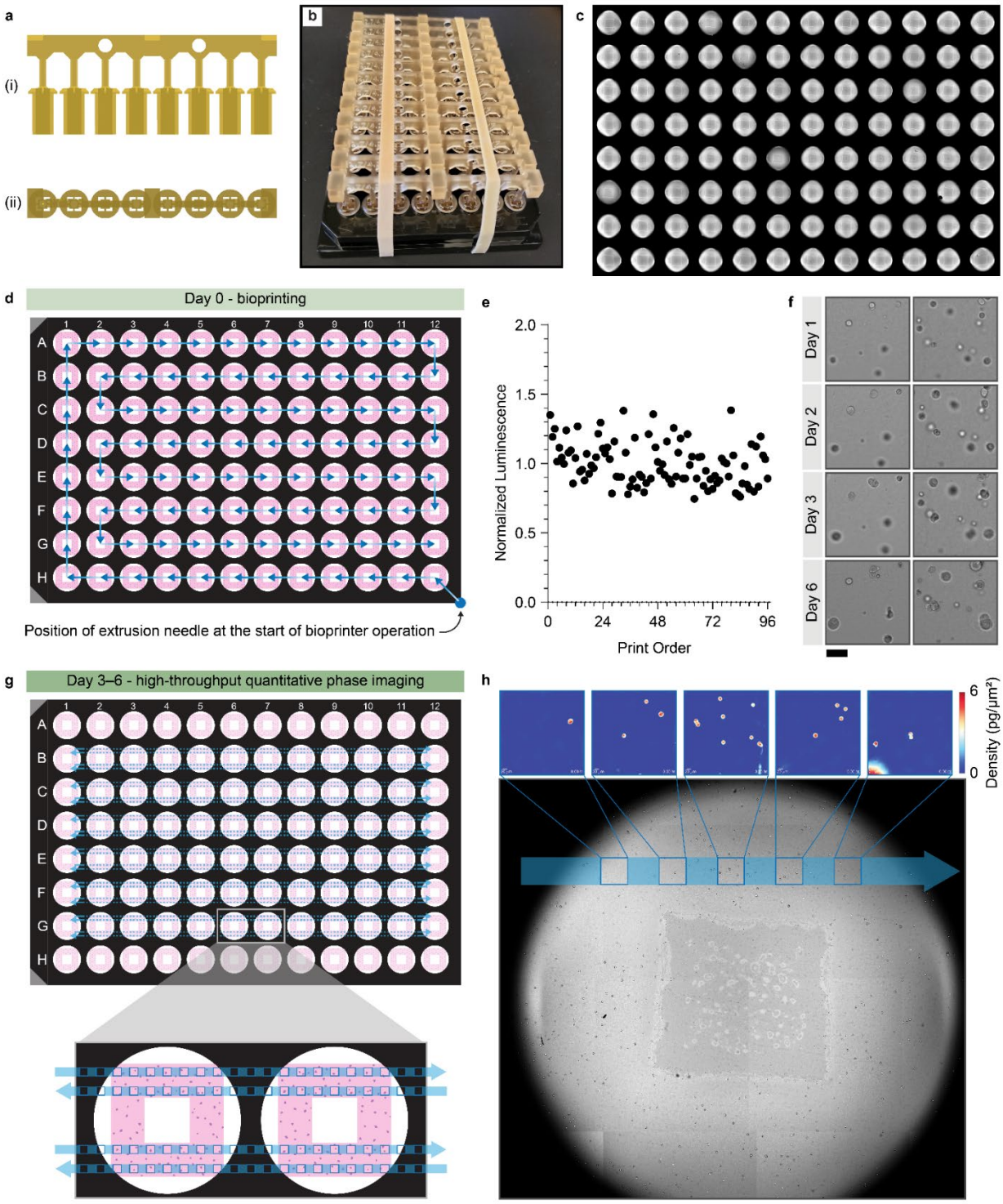

Figure 3.3: Key steps in organoid bioprinting and high-throughput drug screening workflow. **(A)** Schematic of well masks used for patterning oxygen plasma treatments of 96-well glass-bottom plates to facilitate bioprinting in the desired geometry for high-throughput quantitative phase imaging on the HSLCI platform. Individual constructs consisting of masks for a row of 8 wells are shown, (i) viewed from the side and (ii) from the bottom. Reprinted with permissions from Tebon et al, 2023. **(B)** Image of well masks inserted and secured into the wells of a glass-bottom 96-well plate. Well mask constructs are inserted into each of columns 1–12 and secured using rubber bands. **(C)** Whole-well brightfield images of a 96-well plate acquired immediately after bioprinting, with BT-474 cell-laden Matrigel bioink deposited in thin, flat, square-shaped constructs into each of 96 wells for organoid model establishment and high-throughput drug screening. Images are stitched together to recreate the relative positions of the bioprinted constructs in each well, and contrast-enhanced for clarity. Reprinted with permissions from Tebon et al, 2023. **(D)** Schematic depicting key bioprinting parameters for 96-well glass-bottom plates including the desired square-shaped geometry for seeding Matrigel-laden cells within each circular well, the order in which bioink is extruded into each well, and the xy-positioning of the 25G extrusion needle during plate calibration, which sets the origin of the bioprinter's movement coordinates. **(E)** Post-print ATP-catalyzed luminescence readings from each well of a representative 96-well plate of BT-474 cells (**C**), normalized to the average of all luminescence measurements from the plate and sorted by the order in which each well was seeded with cell-laden Matrigel bioink. The coefficient of variation (CV%) for the plate shown is 15.6%. Adapted with permissions from Tebon et al, 2023. **(F)** Representative brightfield images of MCF-7 cell line–derived organoids taken 1-, 2-, 3-, and 6-days after seeding by bioprinting. 3D multicellular organoids increase in size and prevalence with culture time. Scale bar is 50 μm. **(G)** Schematic showing the raster scanning pattern of the translation stages carrying a 96-well plate of bioprinted organoids during each complete, pre-programmed imaging loop in a HSLCI experiment. The inset depicts a magnified view of the arrangement of imaging FOVs corresponding to sequential scans in two adjacent wells from the same column, overlaying the position of the square-shaped Matrigel constructs which contain the organoids of interest. Arrows represent the direction of each individual scan down a column of wells, and open squares represent unique imaging FOVs over the duration of a single HSLCI imaging experiment. The coordinates of plate scans are user-inputted such that scans are parallel to the long axis of the sample plate and the majority of FOVs overlap with the legs of thin, flat, square-shaped Matrigel constructs containing organoids of interest. In a typical experiment, ~25 unique FOVs across the interior 60 wells of a 96-well plate are repeatedly imaged, with an interval of 10 minutes between successive frames. **(H)** Brightfield image of a single well containing BT-474 cells seeded by bioprinting, overlaid with the HSLCI imaging path and five corresponding phase shift images of these cells. Bioprinting enables seeding of Matrigel-encapsulated cells in geometries optimized for efficient imaging using the HSLCI platform. Adapted with permissions from Tebon et al, 2023.

organoids for which calculation of biomass and other quantitative metrics using QPI data cannot be assumed to be accurate[124,174].

Comparison with other methods

A feature of our organoid bioprinting and high throughput drug screening protocol that advantageous for potential applications in FPM is the automatic seeding of temperature-sensitive ECM bioink in a 96-well plate such that 3D models can consistently be screened in under one week, a clinically relevant timeframe[27,174]. The protocol that we present is adaptable to a range of 3D organoid models, including PDTOs from multiple cancers. Compared to traditional drop-seeding techniques, our mini-ring and mini-square methods enables seeding of less Matrigel and fewer cells in each well, enabling conservation of expensive reagents and cells of potentially limited availability[20,27,28,38,171,174]. This feature is highly desirable for future adaptations of this workflow toward drug screening of 3D PDTOs for FPM applications[27,174].

Furthermore, whereas other groups have developed protocols to bioprint organoid models with culturing in 3D for downstream drug efficacy assessments[144–146], these systems, like most existing organoid screening strategies, use endpoint chemosensitivity assays that outputs drug sensitivity results at a single timepoint as well-level averages[27,44,77,174]. Lack of temporal, organoid-level information can mask growth rate variations resulting from differences in the fraction of cells or organoids that grow, and in turn prevent identification of sample heterogeneity in drug responses[78,174,178], including potentially clinically relevant adaptive changes upon treatment[67,178]. By contrast, high-content imaging assays, which extract quantitative information from individual organoids or their constituent cells[44,77,178,179] can reveal dynamic features of drug responses[178,180]. However, most live cell imaging platforms require fluorescent labeling, which can limit data collection times and potentially alter cellular behavior through phototoxicity[44,179]. Compared to existing label-free organoid imaging modalities[63,77,154,180,181], HSLCI coupled to bioprinting and ML is unique in its combination of throughput, time resolution, and number of

organoids analyzed per experiment, and is advantageous in its ability to quantify growth, drug response heterogeneity, and resolve rare phenotypes among drug response profiles[174].

Limitations

While the protocol described here has many applications, limitations remain for each main procedure. A key limitation of the bioprinting protocol is that bioprinting of temperature-sensitive ECM bioinks can be technically challenging[145,174]. Matrigel undergoes time- and temperature-sensitive gelation above a temperature of 6–8°C[135,136], and the bioprinter used in our protocol did not have sufficient temperature control for printing temperature-sensitive Matrigel bioink in the liquid phase. In practice, cell seeding using our bioprinting protocol necessitated that extrusion pressures be adjusted with each print. Without strict temperature control during the bioprinting protocol, pneumatic extrusion may still result in unacceptably high time- and temperature-dependent changes in viscosity over the duration of a single bioprinted plate (see Troubleshooting). Furthermore, shear stress is inherently a potential technical source of variability during extrusion bioprinting, and changes in bioprinting parameters may introduce enough shear stress during cell seeding to adversely affect organoid model establishment[108,136].

The HSLCI platform achieves its throughput and sampling depth by imaging a large number of FOVs at a single focal plane relative to the plate bottom surface, automatically recording 2D projections of the phase shift of incident light caused by cultured cells or organoids[66,174]. However, because these 2D phase shift maps can only provide accurate biomass information for objects in focus[100,142], applying HSLCI for imaging 3D cultured tumor organoids capable of moving orthogonal to the focal plane inherently limits efficiency. When bioprinting cell-laden Matrigel ECM constructs for HSLCI imaging, additional thickness in the z-direction results in a relatively greater fraction of imaged objects staying in focus over the duration of imaging, and therefore greatly decreases sampling depth. During HSLCI imaging, we could not repeat drug treatments (as performed daily in our conventional mini-ring pipeline[20,27,28,38,171]) because doing

so would interrupt imaging, preventing continuous tracking of organoids. Furthermore, unlike QPI images of discrete cells in 2D culture, where mitosis is easily quantifiable[58,59,137], interpreting HSLCI results in 3D organoid models is challenging. This is due to the difficulty in determining how many cells within a multicellular structure contribute to the phase shift at any given coordinate of a phase image.

The primary limiting factor of HSLCI data analysis is that HSLCI-acquired datasets, similarly to other time-resolved, high-content imaging assays of organoids[44], account for very large amounts of data storage space[66,174]. A typical experiment following our complete protocol can produce >10 TB of interferograms and >2 TB of downstream analysis files, substantially consisting of stacks of unwrapped phase images encoded in .mat files. As a result, full analysis of HSLCI-acquired organoid datasets using the listed hardware can take up to a week or more, although this duration can be decreased with additional computational power. Additionally, tracking results can be affected by inaccurate image segmentation, object tracking, or track classification, and the ML models in the analysis pipeline may need to be retrained for different organoid morphologies or biomass accumulation behaviors to appropriately account for organoid phenotypes that are different than those of the MCF-7 and BT-474 cell line–derived organoids used in the training datasets[44,182].

Overview of the Procedure

This protocol provides a step-by-step guide to growing plates of bioprinted organoids for high-throughput drug screening and performing high-throughput QPI and associated data analyses of output organoid-level biomass changes and drug response data. The protocol is divided into three main procedures (**Figure 3.1**) as follows:

1. Procedure 1 (Steps 1–71): Establishment and culturing of bioprinted organoids for downstream high throughput imaging and drug screening experiments. Our bioprinting protocol involves suspending cells in a Matrigel-based mixture and seeding onto the

bottom surface of each well of standard 96-well glass-bottom assay plates in well-aligned, flat “mini-square” constructs[174]. First, we 3D print masks out of cell culture–compatible Biomed Amber Resin (FormLabs) to enable selective modification of the glass surfaces of 96-well glass-bottom assay plates in a pattern that facilitates spreading of the extruded cell-laden Matrigel bioink. This step can be performed days or weeks prior to bioprinting. Then, before beginning the subsequent high throughput imaging and drug screening workflow, we verify that the bioprinting protocol generates full plates of cell-laden bioink constructs that assume the desired thin, flat, square-shaped geometry and are roughly centered within each well and aligned with the edges of a plate. Whole-well brightfield imaging and ATP release assays can be performed immediately following bioprinting to validate the 3D alignment of the user-inputted print instructions and to determine whether constructs are seeded with consistent volumes and cell numbers. Otherwise, after bioprinting and automated addition of organoid media, organoids grow over the course of three days, and we perform daily whole-well brightfield imaging.

2. Procedure 2 (Steps 1–43): Drug treatment of bioprinted organoids and HSLCI operation. With sufficient time remaining prior to treatment (three days after bioprinting to seed organoids), we prepare a drug treatment map for the bioprinted organoid plate of interest, and correspondingly prepare a plate containing drug- and vehicle-treated media. Three days after bioprinting to seed organoids, we perform automated addition of drug treatments using a liquid handler, and then as soon as possible after drug treatment, we perform automated, label-free, time-resolved QPI of organoids for three days using the HSLCI platform. HSLCI is a noninvasive technique that allows repeated, time-resolved imaging: in a typical experiment, interferograms are acquired from 1,000+ FOVs across a 96-well plate every 10 minutes for three days to obtain growth and drug response kinetics for thousands of individual organoids. When validation of HSLCI-acquired data with

conventional measurements of well-level viability results is desired, we perform a terminal ATP release assay at the conclusion of the HSLCI imaging experiment.

3. Procedure 3 (Steps 1–12): Data analysis of HSLCI results. First, we use our custom phase unwrapping script along with the manufacturer's software to convert interferograms collected by HSLCI to phase shift maps. Then, we run our custom data analysis pipeline, which includes image segmentation, organoid tracking, track classification, and single-organoid level analyses.

Experimental Design

The methods our protocol describes are of broad interest to researchers using 3D organoid models for high throughput screening, and are applicable well beyond the cancer field. We anticipate that these methods could be particularly useful for researchers in the field of precision cancer medicine who use PDTO models for functional imaging and drug sensitivity or response studies. Although our methods are uniquely powerful for FPM studies, we anticipate that they will provide valuable organoid-level results for researchers investigating the biology of disease, normal development, or physiologic responses to the local well environment.

Key timing parameters of our complete protocol, including of the drug treatment and imaging steps, are adjustable as desired, with the consideration that replenishment of organoid media is required every two to three days when bioprinted organoids are grown for longer than three days, and volumes of drug-treated media must be increased from the recommended 100 µL when organoids are subjected to drug treatments of longer than three days. Seeding parameters, including the concentration of cells in bioink and organoid media formulation, can be modified as desired according to the requirements of the specific organoid model. We used a single-endpoint ATP release assay to evaluate the effect of drug treatments on organoid growth at the end of the HSLCI imaging duration, in parallel with highly time-resolved HSLCI-acquired measurements of individual organoids' biomass accumulation behaviors, although this additional

assay is optional and other endpoint measurements of cell viability, metabolic activity, proliferation, or single-gene reporter activity can also be used for hit selection[27,44,183].

The main procedures of bioprinting, high-throughput QPI, and subsequent analysis of the acquired high-content imaging datasets (**Figure 3.1**) can each be substituted for an alternative method when desired. We chose to bioprint using Matrigel bioink because it can be used to create mechanically strong bioprinted constructs that promote complex, physiologically relevant cell behavior[136], and furthermore is generalizable in its ability to establish organoids from many human tissue sources and disease types[19,31]. An additional advantage of Matrigel is that it undergoes temperature-dependent physical crosslinking without the addition of an exogenous agent, avoiding the risk of chemical contamination of organoid culture[136]. When alternative bioinks are considered for growing organoid models of cancer, desirable features include bioprintability, stability *in vitro* in organoid culture medium, and support for cell adhesion, organoid growth, and mobility[136]. The crosslinking mechanism of the bioink must also not require the addition of external stimuli that may damage or otherwise affect the embedded cells during seeding[136]. We chose to use extrusion bioprinting to seed cells in Matrigel because of its relative speed and scalability[136,184]. Other labs have developed methods to bioprint cells in Matrigel using other commercially available or custom-built bioprinters; other bioprinting modalities including laser-based bioprinting or droplet-based bioprinting are possible for printing cells in Matrigel bioink when they do not result in excessive cell death[136,184]. Commercially available bioprinters have rapidly improved in capability in the past decade[94],and we anticipate that further improvements in temperature control and print resolution will make bioprinting processes even more robust.

As our bioprinting protocol solves or improves many challenges of high-throughput and high-content organoid imaging by establishing cultures of 3D organoid models in thin, flat ECM constructs, it could be applicable for other high-throughput and high-content organoid imaging modalities. Specifically, although we used a QWLSI wavefront sensing camera, other forms of

interference microscopy could in theory be similarly adapted into a high-throughput QPI platform for high-throughput growth and drug response profiling[45]. To achieve the desired combination of imaging throughput and time resolution for high-throughput drug screening, the selected QPI modality must be compatible with automated imaging using a linear plate scanning device. QPI methods that use single image acquisition, such as QWLSI, are strictly necessary because those that require multiple exposures to reconstruct a single phase image, such as phase-shifting interferometry, differential phase contrast microscopy, and Fourier ptychography, have comparatively much lower potential temporal resolution[45]. Single image acquisition is also advantageous over dual-path QPI methods because reconstruction of phase shift maps are less sensitive to vibration[45]. Finally, autofocusing mechanisms other than the one shown in the HSLCI optical assembly (**Figure 3.2**) are possible to configure and have been demonstrated in other QPI systems[45].

Many alternative methods have been developed for analyzing large volumes of high-content imaging data[77,182],and individual components of the included HSLCI data analysis pipeline code can be modified as desired. The U-Net CNN model that we used for segmenting high-throughput, time-series QPI datasets was trained using 50 randomly selected phase shift images from each of MCF-7 and BT-474 cell line–derived organoid datasets shown in Tebon et al 2023[174], because these organoids were observed to have lobular morphologies representative of a substantial fraction of organoid models of breast cancer[36]. The-segmentation algorithm can be re-trained using different or additional labeled phase shift images, or with different training parameters, when necessitated by suboptimal performance of the U-Net segmentation algorithm[182] (see Troubleshooting). We assembled data from discrete segmented organoids into time-coherent tracks using a linking cost minimization algorithm, one of three available algorithms included in the TrackMate program[176,177]. We tested each of the algorithms available and determined that the Sparse LAP tracker was the most effective of the options for our datasets

given that the organoids did not exhibit linear movement and often changed size, which rendered the Kalman filter–based and the nearest neighbor–based algorithms less effective. We used the tracking parameters shown in **Table S3.1**, although user customization of tracking parameters could be appropriate for datasets with different organoid morphologies and behaviors, and other effective algorithms are available for time-series particle tracking[185]. For exclusion of unreliable biomass tracks corresponding to HSLCI images of out of focus organoids, we used an XGBoost-based classifier because of its sensitivity and accuracy in classifying our HSLCI-acquired time series biomass data[124]. With the parameters listed in **Table S3.2**, we trained this XGBoost-based classifier using a randomly selected subset of time series organoid biomass data from vehicle-treated MCF-7 and BT-474 cell line–derived organoids shown in Tebon et al 2023[174], manually labeled to exclude organoids moving into and out of focus, frequently overlapping and/or separating from neighboring organoids, or overlapping with debris. Analysis of time-series biomass datasets from organoid models with drastically different phenotypes or temporally specific patterns of biomass changes may necessitate the re-training of XGBoost with different training datasets or parameters[182] (see Troubleshooting).

Materials

Biological materials

- MCF-7 cells (ATCC, cat. no. HTB-22)
- BT-474 cells (ATCC, cat. no. HTB-20)

  Critical: The protocol reported here was developed and optimized using MCF-7 and BT-474 cells. When establishing this protocol using cells from a different source, we recommend validating the bioprinted 3D models or organoids by performing imaging, histochemical, and molecular comparisons with their manually seeded equivalents.

Reagents

- MammoCult human medium kit (StemCell Technologies, cat. no. 05620)
- MammoCult basal medium (StemCell Technologies, cat. no. 05621)
- MammoCult human proliferation supplement (StemCell Technologies, cat. no. 05622)
- Hydrocortisone stock solution, 96 µg/mL (StemCell Technologies, cat. no. 07925)
- Heparin solution, 0.2% (StemCell Technologies, cat. no. 07980)
- Matrigel basement membrane matrix (Corning, cat. no. 354234)
- RPMI 1640 medium, L-glutamine, 25 mM HEPES (Gibco, cat. no. 22400-089)
- Fetal bovine serum (FBS), qualified, heat inactivated (Gibco, cat. no. 16140-071)
- Antibiotic-antimycotic, 100× (Gibco, cat. no. 15240-062)
- Staurosporine (Selleck Chemicals, cat. no. S1421)
- Lapatinib (Selleck Chemicals, cat. no. S1028)
- Neratinib (Selleck Chemicals, cat. no. S2150)
- Dimethyl sulfoxide (Fisher Scientific, cat. no. BP231-100)
- BioMed Amber Resin (Form 3), 1L (FormLabs, cat. no. RS-F2-BMAM-01)
- Isopropyl alcohol, 99% min. (MilliporeSigma, cat. no. PX18304)
- Dulbecco's phosphate buffered saline (DPBS), no calcium, no magnesium (Gibco, cat. no. 14190-144)
- Trypsin-EDTA, 0.05%, phenol red (Gibco, cat. no. 25300-054)
- CellTiter-Glo 3D cell viability assay (Promega, cat. no. G9683)
- ViaStain AOPI staining solution (Nexcelom, cat. no. CS2-0106-5mL)
- Dispase (Life Technologies, cat. no. 17105-041)

Equipment

High-speed live cell interferometry (HSLCI) system foundation

- Steri-Cult CO_2 incubator (Thermo Scientific, cat. no. 3310)
- UltraLight Series II breadboard, 24" x 18" x 2.2", 1/4"-20 taps (ThorLabs, cat. no. PBG12118)
- 6" x 12" x 1/2" aluminum breadboard, 1/4"-20 double-density taps (ThorLabs, cat. no. MB612)
- Large right-angle mounting plate, 1/4"-20 compatible (ThorLabs, cat. no. AP90L)
- 100 mm motorized linear translation stage, stepper motor, 1/4"-20 taps (ThorLabs, cat. no. NRT100)
- 50 mm (1.97") TravelMax translation stage, 1/4"-20 taps (ThorLabs, cat. no. LNR50S)
- Right-angle bracket for LNR50 TravelMax stages, imperial threads (ThorLabs, cat. no. LNR50P2)
- Vertical mounting bracket for LNR25 stage (ThorLabs, cat. no. LNR25P2)
- Adapter plate for Ø1.5" post mounting clamp, 2.50" x 2.50" (ThorLabs, cat. no. C1520)
- Custom plate holder

HSLCI system hardware components for optical cage assembly, general

- SM1-threaded 30 mm cage plate, 0.35" thick, 2 retaining rings, 8-32 tap (ThorLabs, cat. no. CP02)
- Cage assembly rod, 1/4" long, Ø6 mm (ThorLabs, cat. no. ER025)
- Cage assembly rod, 1/2" long, Ø6 mm (ThorLabs, cat. no. ER05)
- Cage assembly rod, 1" long, Ø6 mm (ThorLabs, cat. no. ER1)
- Cage assembly rod, 1.5" long, Ø6 mm (ThorLabs, cat. no. ER1.5)
- Cage assembly rod, 3" long, Ø6 mm (ThorLabs, cat. no. ER3)
- Cage assembly rod, 4" long, Ø6 mm (ThorLabs, cat. no. ER4)
- Cage assembly rod, 6" long, Ø6 mm (ThorLabs, cat. no. ER6)
- Ø1/2" post holder, spring-loaded hex-locking thumbscrew, L = 3" (ThorLabs, cat. no. PH3)
- Ø1/2" optical post, SS, 8-32 setscrew, 1/4"-20 tap, L = 1" (ThorLabs, cat. no. TR1)

- Ø1/2" optical post, SS, 8-32 setscrew, 1/4"-20 tap, L = 4" (ThorLabs, cat. no. TR4)
- Mounting base, 2" x 3" x 3/8" (ThorLabs, cat. no. BA2)
- SM1-threaded IR alignment disk (790 - 840 nm, 870 - 1070 nm, 1500 - 1590 nm) (ThorLabs, cat. no. VRC4SM1)

HSLCI system hardware components for optical cage assembly, phase imaging light path

- SID4 Bio quadriwave lateral shearing interferometry camera (Phasics, cat. no. SID4-533)
- Standard power supply 12.6 V DC, 2 A, with one strobe and one trigger, 1.5 m (Imperx, cat. no. PS12V04 or PS12V04A)
- 30 mm to 60 mm cage plate adapter, 8-32 tap (ThorLabs, cat. no. LCP02)
- 60 mm cage plate, SM2 threads, enhanced clamping, 0.5" thick, 8-32 tap, one SM2RR retaining ring (ThorLabs, cat. no. LCP08)
- Adapter with external C-mount threads and internal SM1 threads, 4.4 mm spacer (ThorLabs, cat. no. SM1A9)
- SM1 (1.035"-40) coupler, external threads, 0.5" long, two locking rings (ThorLabs, cat. no. SM1T2)
- Adapter with external SM2 threads and internal M38 x 0.5 threads (ThorLabs, cat. no. SM2A20)
- Tube lens, f = 200 mm, external M38 x 0.5 threads (ThorLabs, cat. no. ITL200)
- Ø2" broadband dielectric mirror, 400 - 750 nm (ThorLabs, cat. no. BB2-E02)
- Right-angle kinematic mirror mount with tapped cage rod holes, 60 mm cage system and SM2 compatible, 8-32 and 1/4"-20 mounting holes (ThorLabs, cat. no. KCB2)
- Cage plate mounting base for 60 mm cage plates, imperial (ThorLabs, cat. no. LCPB1)
- Matte black aluminum foil, 1' x 50' (305 mm x 15.2 m) x .002" (50 µm) thick (ThorLabs, cat. no. BKF12)

- CFI Plan Fluor 40X objective, NA 0.75 (Nikon)
- Nano-F100S piezo nanopositioner (Mad City Labs)
- Kinematic fluorescence filter cube for Ø25 mm fluorescence filters, 30 mm cage compatible, right-turning, 1/4"-20 tapped holes (ThorLabs, cat. no. DFM1)
- 25 mm x 36 mm shortpass dichroic mirror, 805 nm cutoff (ThorLabs, cat. no. DMSP805R)
- Ø1" near-IR hot mirror, AOI: 0°, 1 mm thick (ThorLabs, cat. no. FM01)
- Adapter with external SM1 threads and internal M25 x 0.75 threads (ThorLabs, cat. no. SM1A12)
- SM1 lens tube, 0.50" thread depth, one retaining ring included (ThorLabs, cat. no. SM1L05)
- Ø1000 µm, 0.39 NA, SMA-SMA fiber patch cable, low OH, 1 m long (ThorLabs, cat. no. M35L01)
- 543 nm, f = 7.86 mm, NA = 0.51 SMA905 fiber collimation package (ThorLabs, cat. no. F240SMA-A)
- SM1-threaded adapter for Ø12 mm, ⩾0.35" (8.9 mm) long cylindrical components (ThorLabs, cat. no. AD12F)
- Mounted N-BK7 bi-convex lens, Ø1", f = 35.0 mm, ARC: 350 - 700 nm (ThorLabs, cat. no. LB1811-A-ML)
- Ø1.5" mounting post, 1/4"-20 taps, L = 14" (ThorLabs, cat. no. P14)
- Ø1.5" post mounting clamp, 2.50" x 2.50" (ThorLabs, cat. no. C1511)

HSLCI system hardware components for optical cage assembly, infrared laser light path in autofocusing module

- Collimated laser diode module, 980 nm, 4.5 mW, elliptical beam, Ø11 mm housing (ThorLabs, cat. no. CPS980)

- Laser safety glasses, light green lenses, 59% visible light transmission, sport style (ThorLabs, cat. no. LG1B)

  Caution: Always put on laser safety glasses before turning on the infrared (IR) laser. Be extremely careful to avoid eye damage; IR laser does not induce a blink response! Must not view the laser beam directly or indirectly through mirrors or optics.

  Caution: Safest practice is to always wear laser safety goggles when opening the HSLCI incubator for any reason to avoid eye damage from the IR laser, which does not induce a blink response!
- SM1-threaded adapter for Ø11 mm, ⩾0.35" (8.9 mm) long cylindrical components (ThorLabs, cat. no. AD11F)
- SM1 graduated ring-actuated zero aperture iris diaphragm, Ø12.0 mm max aperture (ThorLabs, cat. no. SM1D12CZ)
- Adapter with external SM05 threads and internal SM1 threads (ThorLabs, cat. no. SM1A1)
- 30 mm cage system, XY translating lens mount for Ø1" optics (ThorLabs, cat. no. CXY1)
- Cage plate mounting base for 30 mm cage plates, imperial (ThorLabs, cat. no. CPB1)
- 1" translation stage with standard micrometer, 1/4"-20 taps (ThorLabs, cat. no. PT1)
- Right-angle kinematic mirror mount with smooth cage rod bores, 30 mm cage system and SM1 compatible, 8-32 and 1/4"-20 mounting holes (ThorLabs, cat. no. KCB1C)
- Ø1" protected silver mirror (ThorLabs, cat. no. PF10-03-P01)
- Ø1" zero-order quarter-wave plate, SM1-threaded mount, 980 nm (ThorLabs, cat. no. WPQ10M-980)
- Cage rotation mount for Ø1" optics, SM1 threaded, 8-32 tap (ThorLabs, cat. no. CRM1)
- 30 mm cage-cube-mounted polarizing beamsplitter cube, 980 nm, 8-32 tap (ThorLabs, cat. no. CCM1-PBS25-980)

- Ø1" N-BK7 plano-convex lens, SM1-threaded mount, f = 500 mm, ARC: 650-1050 nm (ThorLabs, cat. no. LA1908-B-ML)
- Ø1" N-BK7 plano-convex lens, SM1-threaded mount, f = 125 mm, ARC: 650-1050 nm (ThorLabs, cat. no. LA1986-B-ML)
- 30 mm cage cube with dichroic filter mount (ThorLabs, cat. no. CM1-DCH)
- 25 x 36 mm 10:90 (R:T) UVFS plate beamsplitter, coating: 700 - 1100 nm, t = 1 mm (ThorLabs, cat. no. BSN11R)
- Quadrant detector sensor head, 400 to 1050 nm (ThorLabs, cat. no. PDQ80A)
- USB 2.0 CMOS Camera, 1280 x 1024, monochrome sensor (ThorLabs, cat. no. DCC1545-M or DCC1545M-GL)

HSLCI electronic components outside of incubator

- 660 nm, 13.0 mW (min) fiber-coupled LED, 1000 mA, SMA (ThorLabs, cat. no. M660F1)
- ±12 VDC regulated linear power supply, 6 W, 100/120/230 VAC (ThorLabs, cat. no. LDS12B)
- 4-channel LED driver, 1 modulation input, 1 A, 5 V (ThorLabs, cat. no. DC4100)
- Single LED connector hub for DC4100 (ThorLabs, cat. no. DC4100 HUB)
- Three-channel benchtop stepper motor controller (ThorLabs, cat. no. BSC203)
- Nano-Drive C single-axis controller (Mad City Labs)
- 5 VDC regulated power supply, 2.5 mm Phono Plug, 120 VAC (ThorLabs, cat. no. LDS5)
- Tektronix TDS 2002C oscilloscope (Tektronix, cat. no. TDS 2002C)
- Feedback controller box with a custom-built circuit board that includes an Arduino Nano microcontroller and a Teensy 3.6 microcontroller
- Gigabit ethernet cable
- BNC cables
- 15-pin D-SUB connectors

- USB cables

Imaging computer

- Dell Precision Tower 5810 with an Intel Core i7-8700 CPU and Windows 10 Enterprise Version 22H2, OS build 19045.4529

Data analysis computer

- Custom-built multi-core processing computer with an Intel Core i7-5930K CPU, Windows 10 Enterprise Version 22H2, OS build 19045.5011 and virtual machine platform support

Other equipment

- Biological safety cabinet
- CO_2 incubator, set at 37°C and 5% CO_2
- Inverted tissue culture microscope
- Vortex
- Centrifuge
- Rubber bands
- Straight razors
- Disposable compressed gas duster
- Pipettes (p1000, p200, p20, p10, p2)
- 12-channel pipettes (p300, p100)
- Serological pipette controller
- 2 mL serological pipets, sterile (Greiner Bio-One, cat. no. 710180)
- 5 mL serological pipets, sterile (Greiner Bio-One, cat. no. 606180)
- 10 mL serological pipets, sterile (Greiner Bio-One, cat. no. 607180)
- 25 mL serological pipets, sterile (Greiner Bio-One, cat. no. 760180)

- 50 mL serological pipets, sterile (Greiner Bio-One, cat. no. 768180)
- Aspirating pipettes, 2 mL, sterile (Greiner Bio-One, cat. no. 710183)
- uTIP non-filter pipette tips, 10µL, sterile (Biotix, cat. no. 63300048)
- uTIP filter pipette tips, 2µL, sterile (Biotix, cat. no. 63300153)
- uTIP filter pipette tips, 10µL, sterile (Biotix, cat. no. 63300154)
- uTIP filter pipette tips, 20µL, sterile (Biotix, cat. no. 63300042)
- uTIP non-filter pipette tips, 200µL, sterile (Biotix, cat. no. 63300050)
- uTIP non-filter pipette tips, 300µL, sterile (Biotix, cat. no. 63300052)
- uTIP filter pipette tips, 300µL, sterile (Biotix, cat. no. 63300045)
- uTIP filter pipette tips, 1250µL, sterile (Biotix, cat. no. 63300047)
- Disposable reagent reservoirs, sterile (Corning, cat. no. 4870)
- 1.5 mL microcentrifuge tubes, sterile (Eppendorf, cat. no. 022363212)
- 2.0 mL microcentrifuge tubes, sterile (Eppendorf, cat. no. 022363344)
- 15 mL conical centrifuge tubes (Falcon, cat. no. 352096)
- 50 mL conical centrifuge tubes (Falcon, cat. no. 352098)
- Corning vacuum filter/storage systems, 0.22 µm pore size, 500 mL, sterile (VWR, cat. no. 28199-788)
- Steriflip disposable vacuum filter units, 0.22 µm pore size, 50 mL, sterile (MilliporeSigma, cat. no. SCGP00525)
- 100 µm cell strainer (VWR, cat. no. 10054-458)
- 70 µm cell strainer (VWR, cat. no. 10054-456)
- 40 µm cell strainer (VWR, cat. no. 10054-462)
- 100 mm cell culture dish (VWR, cat. no. 10062-880)
- Form 3B bioprinter (FormLabs)
- Form Cure UV curing oven (FormLabs, cat. no. FH-CU-01)

- 96-well flat clear bottom black or white polystyrene TC-treated microplates, individually wrapped, with lid, sterile (Corning, cat. no. 3603 or 3610)
- 96-well glass bottom plate with high performance #1.5 cover glass (Cellvis, cat. no. P96-1.5H-N)
- Bio X 3D bioprinter (CELLINK)
- Temperature-controlled printhead (CELLINK, cat. no. CL-PH-TCPH)
- High-precision blunt needles 25G, 12.7 mm (0.50 inch), sterile (CELLINK, cat. no. NZ6250505001)
- Empty cartridges with end and tip caps, 3 mL, sterile (CELLINK, cat. no. CSC010311101)
- Female/female Luer Lock adapters (CELLINK, cat. no. OH000000050)
- Disposable syringes with Luer Lock tips, 3 mL, sterile (BD, cat. no. 309657)
- Cellometer Auto 2000 cell viability counter (Nexcelom, cat. no. CMT-A2K)
- Cellometer SD100 cell counting slides (Nexcelom, cat. no. CHT4-SD100-002)
- Enviro-Genie benchtop refrigerator incubator (Scientific Industries)
- PE-25 plasma cleaner (Plasma Etch)
- MASTERBLOCK 96 Well Polypropylene 0.5mL V-Bottom deep well plates, sterile (Greiner Bio-One, cat. no. 786261)
- epMotion 96 liquid handler (Eppendorf, cat. no. 5069000004)
- epT.I.P.S. Motion as Reload System, 50µL tips, with filter, PCR clean and sterile (Eppendorf, cat. no. 0030014529)
- epT.I.P.S. Motion as Reload System, 300µL tips, with filter, PCR clean and sterile (Eppendorf, cat. no. 0030014537)
- Celigo S image cytometer (Nexcelom, cat. no. 200-BFFL-S)
- LSE digital microplate shaker, 120V (Corning, cat. no. 6780-4)
- MicroAmp optical adhesive film (Applied Biosystems, cat. no. 4311971)

- SpectraMax iD3 multi-mode microplate reader (Molecular Devices)
- Parafilm M laboratory wrapping film (Bemis, cat. no. PM996)

Software

Software required for Procedure 1: Establishment and culturing of bioprinted organoids for downstream high-throughput imaging and drug screening experiments

- (Optional) Fusion (2.0.18460, Autodesk) – software for computer-aided design (CAD) of well masks.
- (Optional) Inventor (Autodesk) – software for computer-aided design (CAD) of well masks.
- Preform (3.41.0.427, FormLabs) – software for operating FormLabs 3D printer.
- Celigo S Software (Nexcelom) – software for using Celigo S whole-well plate imager.
- (Optional) DNA Studio (v4, CELLINK) – software for generating and visualizing bioprinter instruction files (G-code) for the Bio X bioprinter.

Software required for HSLCI operation (Procedures 2.2–2.3)

- SID4Bio Software (v2.4.2.93, Phasics) – required for the imaging computer to interface with the Phasics QWLSI camera and unwrap interferograms.
- SID4 SDK (CPU version, v7.4.1, Phasics) – required for computer to interface with the Phasics QWLSI camera and unwrap interferograms (although unwrapping is performed on a separate analysis computer using the more efficient GPU version of SID4 SDK).
- eBUS SDK (v3.1.7, Phasics) – required drivers for the Phasics QWLSI camera and associated software.
- DC4100 Series 4 channel LED Driver (version 2.2.44.95, ThorLabs) – required drivers for the DC4100 LED controller box.

- Arduino IDE (2.1.1) – open-source integrated development environment (IDE) for Arduino microcontrollers.
- Teensyduino (version 1.59) – add-on that allows Arduino IDE to work with the Teensy 3.6 microcontroller.
- ThorLabs Advanced Positioning Technology (APT) software (version 3.21.3) – required for the imaging computer to interface with the x-, y-, and z- translation stages.
- ThorCam (version 3.2.0.0, ThorLabs) – used on the imaging computer for visualizing the IR laser signal for the autofocusing system.
- MATLAB R2018b (MathWorks) – required on the imaging computer for interfacing with the HSLCI system's electronic components.
    - MATLAB (Version 9.5, R2018b)
    - Simulink (Version 9.2, R2018b)
    - Curve Fitting Toolbox (Version 3.5.8, R2018b)
    - Image Acquisition Toolbox (Version 5.5, R2018b)
    - Image Processing Toolbox (Version 10.3, R2018b)
    - Instrument Control Toolbox (Version 3.14, R2018b)
    - Parallel Computing Toolbox (Version 6.13, R2018b)

Software required for Procedure 3.1: Unwrapping interferograms into phase shift images

- SID4Bio Software (v.2.4.2.93, Phasics) – required for the data analysis computer to interface with the Phasics QWLSI camera and unwrap interferograms (although imaging is performed on a separate imaging computer).
- SID4 SDK (GPU version, v7.4.1, Phasics) – required for computer to unwrap interferograms; enables more efficient unwrapping using a multi-core processor and the parallel computing toolbox in MATLAB.

- eBUS SDK (v3.1.7, Phasics) – required drivers for the Phasics QWLSI camera and associated software.
- MATLAB R2020a (MathWorks) – required on the data analysis computer for interfacing with Phasics software and unwrapping interferograms.
    - MATLAB (Version 9.8, R2020a)
    - Simulink (Version 10.1, R2020a)
    - Bioinformatics Toolbox (Version 4.14, R2020a)
    - Control System Toolbox (Version 10.8, R2020a)
    - Curve Fitting Toolbox (Version 3.5.11, R2020a)
    - DSP System Toolbox (Version 9.10, R2020a)
    - Data Acquisition Toolbox (Version 4.1, R2020a)
    - Image Acquisition Toolbox (Version 6.2, R2020a)
    - Image Processing Toolbox (Version 11.1, R2020a)
    - Instrument Control Toolbox (Version 4.2, R2020a)
    - Optimization Toolbox (Version 8.5, R2020a)
    - Parallel Computing Toolbox (Version 7.2, R2020a)
    - Signal Processing Toolbox (Version 8.4, R2020a)
    - Statistics and Machine Learning Toolbox (Version 11.7, R2020a)
    - Symbolic Math Toolbox (Version 8.5, R2020a)

Software required for Procedure 3.2: Analysis pipeline code

- (Highly recommended) git (2.47.0) – for version control on Windows operating system.
- (Highly recommended) git (2.34.1) – for version control when running Linux shells on a Windows computer.
- (Highly recommended) GitHub Desktop (3.4.2) – for version control.

- VSCodium (1.72.2.22286) – open-source IDE used for viewing, editing, debugging, and running code.
- Python (3.10.5) – required for running and debugging Python code without calling nextflow.
- R (4.2.1) – required for running and debugging R code without calling nextflow.
- RStudio (2022.07.1+554) – required for running and debugging R code without calling nextflow.
- ImageJ (1.43u) – required for running TrackMate.
- TrackMate (version 7.6.1) – particle-tracking software called by analysis pipeline code.
- PowerShell 7.4.5 – open-source command line shell for Windows, Mac OS, and Linux.

  Tabby (1.0.205) – open-source cross-platform terminal app. Optional.
- Windows Subsystem for Linux (2.0.14.0) – required to run the open-source Linux OS in a virtual machine (VM) environment on Windows.
- Ubuntu (release 22.04) – Linux distribution for WSL, run in a VM environment on Windows.
- OpenJDK (Eclipse Temurin build, v21.0.2) – open-source implementation of Java Platform, Standard Edition (Java) SE. Java is required to run Nextflow.
- Docker Desktop (4.27.1) – enables users to run code from the equivalent virtual environment (Docker container) on any VM–enabled computer.
- Nextflow (v24.04.4 build 5917) – workflow orchestrator that allows us to run pipelines of data analysis scripts in sequence, and theoretically in parallel.

Equipment setup

Box 1: High-speed live cell interferometry (HSLCI) system setup

The hardware and software components of our HSLCI system can all be programmed to interface with MATLAB (MathWorks). Imaging scripts are run on the imaging PC using MATLAB. The main imaging script is initiated from an interactive graphic user interface (GUI) that allows the user to operate the translation stages, take reference images, test feedback control of the autofocusing system prior to running a long-term imaging experiment, and adjust the movement speeds and coordinates of the translation stages for each experiment, as desired (**Figure 3.4**). The imaging script commands the translation stages to move to the user-designated starting coordinates for repeated scans down columns of glass-bottom plates and repeated image captures at the same FOVs for a user-designated number of imaging loops (**Figure 3.3G**). The purpose of the custom-built feedback control box is to trigger repeated image captures using the QWLSI camera and sample illumination through the LED controller simultaneously, with movements of the translation stages, while enabling high-resolution and high-speed feedback control of the autofocusing system using both the piezo nanopositioner coupled to the microscope objective and the translation stage for z-axis movement. We custom built the feedback control box to be independent of the imaging computer's computational resources while enabling precise triggering and focusing by using two microcontrollers: an Arduino Nano and a Teensy 3.6. The Arduino Nano is used as a pulse generator for externally triggering the illumination LED at regular intervals during image capture. The Teensy 3.6 is used to interface with the imaging computer and to perform feedback loop calculations for autofocusing the objective while running continuous, long-term imaging scripts. The QWLSI camera captures images with each trigger signal from the pulse generator while sending a strobe signal to the illumination LED controller such that illumination is synchronized with stage movement and exposure time. The autofocus system functions by applying closed-loop feedback control to the piezo nanopositioner to adjust the distance between the objective and the plate bottom being imaged such that the plate remains in focus during repeated cycles of scanning and imaging (**Figure 3.2C**, **Figure 3.3G**). The input signal of the feedback system for automatically focusing the objective is achieved using a quadrant photodiode detector (QPD). An IR laser is sent from a parallel optical track into the optical path of the microscope and reflects off the bottom surface of the glass-bottom plate being imaged and back into the QPD sensor. (**Figure 3.2A–C**) The QPD converts the intensity and position of this reflected IR laser signal into a voltage, which is sensitive to the distance between the objective and the bottom surface of the plate being imaged. The output signal of the feedback control box is a voltage output to the piezo nanopositioner, which rapidly and precisely adjusts the height of the microscope objective. While the imaging script is running, the feedback control box can also jog the z-translation stage up and down to compensate for the approximately 100 μm spatial translation limit of the piezo. Ten percent of this IR laser is also diverted into the ThorLabs camera using a beamsplitter, to enable visualization of the IR laser image on the imaging computer for plate-specific adjustments at the start of each HSLCI imaging experiment.

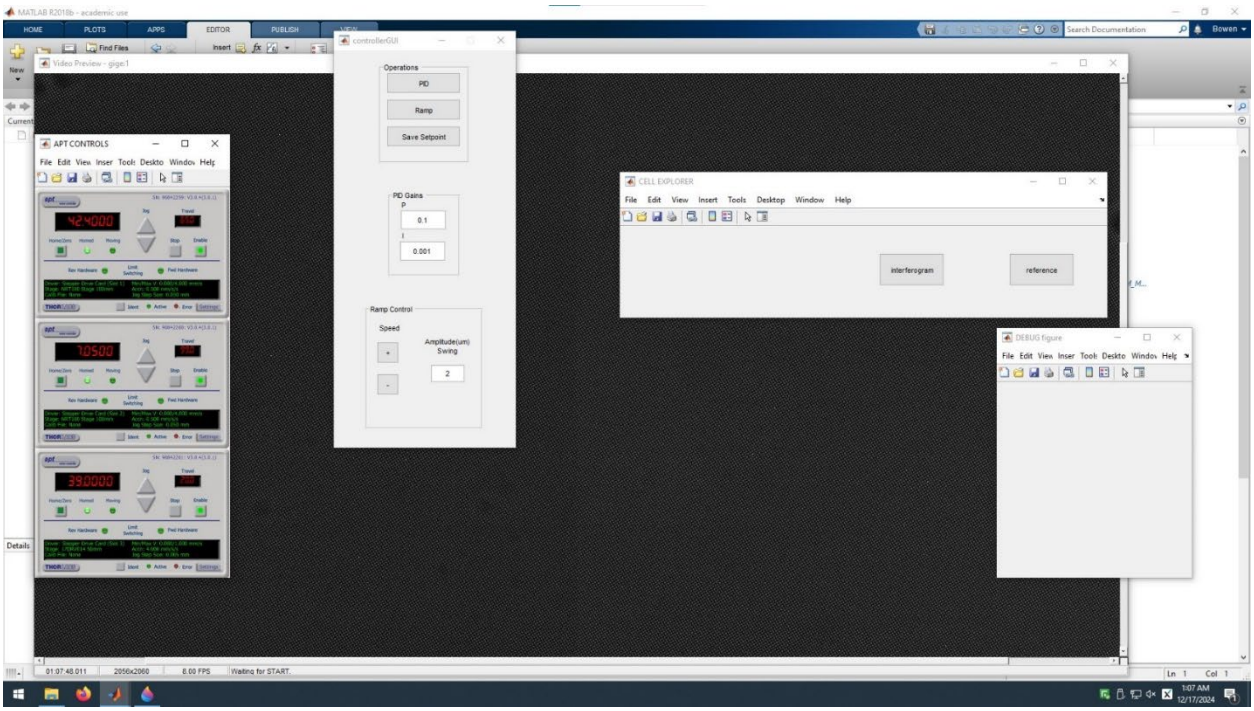

Figure 3.4: Screenshot of the user interface for operating HSLCI hardware components and running imaging experiments. All HSLCI hardware and software are run from the imaging computer through an interactive graphic user interface (GUI). The “APT CONTROLS” window can be used to move the plate holder containing the organoid plate of interest such that the desired imaging field of view (FOV) is visible in the “Video Preview” window, which displays the QWLSI camera signal in real time. The “controllerGUI” window is used for testing the HSLCI platform’s feedback control system, while the “CELL EXPLORER” window is primarily used for taking reference images.

1. Construct the previously described microscopy setup within an optical cage assembly inside the incubator using the above materials and following **Figure 3.2A** and **Figure 3.2B**.

    Caution: Always put on laser safety glasses before turning on the IR laser. Be extremely careful to avoid eye damage; IR laser does not induce a blink response! Individuals must not view the laser beam directly or indirectly through mirrors or optics.

2. Make the following connections between the interfacing components contained inside the HSLCI incubator and the electronic components outside the HSLCI incubator:

    a. The QWLSI camera is connected to the imaging computer with a Gigabit Ethernet cable.

b. The QWLSI camera is powered by an Imperx PS12V04/PS12V04A power supply unit, which contains an extra BNC connection that allows for external camera triggering.

c. Through this power supply unit, the QWLSI camera is connected to the feedback control box with a BNC cable.

Critical: This cable enables the camera to be triggered using an external signal, in our case a microcontroller in the feedback control box.

d. Through this power supply unit, the QWLSI camera is also connected to the illumination LED controller units with a BNC cable.

Critical: This cable enables the strobe function of the illumination LED during imaging.

e. The illumination LED controller units are connected to the imaging computer with a USB cable.

f. The illumination LED controller units are also connected to the illumination LED fiber optics cable which leads into the incubator directly above the objective.

g. Each of three translation stages is connected to the stage controller, a three-channel stepper motor controller, using 15-pin D-SUB connectors from the translation stage to the corresponding port in the stage controller.

h. The stage controller is connected to the imaging computer with a USB cable.

i. The y-axis and z-axis ports of the stage controller are also connected to the feedback control box using 15-pin D-SUB connectors.

j. The piezo in the objective-piezo stack is connected to the piezo controller with a BNC cable.

k. The piezo controller is connected to the feedback control box with a BNC cable.

Critical: This connection carries the output voltage to the piezo nanopositioner.

l. The QPD is also connected to the feedback control box with a BNC cable.

Critical: This connection carries the input voltage corresponding to the signal of the IR laser reflected from the bottom surface of the glass-bottom plate well undergoing imaging on the HSLCI platform.

m. The oscilloscope is connected to the feedback control box with two BNC cables.

Critical: These connections enable real-time monitoring of the above output and input voltage signals in the autofocus system.

n. The feedback control box is connected to the imaging computer with a USB cable.

o. The ThorLabs camera is connected to the imaging computer with a USB cable.

3. Install all listed software components on the imaging computer.

4. Upload code for feedback control of the autofocus system into the Teensy microcontroller, and code for synchronized triggers of camera captures, LED illumination, and plate holder movements into the Arduino Nano microcontroller in the feedback control box.

Critical: Modifications to these scripts, including changes to the imaging frame rate and plate scanning movement parameters, are rarely necessary and require numerous additional modifications to the subsequent analysis workflow.

5. At least one day prior to drug treatment and HSLCI imaging (Procedure 2), which corresponds to two days after bioprinting to establish an organoid plate for this purpose (Procedures 1.1–1.3), turn on the HSLCI incubator and its CO_2 connection and all HSLCI hardware components except the IR laser power supply.

Critical: Because the closed-loop feedback response of the autofocus system is sensitive to temperature, the HSLCI incubator must be turned on sufficiently far in advance of each imaging experiment to allow for adequate time for all electronic components within the HSLCI incubator to temperature equilibrate.

6. Prior to drug treatment and HSLCI imaging (Procedure 2), home the x-, y-, and z- translation stages using the installed APT User software (ThorLabs).

Critical step: This step must be performed after each time the stage controller is powered on to ensure that the plate holder movements in the subsequent experiments are accurate.

Critical: Make sure the motors do not run the plate holder into a stationary object when homing the stages. Homing the plate holder into a stationary object could either knock over the objective or strip the motors' screws while moving the plate holder into something immovable. Homing the motors cannot be stopped through the ThorLabs APT software user interface (UI) and can only be done in an emergency by turning off the stage controller.

7. On a separate computer dedicated to the HSLCI data analysis workflow (Procedure 3), install all listed software components that are required for phase unwrapping HSLCI acquired interferograms (Procedure 3.1).

Critical: Unwrapping images acquired using the Phasics QWLSI camera is dependent on the manufacturer's digital rights management (DRM).

8. On the data analysis computer, install all listed software components that are required for running the multi-step HSLCI data analysis pipeline (Procedure 3.2) and set up a Linux distribution in a virtual machine environment.

Critical: Hardware virtualization must be enabled in the Unified Extensible Firmware Interface (UEFI) or Basic Input/Output System (BIOS) of the data analysis computer to enable it to emulate the Linux operating system.

Reagent setup

2+ days before Procedure 1: Printing masks for patterned oxygen plasma treatment

1. Plug a cartridge of BioMed Amber Resin (FormLabs) into the Form 3B printer (FormLabs) and open the vent cap at the top of the cartridge. BioMed Amber Resin was chosen as the ink for printing well masks because it is non-toxic to cells.

Critical: The build platform is the print substrate for the Form 3B bioprinter and it is important to ensure that it is clean before and after each print job.

Critical: Do not mix equipment used for BioMed Amber Resin with equipment used for other 3D printing inks incompatible with cell culture.

Caution: Uncured BioMed Amber Resin is hazardous and should be disposed of in accordance with all regulations.

2. (Optional) Generate a computer-aided design (CAD) file for the desired well mask model, and then export this file as a .stl file, unless a file is already available.

3. Connect the bioprinter to a computer and open Preform software (FormLabs).

4. Input and save the desired print settings. Ensure that the material selected is BioMed Amber Resin and layer thickness is 0.100 mm.

5. Using the Preform software's UI, lay out individual well mask constructs to be 3D printed such that they are not overlapping with one another, and such that the surfaces of the 96-well plate inserts (**Figure 3.3A–B**) are oriented away from the build platform. Save the print layout, send the print job to the bioprinter, and run the print.

Critical: When a BioMed Amber Resin construct is 3D printed using the Form 3B bioprinter, smaller surface areas that are in contact with the build platform are prone to warping when being removed from the build platform in the following step.

6. At the conclusion of the print, remove the build platform from the bioprinter and scrape off the uncured resin constructs using a straight razor.

7. Wash the resin constructs in a bath of 99% isopropyl alcohol (IPA) for 10–15 minutes. Rotate the constructs so that air bubbles are released.

Critical: Do not leave constructs in IPA for more than 30 minutes or they will swell.

8. Clean the constructs of residual particles or uncured resin, especially the interior faces of each square-shaped well mask, with a stream of compressed air.

9. Wash the resin constructs in a second bath of 99% IPA for 10–15 minutes. Rotate the constructs so that air bubbles are released.

Critical: Do not leave constructs in IPA for more than 30 minutes or they will swell.

10. Allow the constructs to air dry for at least 30 minutes to remove excess IPA.

11. Repeat step 8 and then allow the constructs to air dry again for at least 5–10 minutes to ensure they are entirely dry.

12. Arrange the constructs in an ultraviolet (UV) curing oven so that they are not touching each other.

13. Crosslink the constructs for 30 minutes at 60°C.

14. Discard all well mask constructs that are defective or glossy in appearance from incomplete UV crosslinking.

15. Autoclave all well mask constructs once prior to use for subsequent sterile bioprinting protocols. Store well mask constructs in sterile containers outside of direct sunlight.

16. Autoclave female/female Luer Lock adapters prior to use for subsequent sterile bioprinting protocols, when they are not pre-sterilized.

Pause Point

Procedure 1: Establishing and culturing bioprinted organoids for downstream high throughput imaging and drug screening experiments

TIMING: 3 days

Preparing materials for bioprinting and 3D models/organoid establishment

TIMING: ~1–3 h

1. Prepare the complete serum-free medium used for 3D organoid culture. As an example, when using MammoCult (StemCell Technologies) add the following: 450 mL Mammocult base medium,

50 mL Mammocult supplement, 2.5 mL Hydrocortisone, and 1 mL Heparin, per the manufacturer's instructions.

Critical: Filter all culture media through a 0.22 μm filter prior to use.

2. (Highly recommended) Prepare aliquots of sterile Matrigel prior to starting bioprinting experiments. To prepare aliquots, thaw a stock bottle of Matrigel on ice, and prepare a beaker containing ice in the biosafety cabinet. When the bottle is fully thawed, gently vortex, and on ice in the biosafety cabinet, rapidly pipette 500 to 1,000 μL of Matrigel into pre-chilled 1.5mL microcentrifuge tubes. When they are not immediately used for an experiment, aliquots can be stored in a -20°C freezer and thawed one additional time when needed for use.

Critical: Repeated freeze-thaw cycles can affect the physical properties of Matrigel; avoid using aliquots of Matrigel that have undergone repeat freeze-thaw cycles.

Procedure 1.1: Collecting and counting cells

TIMING: ~30 min

3. Aspirate media from MCF-7 or BT-474 cell plates.

4. Add 10 mL cold 1x PBS, pH 7.4. Shake gently and aspirate all buffer.

5. Add 2 mL 0.05% Trypsin-EDTA and shake well to distribute over the cells.

6. Incubate in a humidified cell culture incubator at 37°C, 5% CO_2 for 5 minutes.

7. Remove the plate from the incubator and view it using a tissue culture microscope to check whether cells are detached.

8. When the cells are detached, use a p1000 pipette to break clumps and strain through a 100 μm cell strainer directly into a 50 mL conical tube containing 10 mL cold complete medium (RPMI 1640 +10% FBS, +1% antibiotic-antimycotic (anti/anti) solution for MCF-7 or BT-474 cells) to obtain a single-cell suspension.

9. Count cells by staining an aliquot of cells (20 μL) with an equal volume of acridine orange/propidium iodide (AO/PI) cell viability stain solution (Nexcelom), adding 20 μL of the

solution to a disposable counting slide, and performing a viable cell count with a Cellometer Auto 2000 counter (Nexcelom) or a similar cell counting device.

10. (Optional) When clumps of cells are observed in the cell suspension during cell counting, repeat step 8 using a smaller cell strainer with either 40 or 70 µm pore sizes, and then repeat step 9.

> **Critical:** Single-cell suspensions are highly preferable because large clumps of cells interfere with accuracy of cell counting and can also result in organoids that grow large enough to affect the integrity of the bioprinted Matrigel constructs in which they grow.

Procedure 1.2: Preparing bioink and 96-well glass-bottom plates

TIMING: ~45 min

Critical: Our standard protocol consists of seeding $5x10^3$ cells per well in 96-well glass-bottom plates using a 4:3 mixture of Matrigel to Mammocult complete medium[20,27,28,38,171,174]. Therefore, we generate a bioink using the same ratio of Matrigel to Mammocult and same concentration of cells, $5x10^5$ cells/mL, for bioprinting. During the printing process, we load cartridges with a total of 1.4 mL of bioink, which includes 800 µL Matrigel, 600 µL Mammocult/cell mixture, and $7x10^5$ total cells. A cartridge set up this way can print up to two full plates of mini-square constructs. Ideal Matrigel bioink prints in mini-square patterns result in consistent depositions of approximately 6–10 µL per well, with uniform volumes printed across the entire plate. Each printed volume spreads into thin, flat, contiguous square-shaped constructs without overflowing into the well center.

> **Critical:** In this procedure, all steps from this point onward are performed on ice. We recommend preparing a small, sterile beaker containing ice in the biosafety cabinet.
>
> **Critical:** Pre-set the temperature of the printhead and the Enviro-Genie rotating incubator (Scientific Industries) to 17°C.

11. Prepare an aliquot of the cell suspension as described above containing $7x10^5$ total cells.

12. Spin at 600g for 5 minutes.

13. Gently aspirate the supernatant without disturbing the pellet.

14. Add 600 µL cold Mammocult to the pellet and resuspend carefully and thoroughly using a p1000 pipette.

15. Add 800 µL Matrigel to the cell suspension and gently pipette up-and-down.

Critical: Avoid generating air bubbles as these interfere with bioprinting.

16. Gently vortex on low setting four times for 5 seconds. Incubate the tube of bioink on ice in between rounds of vortexing.

17. Use a p1000 pipette to load 1.4 mL of bioink into a sterile 3 mL syringe while minimizing the introduction of air bubbles. Orient the syringe so that the opening is facing upward and plunge out as much air as possible, such that the bioink rises to the syringe opening.

Critical: Rapid completion of the subsequent steps in bioink preparation and bioprinting procedures (Procedures 1.2 and 1.3), with strict temperature control, is critical to achieving the desired seeding pattern.

18. Connect the syringe to a sterile 3D bioprinting cartridge using a pre-sterilized Luer Lock connector and push the bioink into the cartridge.

19. Cap the back of the bioprinting cartridge with a sterile end cap.

20. Orient the syringe and cartridge so that the syringe is above the level of the cartridge, and gently flick the cartridge so that any residual bubbles rise into the syringe in the direction of the buoyant force.

21. Remove the Luer Lock connector and cap the front of the cartridge with a sterile tip cap, so that the bioink compartment in the bioprinting cartridge contains at most one single bubble.

Critical: If the bioink compartment contains multiple bubbles, they can potentially clog the needle and cause suboptimal print results.

22. Incubate the bioink cartridge for 30 minutes at 17°C in the Enviro-Genie rotating incubator (Scientific Industries) while rotating at a speed setting of 1/2 RPM.

23. Insert 3D printed, pre-sterilized well mask constructs into a 96 well Cellvis glass-bottom plate, with one construct in each of 12 plate columns.

24. Secure the well mask constructs by placing two rubber bands lengthwise across the plate, one near rows A/B and a second near rows G/H, and then gently press every well mask into its well from the top (**Figure 3.3B**)

Critical step: Make sure that masks are tightly secured and in contact with the glass bottom surface in each well to ensure proper oxygen plasma treatment. If the oxygen plasma treatment through individual well mask constructs are excessive or insufficient, or generate unsuitable preparatory patterns of the glass surfaces of each well and fail to provide the desired seeding geometry for the cell-laden Matrigel bioink, successful bioprinting may require using well mask constructs with a more optimal fit for oxygen plasma treating the plate wells.

Troubleshooting

25. Approximately 30 minutes prior to bioprinting cells, place the Cellvis plate into a PE-25 oxygen plasma cleaner and treat for 30 seconds with oxygen plasma.

Critical step: Oxygen plasma treatment parameters may need adjustments if they are excessive or insufficient or generate unsuitable preparatory patterns of the glass surfaces of each well and fail to provide the desired seeding geometry for the cell-laden Matrigel bioink. We strongly recommend recording oxygen plasma treatment settings for future reference.

Troubleshooting

26. Repeat steps 23–25 on additional Cellvis glass-bottom plates, as desired.

Procedure 1.3: Bioprinting cells in mini-squares for high throughput imaging and drug screening on the HSLCI platform

TIMING: ~15 min

Critical: Printer instruction text files (file extension ".gcode") for the Bio X bioprinter (CELLINK) can be generated and visualized using the DNA Studio software (CELLINK). Alternatively, analogously formatted G-code print instructions for the Bio X bioprinter can be written in a plain text file and saved with the ".gcode" file extension. Other 3D bioprinters may use differently formatted G-code commands to achieve similar results.

Critical: All procedures described below are performed in a biosafety cabinet or laminar flow enclosure to maintain sterility of the cell solution and avoid contamination.

27. Just before the end of 30 minutes incubation of the bioink at 17°C, place the first plasma-treated Cellvis 96-well glass-bottom plate securely into the print bed of the Bio X bioprinter (CELLINK).

28. Run the auto bed leveling function on the bioprinter.

29. At the conclusion of the bioink incubation, remove the bioink cartridge from the Enviro-Genie and cap the back end of the cartridge with a sterile end cap.

30. Flip the cartridge upside down so that the tip points toward the ground and any bubbles rise with buoyant force.

31. Remove the tip cap from the cartridge.

32. Attach a sterile 0.5" 25G blunt needle to the bioink cartridge.

33. Load the cartridge into the temperature-controlled printhead of the bioprinter, preset to 17°C.

34. Prime the needle by extruding a small volume of material at 7 to 15 kPa.

35. User-designated print runs are programmed to start the print head movement from the position where the needle touches the calibration position, which we set at the bottom-right corner of a Cellvis 96-well glass-bottom plate (**Figure 3.3D**). Therefore, calibrate the printer by touching the needle to the bottom-right corner of the plate.

> **Critical step:** Note that the bioink within the needle will undergo gelation over time. Therefore, it is important to run the calibration as quickly as possible.

Critical step: If the bioprinted Matrigel constructs are seeded such that they are misaligned in the x-, y-, or z- axes relative to the well surfaces of a 96-well plate, the alignment of the extrusion needle relative to the plate may need to be adjusted to obtain extruded bioink constructs with the desired geometry and alignment in each well. We strongly recommend recording the movement inputs performed using the bioprinter's UI during this step, as they may be used for reference if this adjustment is necessary.

Troubleshooting

36. Prime the needle again by extruding a small volume of material at a higher pressure of ~40 kPa. Then, prime the needle continuously for a short duration of ~1–2 s to estimate the pressure required to extrude 5 µL to 10 µL per well across an entire plate.

Critical step: Use the lowest pressure required to unclog the needle to minimize shear forces on the cells being bioprinted.

37. Run the bioprinter instruction file for extruding mini-squares into each well of a Cellvis 96-well glass-bottom plate.

Critical step: For best results, bioprinting should be performed as soon as possible after oxygen plasma treatment and bioink incubation.

Critical step: If the bioprinted Matrigel constructs are seeded such that they are misaligned in the x-, y-, or z- axes relative to the well surfaces of a 96-well plate, the user-inputted printer instruction file (a text file with the file extension ".gcode") may need to be adjusted to obtain extruded bioink constructs with the desired geometry and alignment in each well.

Troubleshooting

38. As soon as possible at the conclusion of a plate bioprint, put another oxygen plasma-treated Cellvis 96-well glass-bottom plate into the print bed of the Bio X bioprinter for the next bioprint run.

Critical: To have sufficient bioink to seed a second or third plate, the cartridge loading volumes can be increased up to 3mL. It is important to keep a consistent ratio of Matrigel to Mammocult/cells.

39. Repeat steps 36–37.

Organoid growth and (Optional) daily brightfield imaging

TIMING: 3 days

40. For bioprinted Cellvis 96-well glass-bottom plates intended for subsequent high-throughput QPI and drug screening, place the plate in a humidified cell culture incubator at 37°C, 5% CO_2 for at least 20 minutes to ensure thermal crosslinking of the bioprinted Matrigel constructs.

41. Once the ECM is fully crosslinked, add 100 µL of complete growth media (Mammocult) to each well using a liquid handler.

Critical: To minimize evaporation of growth media, we recommend manually adding 100 µL of warm 1x PBS, pH 7.4, in the plate spaces between wells.

42. Incubate plate(s) in a humidified cell culture incubator at 37°C, 5% CO_2 for three days to grow 3D organoids.

Critical: Our protocols use three days of incubation as described in Tebon et al 2023[174]. For applications that require longer incubation times, such as when bioprinting organoids from patient samples or using frozen specimens rather than fresh cells, it is necessary to replenish or replace the growth media every two to three days.

43. **(**Optional) Image plate(s) daily in brightfield using a whole-well plate imager to assess organoid model appearance.

(Optional) Procedure 1.4: ATP Assay for parallel whole well assessment of cell/organoid viability

TIMING: ~60–75 min

Critical: For plate(s) intended as quality control assessments of the bioprinting protocol (Procedures 1.1–1.3), whole-well brightfield imaging and cell-destructive ATP release assays may be performed within 30 minutes following bioprinting (Procedure 1.3), and steps 45 and 52–59, below, should be skipped because the bioprinted plates do not contain organoid culture media at this point.

Critical: For plates intended for high-throughput QPI and drug screening (Procedures 2.1–2.3), if an alternative high-throughput screening method is desired to validate HSLCI-acquired data, whole-well brightfield imaging and cell-destructive ATP release assays may instead be performed at the conclusion of a three-day HSLCI imaging protocol (Procedure 2.3).

44. Image plate(s) in brightfield using the whole-well plate imager. Then, incubate plate(s) at 37°C, 5% CO_2 until needed.

45. Add 1x PBS, pH 7.4, to each well of a MASTERBLOCK plate corresponding to wells of the bioprinted 96-well plate(s) to be assayed for cell/organoid viability. To each well, add a total of 100 µL PBS per plate that will undergo a terminal ATP assay, plus an excess of 25 µL. Cover the MASTERBLOCK plate and incubate at 37°C, 5% CO_2 until needed.

Critical: For efficiency, we recommend performing this step using a multichannel pipette and a sterile reagent reservoir.

46. Prepare a fresh solution of dispase by dissolving solid dispase in cold, serum free RPMI 1640 medium in a 50 mL tube, to a final concentration of 5 mg/mL.

Critical: Dispase comes as a solid powder and rapidly aggregates in solution. It should always be kept cold and only dissolved immediately prior to usage to avoid aggregation.

Critical: We recommend preparing an excess of 50% of the calculated volume to account for volume losses during filtration as well as to add a minimum 25 µL extra volume to each well of a MASTERBLOCK plate.

47. Invert the tube to dissolve the solid dispase powder without forming bubbles.

48. Once the dispase is fully solubilized, filter the solution through a 0.22μm filter and keep on ice.

49. Add 5 mg/mL dispase to each well of a MASTERBLOCK plate corresponding to wells of the bioprinted 96-well plate(s) to be assayed for cell/organoid viability. To each well, add a total of 50 μL dispase per plate that will undergo a terminal ATP assay, plus an excess of 25 μL. Cover the MASTERBLOCK plate and incubate on ice until needed for ATP assay(s).

Critical: Dispase solution should be kept on ice as much as possible to maximize dispase enzymatic activity and should be used as quickly as possible after it is prepared because dispase readily aggregates in solution.

Critical: For efficiency, we recommend performing this step using a multichannel pipette and a sterile reagent reservoir.

50. Prepare the necessary sets of sterile 300 μL and 50 μL filtered tips for the epMotion 96 liquid handler (Eppendorf) for each plate to be assayed.

51. Retrieve a bioprinted plate, remove the parafilm from around its edges if applicable, and place the plate such that it is centered and secure within the plate holder of the liquid handler.

52. Use the liquid handler with one set of sterile 300 μL tips to aspirate all media by placing the tips at the bottom of the wells in the empty centers.

Critical: Always aspirate and dispense media at the slowest speed setting.

Critical: Visually inspect the bioprinted plate to ensure that it is aligned with the plate holder in the liquid handler and the 300 μL liquid handler tips are centered within each well of the plate.

53. Dispense the aspirated media into a sterile 96-well plate labeled for waste.

54. Repeat steps 52–53 until no media is left in any of the wells and mini-square constructs in each well are visually observable.

55. Retrieve the pre-warmed MASTERBLOCK plate with wells containing 1x PBS, pH 7.4.

56. Use the liquid handler with a second set of sterile 300 µL tips to transfer 100 µL of 1x PBS, pH 7.4, from the MASTERBLOCK plate into the bioprinted plate. Run the aspiration program on the PBS plate, set to aspirate 100 µL from each well, and then dispense these volumes of PBS into the bioprinted plate.

Critical: Always aspirate and dispense media at the slowest speed setting.

Critical: Visually inspect the bioprinted plate to ensure that it is aligned with the plate holder in the liquid handler and the 300 µL liquid handler tips are centered within each well of the plate.

57. Without removing the sterile 300 µL tips used in the previous step, use the liquid handler to aspirate all PBS from the bioprinted plate by placing the tips at the bottom of the wells in the empty centers.

Critical: Always aspirate and dispense media at the slowest speed setting.

Critical: Visually inspect the bioprinted plate to ensure that it is aligned with the plate holder in the liquid handler and the 300 µL liquid handler tips are centered within each well of the plate.

58. Dispense the aspirated PBS into a sterile 96-well plate labeled for waste.

Critical: Always aspirate and dispense media at the slowest speed setting.

59. Repeat steps 57–58 until no PBS is left in any of the wells and mini-square constructs in each well are visually observable.

60. Retrieve the MASTERBLOCK plate with wells containing cold 5 mg/mL dispase, incubated on ice.

Critical: Dispase solution should be kept on ice as much as possible to maximize the enzymatic activity of dispase and should be used as quickly as possible after it is prepared because dispase readily aggregates in solution.

61. Use the liquid handler with a set of sterile 50 µL tips to transfer 50 µL cold 5 mg/mL dispase from each well the MASTERBLOCK plate containing it to the organoid plate. Run the aspiration program on the dispase plate, set to aspirate 50 µL from each well, and then dispense these volumes of dispase into the bioprinted plate.

Critical: Always aspirate and dispense media at the slowest speed setting.

Critical: Visually inspect the bioprinted plate to ensure that it is aligned with the plate holder in the liquid handler and the 300 µL liquid handler tips are centered within each well of the plate.

62. Incubate the plate in a humidified cell culture incubator at 37°C, 5% CO_2 for 25 minutes.

63. Shake the plate for 5 minutes at 800 rpm using an orbital plate shaker.

64. Using a microscope, confirm that the organoids are in solution and released from the mini-square constructs. If not, incubate at 37°C for an additional 5 minutes and shake for an additional 5 minutes at 800 rpm using an orbital plate shaker.

65. Using a multichannel pipette and a sterile reagent reservoir, add CellTiter-Glo 3D Reagent (Promega) to each well of a MASTERBLOCK plate corresponding to wells of the bioprinted 96-well plate(s) to be assayed for cell/organoid viability. To each well, add a total of 100 µL of ATP assay reagent per plate.

Critical: We recommend preparing an excess of 75 µL of ATP assay reagent in addition to the volume required to account for the viscosity of this reagent.

66. Use the liquid handler with a second set of sterile 50 µL tips to transfer 25 µL ATP assay reagent from each well of the MASTERBLOCK plate containing it to the organoid plate. Run the aspiration program on the ATP assay reagent plate, set to aspirate a volume of 25 µL at the slowest speed setting, and then dispense these volumes of ATP assay reagent into the organoid plate, also at the slowest speed setting.

Critical: Always aspirate and dispense media at the slowest speed setting.

Critical: Visually inspect the bioprinted plate to ensure that it is aligned with the plate holder in the liquid handler and the 300 µL liquid handler tips are centered within each well of the plate.

67. Cover plate in aluminum foil to shield it from external sources of light and shake plate for 5 min at 800 rpm using an orbital plate shaker.

68. Incubate plate away from external sources of light for another 20 min at room temperature.

69. Immediately before reading ATP-catalyzed luminescence on the plate reader, remove lid from plate and cover with a plate sealing film.

70. Place the plate in a SpectraMax iD3 plate reader (Molecular Devices), and measure ATP-catalyzed luminescence in all wells of interest using the following parameters:

a. Shake for 5 minutes prior to reading.

b. Read all wavelengths.

c. 500 ms integration time.

71. Repeat steps 51–70 for additional bioprinted plates, as desired.

Procedure 2: Drug treatment of bioprinted organoids and HSLCI operation

TIMING: 3 days

Procedure 2.1: Automated addition of drug treatments to bioprinted plates of organoids

TIMING: ~2–4 h

1. Three days after completion of procedure 1.3 (bioprinting cells in mini-squares for high throughput imaging and drug screening on the HSLCI platform), and at least 4–6 hours prior to drug treatment, prepare a MASTERBLOCK plate of Mammocult growth medium supplemented with the desired drugs. Cover plate and incubate in a humidified cell culture incubator at 37°C, 5% CO_2 until needed. We use 1% DMSO as vehicle for most drug treatments. We recommend

scattering negative control wells (in our case, the 1% DMSO vehicle-treated condition) and positive control wells (in our case, 10 μM staurosporine, a potent pan-kinase inhibitor[125]), across the plate to account for any row effects.

Pause Point

2. Prepare the necessary sets of sterile 300 μL filtered tips for the epMotion 96 liquid handler (Eppendorf) for each plate to be treated.

3. Retrieve the bioprinted plate and place it such that it is centered and secure within the plate holder of the liquid handler.

4. Use the liquid handler with one set of sterile 300 μL tips to aspirate all media by placing the tips at the bottom of the wells in the empty centers.

Critical: Always aspirate and dispense media at the slowest speed setting.

Critical: Visually inspect the bioprinted plate to ensure that it is aligned with the plate holder in the liquid handler and the 300 μL liquid handler tips are centered within each well of the plate.

5. Dispense the aspirated media into a sterile 96-well plate labeled for waste.

6. Repeat steps 4–5 until no media is left in any of the wells and mini-square constructs in each well are visually observable.

7. Retrieve the pre-warmed MASTERBLOCK plate containing the media supplemented with drugs.

8. Use the liquid handler with a second set of sterile 300 μL tips to transfer 100 μL media from the MASTERBLOCK plate containing treatments to the organoid plate. Run the aspiration program on the drug treatment plate, set to aspirate a volume of 100 μL from each well, and then dispense these volumes of drug-treated organoid media into the organoid plate.

Critical: Always aspirate and dispense media at the slowest speed setting.

Critical: Visually inspect the organoid plate to ensure that it is aligned with the plate holder in the liquid handler and the 300 µL liquid handler tips are centered within each well of the plate.

9. Repeat steps 3–8 for additional organoid bioprinted plates, as desired.

10. (Optional) Image plate(s) in brightfield using the whole-well plate imager.

11. If the 96-well glass-bottom cell culture plate containing bioprinted and drug-treated organoids of interest is for a HSLCI drug screening experiment, use parafilm to seal the edges of plate and minimize evaporation during imaging in the dehumidified HSLCI incubator. Then, immediately place the plate in the plate holder of the HSLCI microscope, with well A1 at the top-right of the plate holder.

Critical: Ensure that the parafilm seals the edges of the plate without sticking out underneath the plate in a way that would interrupt plate scanning during the imaging script or cause the plate to be tilted in the plate holder.

Procedure 2.2: Optics adjustment to optimize IR laser signal for autofocusing during raster scanning

TIMING: ~30–60 min

Critical: The optics of the autofocusing arm of the HSLCI build must be adjusted before experiments, as follows: When the z-translation stage is set using a MATLAB-scripted GUI at the desired position to focus the microscope objective on the sample of interest, the IR laser signal detected by the QPD should be focused so that the voltage signal that is inputted into the feedback control box directly correlates to the distance between the objective and the bottom surface of the glass-bottom plate. A small difference in location and intensity of the IR laser signal within the QPD, corresponding to a difference in the distance between the objective and the bottom of the plate, should result in a large change in the QPD voltage signal.

12. Let the plate temperature equilibrate for at least 15 minutes in the dehumidified HSLCI incubator.

13. Ensure that the imaging computer has sufficient storage capacity for the intended imaging experiment.

> **Critical:** The demonstrated imaging setup for organoid experiments, which involves collecting unique FOVs across four scans in each of the interior six columns of a 96-well plate, with a typical imaging interval of 10 minutes between successive scans, requires approximately 12 TB of storage capacity for three continuous days of imaging.

14. Open MATLAB on the imaging computer and run the GUI initialization script (script_initCELL_EXPLORER.m).

15. Put on the appropriate laser safety glasses and turn on the IR laser.

> **Caution:** Be extremely careful to avoid eye damage; IR laser does not induce a blink response! Must not view laser beam directly or indirectly through mirrors/optics.

16. Use the “APT CONTROLS” window of the imaging GUI (**Figure 3.4**) to navigate the stage coordinates to focus on an organoid in the desired focal plane away from the edges of the wells. Using the most recent set of whole-well brightfield images acquired by the plate imager as references, as available, move the plate holder such that the QWLSI camera “Video Preview” window shows a FOV that is focused on an organoid in a known position around 20–40 μm from the bottom of its well.

> **Critical:** We strongly recommend recording these coordinates to enable a user to easily move the plate back to imaging FOVs that are focused on organoids at known positions in the desired focal plane.

17. Open the ThorCam application to stream the IR laser image captured by the ThorLabs camera. The IR laser signal that is reflected off the bottom of the plate toward the QPD for autofocusing

the objective during raster scanning is also captured by the ThorLabs camera to enable visualization of this signal on the imaging computer.

18. On the light path of IR laser used for autofocusing during plate scanning and imaging (to the right of the filter cube), adjust the optics such that the IR laser is being reflected off the bottom of the glass-bottom plate at an area of interest and then back toward the focusing lens in front of the QPD and ThorLabs camera. Adjust the IR laser light path by shifting the position of the laser adjustment mount using the micrometer and adjusting the two 1” mirrors, and make sure that the angle between the fast axis of the quarter wave plate and the polarization plane of the incoming IR light is set to 45° to maximize optical isolation of this laser signal into the light path leading to the QPD. Use the IR alignment disk to confirm that the laser signal is reaching this light path.

19. While watching the image of the IR laser signal in the ThorCam application on the imaging computer, shift the cage plate (the frame for 1” optics) holding the 125mm plano-convex lens along the optical cage assembly in front of the QPD, and adjust the adjacent 1” mirror until the laser spot is visible and focused slightly right of center on the ThorCam window. Then, adjust this mirror and the position of this plano-convex lens such that the input voltage measured by the QPD corresponding to the intensity and position of the IR laser signal has a reading of 1.2 V to 2.0 V as seen in the oscilloscope, while the laser image remains visible and focused slightly right of center on the ThorCam window.

20. Allow all components of the HSLCI system to temperature equilibrate for 5–10 minutes to ensure that the input voltage measured by the QPD remains static to temperature variations, as seen in real time on the oscilloscope. Then, if this voltage has a reading of 1.2 V to 2.0 V on the oscilloscope, navigate to the “controllerGUI” window of the imaging GUI on MATLAB (**Figure 3.4**) and click “Save Setpoint” for closed-loop feedback control of the distance between the microscope objective and the bottom surface of the glass-bottom plate while raster scanning during high-throughput QPI experiments.

21. On the “controllerGUI” window, make sure the proportional integral derivative (PID) controller is turned off and then use the “Ramp” function to oscillate the height of the objective by 2 μm (on the oscilloscope, the signal of the input voltage from the QPD corresponding to the intensity and position of the IR laser image should also be seen oscillating). On the ThorCam window, verify that the image of the IR laser is only moving in the horizontal direction. On the oscilloscope, verify whether the signal of the voltage outputted by the feedback control box to the piezo, which generates corrective z-movement of the objective, is in turn also oscillating linearly and in the same direction as the input voltage.

Critical: The “Ramp” function in the “controllerGUI” window of the imaging GUI enables the user to verify that the height of the objective-piezo stack responds sensitively and linearly to the input voltage corresponding to the IR laser signal in the QPD. This setup ensures that the feedback control system can automatically adjust the height of the objective such that its distance from the bottom of the plate area of interest (and therefore the z-position corresponding to the user’s desired focal height) remains constant through repeated raster scanning during multiday high-throughput QPI experiments.

22. If the signal of the voltage outputted by the feedback control box to the piezo is oscillating as specified with a range of 0.5 to 1.0 V, hit “Ramp” again on the “controllerGUI” window to shut off ramping. If these conditions are not met, repeat steps 18–21.

Troubleshooting

23. In the “controllerGUI” window of the imaging GUI, set parameters for PID gains. We recommend starting with the values of P = 0.1 and I = 0.001.

24. Use the “APT CONTROLS” window of the imaging GUI to navigate the stage coordinates back to the previous in-focus organoid that is in the desired focal plane and away from the edges of the wells. Then, manually move the z-coordinate out of focus by up to 0.040 to 0.050 mm in one direction.

25. In the “controllerGUI” window, hit “PID” to turn on the PID controller of the closed-loop feedback system for autofocusing the objective, and immediately observe the oscilloscope to evaluate the response of the voltage outputted by the feedback control box to the piezo, which generates corrective z-movement of the objective, as well as the “Video Preview” window of the imaging GUI, which should show whether the z-position of the objective immediately and sensitively returns to the previous focal position. Hit “PID” again to turn off the PID controller.

26. Repeat steps 24–25, except manually move the z-coordinate out of focus by up to 0.040–0.050 mm in the opposite direction to evaluate the voltage response outputted by the feedback control box to the piezo.

27. If the corrective voltage response to the piezo to autofocus the objective is sufficiently rapid and sensitive without overshooting, continue running the HSLCI imaging script on MATLAB. Otherwise, repeat steps 23–26 with different inputted values for the PID gain parameters before proceeding.

Procedure 2.3: Imaging bioprinted plates of organoids using HSLCI

TIMING: 3 days

28. Make the following changes to imaging code as necessary:

    a. In the GUI initialization script (script_initCELL_EXPLORER.m), change the movement coordinate limits to ensure that movement of the translation stages during subsequent imaging experiments do not automatically run the plate or plate holder into the objective or another static structure in the HSLCI build.

    b. In the GUI initialization script (script_initCELL_EXPLORER.m), change the default speed, acceleration, and movement step size settings for using the GUI to move the plate with the x-, y-, and z- translation stages to locate objects of interest.

c. In the GUI initialization script (script_initCELL_EXPLORER.m), make sure the configuration file “Obj40xCfg” is called, corresponding to the HSLCI platform setup that uses a 40× objective for subsequent imaging experiments.

d. In the GUI initialization script (script_initCELL_EXPLORER.m) and GUI reinitialization script (script_reinitializeSID4Bio.m), change the exposure time and duration of LED strobe illumination during automated imaging.

Critical: These parameters must be consistent with the code uploaded to the Arduino Nano microcontroller in the feedback control box, which specifies the timing of synchronized triggers of camera captures, LED illumination, and plate holder movements.

e. In the configuration file that is called by the GUI initialization script (Obj40xCfg.m), change the number of full scans of the y-translation stage down and back each column of the 96-well plate that you wish to image, and the number of interferogram image captures triggered during each of these scans.

Critical: These parameters must be consistent with the code uploaded to the Arduino Nano microcontroller in the feedback control box.

f. In the configuration file that is called by the GUI initialization script (Obj40xCfg.m), change the lateral distance between paired scanning movements down and back each column of the 96-well plate that you wish to image.

Critical: We recommend setting this parameter to 0.5mm because the dimensions of the FOV captured by the installed QWLSI camera (SID4-533, Phasics) through the 40× objective (Nikon, NA 0.75) is 0.36mm x 0.36mm.

g. In the configuration file that is called by the GUI initialization script (Obj40xCfg.m), change save directory of captured interferograms on the imaging computer, and create this directory. Also change the save directory of reference interferograms on the imaging computer and create this directory.

Critical: For complete HSLCI drug screening datasets involving continuous image acquisition of up to three days, HSLCI imaging yields enormous volumes of data, and we recommend saving this data into external hard drives of 18 to 24 TB.

h. In the configuration file that is called by the GUI initialization script (Obj40xCfg.m), change the camera gain parameter.

Critical: If reference interferograms and most imaging FOVs seen on the “Video Preview” window contain too many saturated pixels, the camera gain parameter should be decreased. If reference interferograms and most imaging FOVs seen on the “Video Preview” window are too dark and the histograms of their pixel values are heavily skewed toward the minimum, the camera gain parameter should be increased.

i. In the imaging script (script_loopTest.m), set which columns of the 96-well plate will be imaged during each scan of the plate and change the number of imaging loops.

j. In the imaging script (script_loopTest.m), group scanning movements down and back each column into sets of subcolumns as desired for setting up an imaging experiment.

Critical: We group scans for each column into two sets of two subcolumns, for a total of four scans down and back each column – two scans on each side of the column of wells, so that imaging FOVs on opposite sides of each column of wells, corresponding to opposite legs of printed mini-square constructs, can be repeatedly imaged during each programmed imaging loop.

k. In the imaging script (script_loopTest.m), change the starting and ending y-coordinates of each programmed scan of the y-translation stage.

Critical: These parameters must be consistent with the code uploaded to the Arduino Nano microcontroller in the feedback control box.

l. In the hardware-interfacing script called by the imaging script (script_TrigMoveBinary.m), set the movement speed and acceleration settings of movements of the x-, y-, and z- translation stages and programmed scans of the y-translation stages.

Critical: These parameters must be consistent with the code uploaded to the Arduino Nano microcontroller in the feedback control box.

Critical: While the imaging script is running, the feedback control box jogs the z-translation stage up and down to compensate for the spatial limits of the piezo (about 100 µm) during autofocusing of the objective. For these movements, we recommend setting the movement step size to 0.025mm.

m. Re-run the GUI initialization script (script_initCELL_EXPLORER.m) if any changes to the imaging scripts are made in the previous steps.

29. Use the “APT CONTROLS” window of the GUI to navigate the stage coordinates back to the previous in-focus organoid that is in the desired focal plane and away from the edges of the wells.

30. On the “controllerGUI” window, turn on the PID controller function.

31. Use the “APT CONTROLS” window of the GUI to navigate the stage coordinates to locations in the first well of each column that is being imaged [wells B2, C2, D2, E2, F2, and G2], corresponding to odd-numbered subcolumns 1 and 3. Use the most recent set of whole-well brightfield images acquired by the plate imager to attempt to set starting x-coordinates that ensure the subsequent y-movements programmed in the imaging script align the microscope objective with the legs of the bioprinted mini-square constructs in each column being imaged. Record each of these coordinates.

32. Open the variable “well40x”, contained within the configuration file “wells.mat.” In “well40x,” change the starting x- and z- coordinates corresponding to the first and third subcolumns for imaging columns B-G, and then save the variable in the configuration file “wells.mat.”

Critical: Starting and ending y-coordinates on each scan are pre-set by the user in another imaging configuration file, “Obj40xCfg.m” and in the imaging script, “script_loopTest.m,” rather than in the “well40x” variable in “wells.mat.”

33. On the “controllerGUI” window, turn off the PID controller function. Then, re-run the GUI initialization script (script_initCELL_EXPLORER.m) and ensure that the variable “well40x” is called with updated coordinates.

34. On the “APT CONTROLS” window of the GUI, change the step size of z-movement to match the step size programmed in the imaging script for feedback control jogging of the z-translation stage up and down to compensate for the spatial limits of the piezo (about 100 μm) during autofocusing of the objective. For these movements, we recommend setting the movement step size to 0.025mm.

35. Use the “APT CONTROLS” window of the GUI to navigate the stage coordinates back to the previous in-focus organoid that is in the desired focal plane and away from the edges of the wells.

36. On the “controllerGUI” window, turn on the PID controller function. Then, navigate to the starting coordinates of as many imaging subcolumns as desired, which do not have to be odd-numbered subcolumns, and move the y-translation stage along its pre-programmed movement range in the imaging script. This step is to ensure that plate scanning lines up the microscope objective with the legs of the bioprinted mini-square constructs in the 96-well plate, and to verify that potential imaging FOVs visible on the “Video Preview” window of the GUI contain organoids that are in focus.

37. If the bioprinted plate of organoids contains thin, flat, square-shaped constructs in each well undergoing imaging on the HSLCI platform, and the whole-well brightfield images acquired by the plate imager confirms that bioprinted organoids are growing, but those organoids are not visible on the “Video Preview” window when using the GUI to perform the y-axis movements inputted in

the imaging script, repeat steps 29–36 to align the y-translation stage plate holder movements in the imaging script with the legs of the bioprinted mini-square constructs in the 96-well plate.

38. On the “controllerGUI” window, turn off the PID controller function. Then, use the “APT CONTROLS” window of the GUI to navigate the stage coordinates back to the previous in-focus organoid that is in the desired focal plane and away from the edges of the wells, before turning on the PID function again in the “controllerGUI” window.

39. With the most recent set of whole-well brightfield images acquired by the plate imager as references, use the “APT CONTROLS” window of the GUI to navigate to xy-coordinates corresponding to fields of view with uniformly flat layers of bioprinted ECM and without cells, organoids, or debris present.

40. On the “CELL EXPLORER” window, press “Reference” to capture a reference interferogram. Record the coordinates of reference FOVs and their relative positions within the wells in which they are located. Rename the reference image in its saved file location so that the next saved reference image does not overwrite it.

41. Repeat steps 39–40 at least 8 times, making sure to capture reference interferograms at multiple xy-coordinates corresponding to positions in the legs of bioprinted mini-squares that are closer to column A and multiple additional coordinates corresponding to positions in the legs of bioprinted mini-squares that are closer to column H.

> **Critical:** At least two suitable reference images must be captured: one from a FOV in the leg of any mini-square construct that is closest to column A, corresponding to the first of two legs of the mini-square that are scanned when running the imaging script, and one from a FOV in the leg of any mini-square construct that is closest to column H, corresponding to the opposite leg of the mini-square constructs, which is also scanned during imaging (**Figure 3.3G**). We strongly recommend recording the relative position of

these reference FOVs within the well of the 96-well plate to ensure acquisition of suitable reference images, as described.

Critical: If necessary, phase unwrapping using a reference image from the same relative location within a well of a 96-well plate, but from a different experiment, could still feasibly yield high-quality phase images if the alignment of the illumination LED optical path and the orientation of the plate holder were unchanged between experiments.

42. On the “controllerGUI” window, turn off the PID controller function. Then, on MATLAB, run the imaging script (script_loopTest.m), and check that .bin files each containing a full scan of interferograms are saving into the previously inputted directory.

Critical: For complete HSLCI drug screening datasets involving continuous image acquisition over three days, HSLCI imaging yields enormous volumes of data, which we recommend saving on external hard drives of 18 to 24 TB.

43. At the conclusion of the imaging script, verify that image acquisition was successful for the complete dataset and remove the organoid plate from the HSLCI incubator.

Caution: Safest practice is to always wear laser safety goggles when opening the HSLCI incubator for any reason to avoid eye damage from the IR laser, which does not induce a blink reflex.

Pause Point

(Optional) ATP Assay for parallel whole well assessment of cell/organoid viability

TIMING: ~60–75 min

Critical: If an alternative high-throughput screening method is desired for validation of organoid-level data acquired by HSLCI, whole-well brightfield imaging and cell-destructive ATP release assays may be performed at the conclusion of three days of continuous label-free imaging on the HSLCI platform (Procedure 2.3). Please refer to (Optional) Procedure 1.4 (ATP Assay for parallel well-level assessment of cell/organoid viability).

Procedure 3: Data analysis of HSLCI results

TIMING: ~8 days

Procedure 3.1: Unwrapping interferograms

TIMING: ~2 days

1. Ensure that the HSLCI data analysis computer has access to the interferogram files acquired by HSLCI in Procedure 2.3 and at least 5 TB of available storage space to enable the user to perform desired downstream analyses.

2. On the data analysis computer, edit the unwrapping function (read_unwrapColumn_stack.m) on MATLAB to ignore interferograms corresponding to imaging FOVs that are between wells.

3. Change the reference image filename to point to a reference image from a field of view in a leg of a bioprinted mini-square closer to column A, and then run the camera manufacturer's DRM script.

> **Critical step:** Interferograms from FOVs corresponding to opposite legs of mini-square constructs must be unwrapped using the reference interferogram from the matching side of the well due to non-negligible differences in optical contribution of the imaging setup in imaging FOVs on either side of the empty center of each well.
>
> **Critical:** Unwrapping images acquired using the Phasics QWLSI camera is dependent on the manufacturer's DRM.

4. Run the unwrapping script (processFilesHSLCI_stack.m) on the analysis computer for all interferograms captured from scans in the legs of bioprinted mini-squares that are closer to column A, after changing the relevant arguments within "processFilesHSLCI_stack.m" and "read_unwrapColumn_stack.m." This script should generate phase images corresponding to different imaging frames over time at the same FOV into stacks of time-series phase images corresponding to each FOV and output them into .mat files.

Critical: This output requires hundreds of GB of storage space for a typical three-day HSLCI imaging dataset. The specific output file format was designed to minimize the number of files so that data analysis and transfer are not slowed down.

Troubleshooting

Pause Point

5. Change the reference image filename to point to a reference image from a FOV in a leg of a bioprinted mini-square closer to column H, and then run the camera manufacturer's DRM script again.

Critical step: Interferograms from FOVs corresponding to opposite legs of mini-square constructs must be unwrapped using the reference interferogram from the matching side of the well due to non-negligible differences in optical contribution of the imaging setup in imaging FOVs on either side of the empty center of each well.

Critical: Unwrapping images acquired using the Phasics QWLSI camera is dependent on the manufacturer's DRM.

6. Run the unwrapping script (processFilesHSLCI_stack.m) on the analysis computer for all interferograms captured from scans in the legs of bioprinted mini squares that are closer to column H, after changing the relevant arguments within "processFilesHSLCI_stack.m" and "read_unwrapColumn_stack.m."

Critical: This output requires hundreds of GB of storage space for a typical three-day HSLCI imaging dataset. The specific output file format was designed to minimize the number of files so that data analysis and transfer are not slowed down.

Troubleshooting

Pause Point

Procedure 3.2: Analysis pipeline code

TIMING: ~6 days

7. Install Docker Desktop on the HSLCI data analysis computer if it is not already installed, and ensure Docker is running in the background.

8. Using a Linux distribution on the data analysis computer, install nextflow if it is not already installed. Additional information instructions are accessible from the readme file on the included code repository (see Code Availability).

9. Edit the input .csv file that lists the drug treatment conditions tested in the HSLCI imaging experiment to be analyzed, and the wells of the 96-well plate that corresponds to each condition.

10. Edit the configuration file, “hslci_pipeline.config,” with the input directory of the .mat files outputted by the unwrapping script, the full path to the input .csv file listing wells corresponding to each drug treatment condition, and the desired output directory for the time-series biomass data outputted by the data analysis pipeline script.

11. Run the data analysis pipeline script, “main.nf,” which includes image segmentation, organoid tracking, and track classification, by following the instructions in the readme file on the included code repository (see Code Availability).

Troubleshooting

12. Perform desired single organoid scale analyses using the outputted time-series biomass data corresponding to each imaging FOV, imaged well, and drug treatment condition.

Troubleshooting

Troubleshooting advice can be found in **Table 3.1**.

Step	Problem	Possible reason	Solution
Procedure 1, Step 24	BioMed Amber Resin well masks do not fit into 96-well glass-bottom plates	Well masks were washed in 99% IPA for too long and swelled	Decrease the duration of 99% IPA washes after 3D printing well masks
		Well masks were not fully dried from the final 99% IPA wash prior to UV crosslinking	Blast the well masks with compressed air and let them dry completely prior to UV crosslinking
Procedure 1, Steps 27–37	Bioprinted constructs are misaligned within the wells	The inputted bioprinter instruction file used movement coordinates that were misaligned with the wells of the	Using whole-well brightfield images of the misaligned plate as a reference, generate a new bioprinter instruction file adjusted such

	of the 96-well plate in the x- or y- direction	96-well plate in the x- or y-direction	that bioprinted constructs will be centered in each well of the 96-well plate
		Extrusion needle was positioned inaccurately in the x- or y- direction during calibration	Adjust the position of the extrusion needle in the x- or y- direction during bioprinter calibration such that bioprinted constructs will be centered in each well of the plate
Procedure 1, Steps 27–37	Extrusion needle scratches the glass surface of the plate during bioprinting	The inputted bioprinter instruction file used movement coordinates that were misaligned in the negative z-direction	Using whole-well brightfield images of the misaligned plate as a reference, generate a new bioprinter instruction file adjusted such that bioink will extrude at a suitable height above the surface of the plate
		Extrusion needle was positioned too closely to the surface of the plate during calibration	Adjust the position of the extrusion needle in the z- direction during bioprinter calibration such that bioink will extrude at a suitable height above the surface of the plate
Procedure 1, Steps 27–37	Bioprinted constructs are rounded and too thick (greater than ~150 µm)	The inputted bioprinter instruction file used movement coordinates that were misaligned in the positive z-direction	Using whole-well brightfield images of the misaligned plate as a reference, generate a new bioprinter instruction file adjusted such that bioink will extrude at a suitable height above the surface of the plate
		Extrusion needle was positioned too far away from the surface of the plate during calibration	Adjust the position of the extrusion needle in the z- direction during bioprinter calibration such that bioink will extrude at a suitable height above the surface of the plate
Procedure 1, Steps 24–25 Procedure 1, Steps 27–37	Matrigel bioink spreads up the walls of wells during extrusion, and bioprinted constructs appear patchy	Oxygen plasma treatment resulted in excessive functionalization of the glass surfaces and walls of wells in a 96-well glass-bottom plate	Repeat the bioprinting procedure using BioMed Amber Resin well masks with a slightly different fit within the wells of the 96-well plate, and decrease the duration and intensity of oxygen plasma treatment if necessary
Procedure 1, Steps 24–25 Procedure 1, Steps 27–37	Bioprinted constructs are rounded and uneven, with nonrandom distribution of embedded cells	Oxygen plasma treatment resulted in insufficient functionalization of the glass surfaces of wells in a 96-well glass-bottom plate	Repeat the bioprinting procedure using BioMed Amber Resin well masks with a slightly different fit within the wells of the 96-well plate, and increase the duration and intensity of oxygen plasma treatment if necessary
Procedure 1, Steps 33–37	Matrigel bioink spreads into the centers of wells during extrusion	Extrusion pressure was too high during bioprinting	Try bioprinting at lower extrusion pressures
Procedure 1, Steps 27–37; Procedure 1, Steps 46 – 51 and 60–71	Volume of bioink extruded into each well qualitatively or quantitatively decreases with the order of wells bioprinted in a single 96-well plate	Premature crosslinking of Matrigel bioink	Ensure adequate temperature control throughout the entire duration of the bioprinting procedure
		The inputted bioprinter instruction file used movement coordinates that were misaligned in the negative z-direction	Using whole-well brightfield images of the misaligned plate as a reference, generate a new bioprinter instruction file adjusted such that bioink will extrude at a suitable height above the surface of the plate
		Extrusion needle was positioned too closely to the	Adjust the position of the extrusion needle in the z- direction during bioprinter calibration

		surface of the plate during calibration	such that bioink will extrude at a suitable height above the surface of the plate
		Extrusion needle was clogged by bubbles	Avoid generating bubbles while loading the cell-laden Matrigel bioink into the bioprinter cartridge
Procedure 2, Steps 14–22	The “Ramp” function in the imaging GUI does not generate a corresponding linearly oscillating output voltage to the piezo to adjust the height of the objective	The feedback control system and its relevant optics were not optimized for keeping the objective focused at a constant distance from the 96-well plate bottom surface	Adjust the micrometer and the rightmost 1” mirror such that the rightmost portion of the IR laser optical path is further offset from the rest of the optical cage assembly, and that on the imaging computer, the signal of the IR laser reflected off the 96-well plate bottom surface is visible on the ThorCam program
			Adjust the position of the focusing lens on the optical track in front of the QPD, as well as the 1” mirror adjacent to this lens, such that the IR laser reflection visible on ThorCam changes in position and sharpness
			Adjust the aperture of the IR laser or QPD, such that the IR laser reflection visible on ThorCam changes in intensity
Procedure 2, Steps 38–43; Procedure 3, Steps 1–6	Unwrapped phase shift images in dataset are of poor quality and full of background artifacts that interfere with analysis of biomass data	The quality of the reference image used for phase unwrapping was suboptimal	Attempt phase unwrapping using a different reference image, from a FOV corresponding to a thin, flat section of the bioprinted ECM construct that is devoid of cells, organoids, and debris
		The reference image used for phase unwrapping was acquired from a FOV on the opposite side of the well relative to the acquired interferograms that were being unwrapped	Attempt phase unwrapping using a reference image located in the same leg of the bioprinted mini squares as the acquired interferograms that are being unwrapped
Procedure 3, Step 9–11	Organoids are not segmented accurately within high-quality phase shift images with low background noise	Organoid phenotypes in phase shift images were substantially different than those of the MCF-7 and BT-474 cell line–derived organoids that were manually segmented and used as the ground truth for training the U-Net segmentation algorithm	Obtain phase shift images of organoids that are of the same lineage, or otherwise of similar phenotypes as observed in HSLCI-acquired phase shift images, and manually segment these images for use as the ground truth for re-training the U-Net segmentation algorithm, before re-analyzing the dataset using the analysis pipeline code with the training data updated
Procedure 3, Step 9–11	Organoids are segmented but not tracked accurately within high-quality phase shift images with low background noise	Organoid phenotypes in biomass accumulation data were substantially different than the time-series biomass behavior of MCF-7 and BT-474 cell line–derived organoids that were tracked and used as the ground truth for training the XGBoost track classification algorithm	Re-train the XGBoost algorithm for track classification by using time-series biomass data from organoids that are derived from the same cell source if possible, or otherwise are of similar phenotypes as observed in HSLCI-acquired phase shift images, before re-running the analysis pipeline code with the training data updated

Table 3.1: Troubleshooting table.

Timing

Procedure 1: Establishing and culturing bioprinted organoids for downstream high throughput imaging and drug screening experiments: three days

Steps 1–2, Preparing materials for bioprinting and 3D models/organoid establishment: ~1–3 h

Steps 3–10, Collecting and counting cells (Procedure 1.1): ~30 min

Steps 11–26, Preparing bioink and 96-well glass-bottom plates (Procedure 1.2): ~45 min

Steps 27–39, Bioprinting cells in mini-squares for high-throughput imaging and drug screening on the HSLCI platform (Procedure 1.3): ~15 min

Steps 40–43, Organoid growth and (optional) daily brightfield imaging: three days

Steps 44–71, (Optional) ATP Assay for parallel whole well assessment of cell/organoid viability (Procedure 1.4): ~60–75 min

Procedure 2: Drug treatment of bioprinted organoids and HSLCI operation: three days

Steps 1–11, Automated addition of drug treatments to bioprinted plates of organoids (Procedure 2.1): ~2–4 h

Steps 12–27, Optics adjustment to optimize IR laser signal for autofocusing during raster scanning (Procedure 2.2): ~30–60 min

Steps 28–43, Imaging bioprinted plates of organoids using HSLCI (Procedure 2.3): three days

(Optional) ATP Assay for parallel whole well assessment of cell/organoid viability (Procedure 1.4): ~60–75 min

Procedure 3: Data analysis of HSLCI results: ~eight days

Steps 1–6, Unwrapping interferograms (Procedure 3.1): ~2 days

Steps 7–12, Analysis pipeline code (Procedure 3.2): ~6 days

Anticipated results

Here, we report a multi-step protocol for automatic printing, high throughput drug screening, and parallel biomass profiling of 3D cell models using two breast cancer cell lines, MCF-7 and BT-474, as example cell sources (**Figure 3.1**). This protocol has been successfully applied in our laboratory to tumor organoid models derived from a variety of cell and tissue sources, including PDTOs.

Implementation of our bioprinting workflow will generate 96-well glass-bottom plates with cells embedded in thin, flat, and uniform square-shaped Matrigel constructs in each well (**Figure 3.3C**). We show an example of results of an ATP release assay performed immediately following bioprinting (**Figure 3.3E**), and time-course brightfield images of bioprinted organoids that grow over the first three days after seeding (**Figure 3.3F**). We recommend performing these two independent quality checks before using bioprinted plates of organoids for downstream experiments. When testing the bioprinting workflow prior to using either a new cell line or primary patient material as a cell source, it is important to image each bioprinted plate and record the inputted coordinates for bioprinter movements during extrusion in case troubleshooting is required. Furthermore, we advise users testing new cell sources to perform additional validation experiments, including histological and biomolecular comparisons with the equivalent manually-seeded organoid models, to confirm that bioprinting did not substantially alter tumor biology; further details can be found in the original publication[174]. While we show that this “mini square” seeding geometry for bioprinted organoids is conducive to automated addition of media using liquid handlers[27,38,174] and downstream high throughput imaging using the HSLCI platform[174] (**Figure 3.3G–H**), we recognize that users may wish to incorporate bioprinted organoids into other workflows. We anticipate that the ability to rapidly and reproducibly seed entire plates of 3D organoids that grow robustly in a thin (~70 µm) layer of Matrigel will also facilitate the application of other high throughput and high-content organoid imaging modalities[44,45,77].

In this protocol, we provide instructions for constructing our HSLCI optical imaging setup, customizing HSLCI operation for imaging bioprinted organoids seeded in 96-well glass-bottom plates in the desired “mini square” geometry, and performing multiparametric, time-resolved analyses of cellular phenotypes (**Figure 3.2**). We also provide a detailed protocol for performing drug screening experiments after three days of cell growth using liquid handlers to treat the bioprinted 3D models with drugs or agents of interest. We include details for using a liquid handler to perform an ATP assay at the conclusion of three days of continuous drug treatment and label-free QPI. Moreover, we advise users testing new cell sources to perform this assay or an alternative endpoint chemosensitivity assay for validation of HSLCI data with well-level drug sensitivity results acquired in parallel[44,183]. The duration of organoid growth and imaging are adaptable as needed for different organoid models.

Successful implementation of the complete protocol will result in the generation of very large datasets including hundreds of thousands of phase shift images of drug-treated organoids after each of 1,000+ FOVs is repeatedly imaged by QPI at intervals of ~10 minutes between frames for three consecutive days. If the bioprinting procedure successfully generates an entire plate of viable organoids in the desired uniformly thin (~70 μm) layer of Matrigel, and the autofocusing module of the HSLCI platform is set up to be focused on a focal plane in the center of this layer, then many of the imaging FOVs will include tracked organoids that stay in focus over multiple days of continuous imaging and yield interpretable time-series biomass data. We show examples of phase shift images of drug-treated MCF-7 and BT-474 cell line–derived organoids, which include organoids of a wide range of sizes and shapes (**Figure 3.5A**). Completion of the multi-step QPI analysis pipeline also generates time-series tracks of the biomass and other selected morphological and biophysical characteristics corresponding to segmented organoids at each FOV, and an output file with XGBoost-predicted classifications of whether each organoid biomass versus time track is valid based on training parameters.

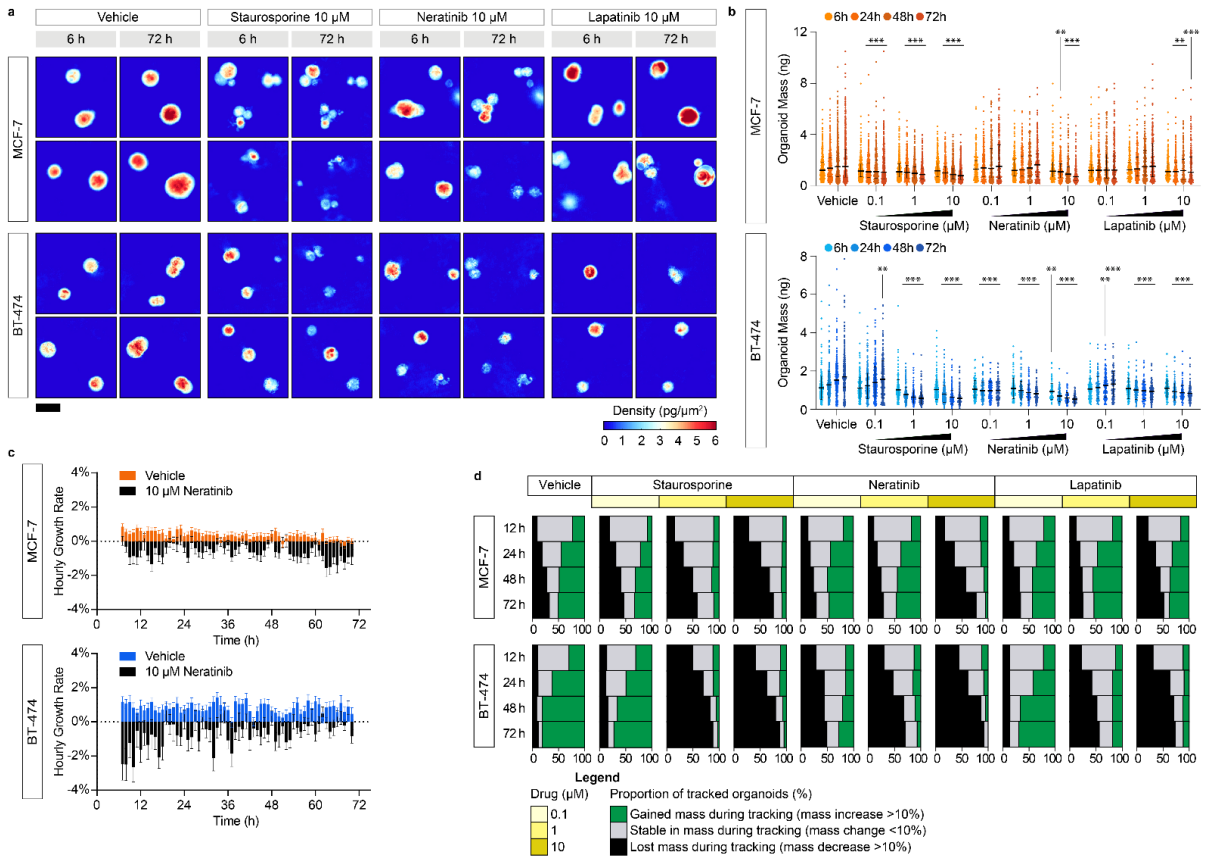

Figure 3.5: HSLCI enables high-throughput, longitudinal drug response profiling of 3D organoid models of cancer. (A) Representative HSLCI-acquired phase images of MCF-7 and BT-474 cell line–derived organoids treated with staurosporine, neratinib, and lapatinib at concentrations of 10 µM. Scale bar is 40 µm. **(B)** Biomass of tracked MCF-7 and BT-474 organoids by treatment. For each treatment condition, each column represents the biomass distribution at 6, 24, 48, or 72 h post-treatment (left to right). Black horizontal bars represent the median and error bars represent the interquartile range (IQR) of the distribution. Statistical significance was assessed using two-tailed Mann-Whitney U-tests against the vehicle control at the respective time points. $p < 0.05$ is denoted by *, $p < 0.01$ is denoted by **, and $p < 0.001$ is denoted by ***. **(C)** Representative hourly growth rate comparison (percent biomass change per hour) between vehicle-treated organoids and organoids treated with 10 µM neratinib. Data are presented as mean growth rate ± standard error of the mean (SEM). **(D)** Plots showing the proportion of tracked organoids in each condition that gained more than 10% of their initial mass (green), lost more than 10% of their initial mass (black), or maintained a mass within 10% of their initial mass (gray) at 12, 24, 48, and 72 h after treatment addition. Reprinted with permissions from Tebon et al, 2023.

Successful completion of the full protocol as described above can be reasonably expected to generate interpretable time-series biomass data for 1,000 to 10,000 individual organoids per experiment. We demonstrate that our analysis pipeline can analyze organoids with a wide range of biomasses, including with biomasses equivalent to dozens of constituent cells, as well as single cells occasionally present within the ECM (**Figure 3.5B**). Individual MCF-7 cells growing in 3D measured approximately 300–600 pg, whereas single BT-474 cells in 3D culture ranged from about 250–500 pg, consistent with previous QPI measurements of MCF-7 and BT-474 cells in 2D culture[54,59]. Lastly, we demonstrate that these organoid-level biomass data can be used to make growth rate comparisons among different populations and treatment groups (**Figure 3.5C**), and to quantify drug response heterogeneity, including by identifying rare, drug-resistant organoid subpopulations (**Figure 3.5D**). We anticipate that studies of patient-derived tumor organoid drug responses will be a direct application of this protocol.

Data availability

HSLCI imaging data presented in **Figure 3.5**, as well as corresponding source data and all training datasets used in the analysis of these data, are accessible in the BioImage Archive on Biostudies under accession code S-BIAD616. Source data are provided in Tebon et al. 2023[174].

Code availability

Code used for imaging and data analysis is publicly available on GitHub at https://github.com/uclahs-soragnilab/hslci_pipeline or Zenodo[170] (https://doi.org/10.5281/zenodo.7787339). A ready-to-use Docker container image for running the data analysis pipeline code is publicly available on Dockerhub at: https://hub.docker.com/r/soragnilab/unetsegmentation.

Supplementary Information

Supplementary Tables

Parameter Name	Setting
Detector	Manual annotation
Simplify contours	FALSE
Target channel	1
Spot filtering: Area	Remove spots < 250 square pixels
Tracker	Sparse LAP Tracker
Linking max distance	90 pixels
Linking feature penalty: ellipse major	4
Linking feature penalty: area	4
Allow gap closing	True
Gap-closing max distance	60 pixels
Max frame gap	30 frames
Gap closing feature penalty: ellipse major	1
Gap closing feature penalty: area	1
Allow track segment splitting	False
Allow track segment merging	False
Track filtering: track duration	Remove tracks <10 frames in length

Table S3.1: Organoid tracking parameters. The TrackMate program was used for tracking segmented objects in time-series quantitative phase imaging (QPI) datasets.

Parameter Name	Setting
alpha	0
approxcontrib	FALSE
base_score	0.5
booster	gbtree
colsample_bylevel	1
colsample_bynode	1
colsample_bytree	1
disable_default_eval_metric	FALSE
eta	0.3
feature_selector	cyclic
gamma	0
grow_policy	depthwise
lambda	1
lambda_bias	0
max_bin	256
max_delta_step	0
max_depth	6
max_leaves	0
min_child_weight	1
missing	NA
monotone_constraints	0
normalize_type	tree
nthread	1
num_parallel_tree	1

Parameter Name	Setting
objective	binary:logistic
one_drop	FALSE
outputmargin	FALSE
predcontrib	FALSE
predictor	cpu_predictor
predinteraction	FALSE
predleaf	FALSE
print_every_n	1
process_type	default
rate_drop	0
refresh_leaf	TRUE
reshape	FALSE
seed_per_iteration	FALSE
sample_type	uniform
sampling_method	uniform
scale_pos_weight	1
skip_drop	0
strict_shape	FALSE
subsample	1
top_k	0
training	FALSE
tree_method	auto
tweedie_variance_power	1.5
verbose	1

Table S3.2: XGBoost Classifier hyperparameters. Reprinted with permissions from Tebon et al, 2023.

Acknowledgements

We would like to thank Dr. Kevin Leslie and Dr. Dian Huang for their prior contributions in testing the imaging scripts and workflow upon which ours was built. We would also like to thank Dr. Steven Jonas for generously allowing access to laboratory equipment. This work was supported by the Air Force Office of Scientific Research (FA9550-15-1-0406, to M.A.T.), the Department of Defense (W81XWH2110139, to M.A.T.), a National Science Foundation Graduate Research Fellowship (DGE-2034835, to B.W.), a Eugene V. Cota Robles Fellowship (to B.W.), a JCCC Fellowship (to P.J.T.), and a UCLA DGSOM Seed Award (to A.S.). It was additionally supported by NIH T32HL144449 (to T.L.N.), R01CA244729 (to A.S.), R01CA244729-03S1 (to A.S.), NIH R01GM114188 (to M.A.T.), R01GM073981 (to M.A.T.), R01CA185189 (to M.A.T.), R21CA227480 (to M.A.T.), R01GM127985 (to M.A.T.), and P30CA016042 (to M.A.T.). B.W., P.J.T., A.S., and M.A.T. are inventors on patent application 18/037,646 (U.S. Patent and Trademark Office) filed by The Regents Of The University Of California covering certain aspects of the bioprinting process. A.S. is a founder and owner of Icona BioDx.

Chapter 4: Conclusions and future directions

While 3D tumor organoid models have become established alongside cancer cell lines as foundational tools for basic and translational studies of cancer biology[16–28], their application for FPM is particularly compelling due to key advantages over 2D cell line models[18,21,24,25,30–32,34,35], including their efficiency of derivation from many tumor types[18,19,23–26,92] and superior modeling of *in vivo* tumor physiology[21,24,30–32]. In recent years, PDTOs have become the most prevalent personalized cancer model for FPM assays testing drugs on primary patient tumor samples, and several studies have demonstrated their promise by correlating the results of these PDTO-based assays with clinical responses to treatments[27,28,39–43]. These developments have inspired further clinical trials, using a variety of organoid drug screening strategies, with the ultimate goal of providing biomarkers to stratify patients for therapy[25,29].

The work in this thesis presents a new application of high-speed live cell interferometry for high throughput, label free, and highly time-resolved QPI of 3D-cultured organoid models of cancer and describes the development of this method. Extrusion bioprinting[173] was used to pattern a biomimetic extracellular matrix (ECM) in glass-bottom 96-well plates in the desired geometry that maximizes organoid imaging efficiency and sampling depth for this application; incorporation of machine learning–based tools in a subsequent image analysis pipeline was also required to efficiently output time-resolved biomass data from individual organoids imaged in each of over 1,000 fields of view in a typical experiment. The combination of bioprinting, HSLCI, and machine learning technologies in the complete organoid drug screening pipeline enabled label-free quantification of the biomass, growth, and drug responses of thousands of discrete tumor organoids in each individual 3-day imaging experiment. MCF-7 and BT-474 cell line–derived organoids, representing two distinct molecular subtypes of breast cancer[35,111], were established by bioprinting without adverse effects on viability or measurable changes in molecular features caused by the bioprinting process. Subsequently, differences in those models' responses to two

molecularly targeted small molecule drugs, lapatinib and neratinib, which are clinically indicated for HER2-overexpressing disease[10,11,186], were detected that were consistent with the expression levels of the clinically validated HER2 biomarker observed in the respective models[35,111], as well as with concurrent well-level, bulk organoid viability data from ATP release assays performed at the conclusion of label-free HSLCI imaging.

One key advantage of the protocol described, relative to existing organoid drug screening methods[2,27,39,43,62–65,83,84,154,155,172,181,187], is its combination of throughput, time resolution, and number of organoids sampled. While HSLCI measurements of 3D organoid cultures quantified the size heterogeneity of imaged objects ranging from single ECM-embedded cells to large organoids containing dozens of cells, the ATP release assay results corresponding to those HSLCI-imaged, drug-treated plates could not consider the contribution of those organoid size distributions to well-level viability. Furthermore, the imaging interval of ~10 minutes is sufficient to observe temporal changes in biomass dynamics, and the time-resolved, organoid-level information returned by HSLCI enables the characterization of heterogeneous organoid growth and drug response behaviors and identification of rare organoid subpopulations among those observed behaviors – information that is also inaccessible using traditional chemosensitivity assays[2,188,189]. In the clinical setting, anti-cancer drug therapies often fail due to the persistence of rare subpopulations of cells that exhibit drug resistance or adaptive drug-tolerance[68–70,190]. Therefore, the rare subpopulations of organoids that grow unabated or temporarily lose mass before resuming growth among a population of PDTOs that lose mass in response to strong drug treatments may prove to be extremely pertinent to clinical outcomes. Additionally, preliminary work has confirmed the feasibility of growing bioprinted PDTO models and obtaining functional drug response data using the HSLCI organoid screening pipeline even when primary patient tumor material is limited in availability (**Figure 4.1**). In one proof-of-concept experiment, PDTOs grown from a biobanked metastatic leiomyosarcoma tumor sample were screened for their responses

to a panel of drug treatments of interest, including single-agent therapies and two-drug combinations commonly used in clinical management of advanced leiomyosarcoma[191,192], advanced breast cancer[10,11], and other sarcomas[28,193,194]. Among these drug treatments, alpelisib, a selective phosphatidylinositol 3-kinase (PI3K) inhibitor[195] that is used with fulvestrant for treatment of a subset of ER-positive, HER2-negative advanced breast cancers[10,196], was identified to induce a significant decrease in organoid biomass accumulation rates relative to vehicle treatment (**Figure 4.1**), although alpelisib monotherapy is not normally clinically indicated for treating patients with advanced leiomyosarcoma[191,192]. Taken together, these results justify future experiments investigating whether analogous HSLCI biomass profiling data of PDTOs can be used to improve treatment selection for patients with solid cancers.

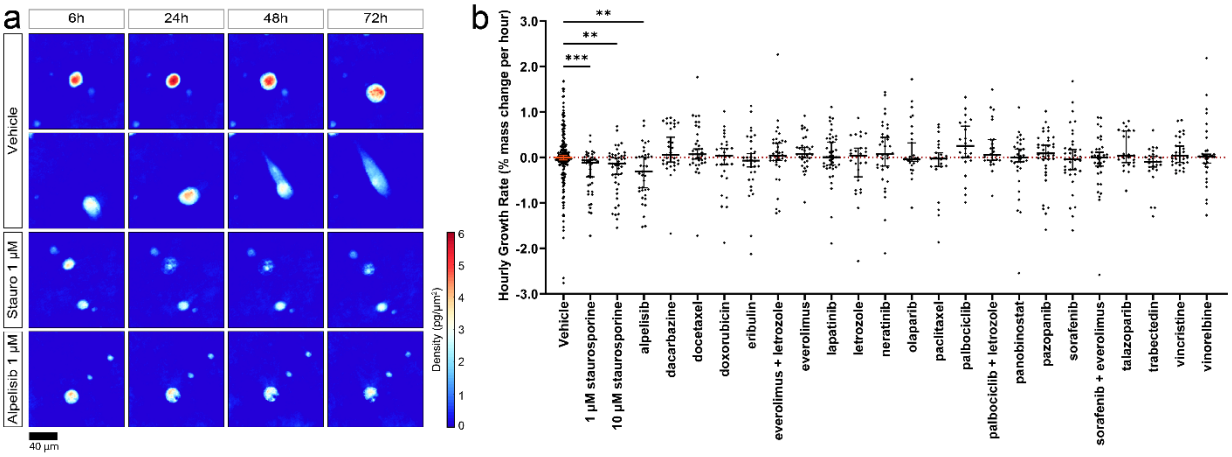

Figure 4.1: HSLCI enables high-throughput, longitudinal drug response profiling of patient-derived tumor organoids (PDTOs). (A) Representative HSLCI-acquired phase images of vehicle-treated and drug-treated leiomyosarcoma PDTOs. All primary tumor samples were obtained from consenting patients (UCLA IRB #10-001857). **(B)** Hourly growth rates of HSLCI-imaged leiomyosarcoma PDTOs by drug treatment condition. All drug treatments were performed at a concentration of 1 µM, with the exception of 10 µM staurosporine. Horizontal bars represent median and error bars represent IQR. $p < 0.05$ is denoted by *, $p < 0.01$ is denoted by **, and $p < 0.001$ is denoted by ***.

The most compelling future direction for assaying organoid biomass accumulation using HSLCI as described is establishing clinical correlations for disease contexts in which biomarker-

indicated treatment selection is unavailable or otherwise lacking. One such potential use case of HSLCI is for functional drug screening of ovarian cancer PDTOs. Even with the current standard treatments, advanced ovarian cancer has a 5-year survival rate of 29% after diagnosis[197], accounting for both patients with platinum-resistant disease as defined by disease progression within six months prior to completion of standard first-line platinum-based chemotherapy, and those with platinum-sensitive disease, as determined by lack of disease progression at this predefined clinical endpoint[12,197,198]. These two groups of patients have drastically different prognoses and treatment outcomes[12,198]; patients with platinum-resistant ovarian cancer fare worse because subsequent treatment options are limited to single-agent chemotherapy drugs with low expected response rates of less than 15%, and evidence-based strategies for choosing among them currently do not exist[12,197]. Furthermore, no biomarkers exist to rapidly identify that a patient's ovarian cancer is platinum-resistant in advance of administering systemic drug treatments[199,200], and management of advanced platinum-resistant disease becomes more challenging following months of additional unabated tumor growth and disease progression[12,198]. In clinical management of advanced ovarian cancer, there is an urgent need to improve treatment selection by minimizing toxic side effects from ineffective chemotherapy options, as well as by predicting which first-line and second-line treatment options are likely to be efficacious against the patient's disease in advance of the current six-month clinical timeframe required to determine resistance to platinum-based chemotherapy[199,200]. Therefore, a rational follow-up study that aims to address these areas of clinical need would be to determine whether the population-level and individual organoid–level data acquired from HSLCI biomass measurements of ovarian cancer PDTOs can be retrospectively associated with clinical responses, including platinum-free interval following primary platinum-based therapy. Retrospective studies establishing correlations between HSLCI measurements of organoid biomass and relevant clinical outcomes, such as

platinum-free interval in the example of ovarian cancer, could subsequently result in prospective validation of biomarkers to guide treatment selection[1,2,18,25].

Advantageous capabilities in detecting and quantifying heterogeneity in organoid biomass, growth, and drug responses uniquely position HSLCI and the complete protocol described for a multitude of potential future applications not only in precision cancer medicine, but also as a powerful tool for basic and translational research. For example, through larger-scale high-throughput screening of organoid models representing a greater range of cancer etiologies, HSLCI could feasibly be used for drug discovery[21,141,175] while enabling consideration of organoid population and drug response heterogeneity measurements in lead compound identification. In previous work, HSLCI was used to identify a rare subpopulation of drug-resistant diffuse large B cell lymphoma cells from a population that was otherwise drug-sensitive, and a micropipette cell isolation system was demonstrated that enabled real-time isolation of cells of interest for continued culture, expansion, and further basic studies regarding mechanisms of drug resistance[73]. As the bioprinting procedure presented in this thesis enables growth of 3D-cultured organoids in a geometry that enables indexing across images, construction of such a micropipette-based isolation system for capturing bioprinted organoids of interest would enable individual drug-resistant organoids to be isolated and potentially re-cultured for analogous basic studies on the growth and evolution of 3D tumor models. Previous work has also demonstrated that QPI can quantitatively analyze cytotoxic interactions between 2D-cultured cancer cells and T cells[201,202]. Recently, a variety of more complex 3D-cultured organoid model systems have been developed that incorporate immune cells to model tumor-immune interactions, which are of interest for studying tumor immunology and testing the efficacy of immunotherapeutic approaches[19,25,179,203–206]. Further technical upgrades to the bioprinting, HSLCI imaging, or image analysis procedures could enable HSLCI to be used for high-throughput imaging and analysis of these model systems for basic and translational studies of growth, organoid drug responses, and

immune cell behavior. Further technical improvements could also conceivably increase the upper bound of the number of organoids imaged and tracked in an experiment by one order of magnitude, which in turn would provide even more opportunities to utilize the high-throughput measurements of changes in organoid biomass that are unique to this method, in both research and clinical contexts. While technical improvements will surely continue, the organoid screening pipeline presented in this work has already opened many new possibilities for studying 3D models of cancer, with the potential to provide a more comprehensive understanding of disease biology and to introduce evidence-based treatment options for more patients in need of them.

References

1. Letai, A., Bhola, P. & Welm, A. L. Functional precision oncology: Testing tumors with drugs to identify vulnerabilities and novel combinations. *Cancer Cell* **40**, 26–35 (2022).
2. Letai, A. Functional precision cancer medicine-moving beyond pure genomics. *Nat. Med.* **23**, 1028–1035 (2017).
3. Weinberg, R. A. *The Biology of Cancer*. (W.W. Norton & Company, 2013). doi:10.1201/9780429258794.
4. Tsimberidou, A. M., Fountzilas, E., Nikanjam, M. & Kurzrock, R. Review of precision cancer medicine: Evolution of the treatment paradigm. *Cancer Treat. Rev.* **86**, 102019 (2020).
5. Prasad, V., Fojo, T. & Brada, M. Precision oncology: origins, optimism, and potential. *Lancet Oncol.* **17**, e81–e86 (2016).
6. Brock, A. & Huang, S. Precision Oncology: Between Vaguely Right and Precisely Wrong. *Cancer Res.* **77**, 6473–6479 (2017).
7. Flaherty, K. T. *et al.* Molecular Landscape and Actionable Alterations in a Genomically Guided Cancer Clinical Trial: National Cancer Institute Molecular Analysis for Therapy Choice (NCI-MATCH). *J. Clin. Oncol. Off. J. Am. Soc. Clin. Oncol.* **38**, 3883–3894 (2020).
8. Marquart, J., Chen, E. Y. & Prasad, V. Estimation of the Percentage of US Patients With Cancer Who Benefit From Genome-Driven Oncology. *JAMA Oncol.* **4**, 1093 (2018).
9. Le Tourneau, C. *et al.* Molecularly targeted therapy based on tumour molecular profiling versus conventional therapy for advanced cancer (SHIVA): a multicentre, open-label, proof-of-concept, randomised, controlled phase 2 trial. *Lancet Oncol.* **16**, 1324–1334 (2015).
10. Rakha, E. A. & Pareja, F. G. New Advances in Molecular Breast Cancer Pathology. *Semin. Cancer Biol.* **72**, 102–113 (2021).

11. Meisel, J. L., Venur, V. A., Gnant, M. & Carey, L. Evolution of Targeted Therapy in Breast Cancer: Where Precision Medicine Began. *Am. Soc. Clin. Oncol. Educ. Book* 78–86 (2018) doi:10.1200/EDBK_201037.
12. Lheureux, S., Braunstein, M. & Oza, A. M. Epithelial ovarian cancer: Evolution of management in the era of precision medicine. *CA. Cancer J. Clin.* **69**, 280–304 (2019).
13. Kornauth, C. *et al.* Functional Precision Medicine Provides Clinical Benefit in Advanced Aggressive Hematologic Cancers and Identifies Exceptional Responders. *Cancer Discov.* **12**, 372–387 (2022).
14. Marusyk, A., Janiszewska, M. & Polyak, K. Intratumor Heterogeneity: The Rosetta Stone of Therapy Resistance. *Cancer Cell* **37**, 471–484 (2020).
15. Malani, D. *et al.* Implementing a Functional Precision Medicine Tumor Board for Acute Myeloid Leukemia. *Cancer Discov.* **12**, 388–401 (2022).
16. Lancaster, M. A. & Huch, M. Disease modelling in human organoids. *Dis. Model. Mech.* **12**, dmm039347 (2019).
17. Li, M. & Izpisua Belmonte, J. C. Organoids — Preclinical Models of Human Disease. *N. Engl. J. Med.* **380**, 569–579 (2019).
18. Schutgens, F. & Clevers, H. Human Organoids: Tools for Understanding Biology and Treating Diseases. *Annu. Rev. Pathol.* **15**, 211–234 (2020).
19. Zhao, Z. *et al.* Organoids. *Nat. Rev. Methods Primer* **2**, 94 (2022).
20. Al Shihabi, A. *et al.* Personalized chordoma organoids for drug discovery studies. *Sci. Adv.* **8**, eabl3674 (2022).
21. Langhans, S. A. Three-Dimensional in Vitro Cell Culture Models in Drug Discovery and Drug Repositioning. *Front. Pharmacol.* **9**, 6 (2018).
22. Lo, Y.-H., Karlsson, K. & Kuo, C. J. Applications of organoids for cancer biology and precision medicine. *Nat. Cancer* **1**, 761–773 (2020).

23. Tuveson, D. & Clevers, H. Cancer modeling meets human organoid technology. *Science* **364**, 952–955 (2019).

24. Porter, R. J., Murray, G. I. & McLean, M. H. Current concepts in tumour-derived organoids. *Br. J. Cancer* **123**, 1209–1218 (2020).

25. Veninga, V. & Voest, E. E. Tumor organoids: Opportunities and challenges to guide precision medicine. *Cancer Cell* **39**, 1190–1201 (2021).

26. Clevers, H. & Tuveson, D. A. Organoid Models for Cancer Research. *Annu. Rev. Cancer Biol.* **3**, 223–234 (2019).

27. Phan, N. *et al.* A simple high-throughput approach identifies actionable drug sensitivities in patient-derived tumor organoids. *Commun. Biol.* **2**, 78 (2019).

28. Al Shihabi, A. *et al.* The landscape of drug sensitivity and resistance in sarcoma. *Cell Stem Cell* **31**, 1524-1542.e4 (2024).

29. Wensink, G. E. *et al.* Patient-derived organoids as a predictive biomarker for treatment response in cancer patients. *Npj Precis. Oncol.* **5**, 30 (2021).

30. Edmondson, R., Broglie, J. J., Adcock, A. F. & Yang, L. Three-dimensional cell culture systems and their applications in drug discovery and cell-based biosensors. *Assay Drug Dev. Technol.* **12**, 207–218 (2014).

31. Simian, M. & Bissell, M. J. Organoids: A historical perspective of thinking in three dimensions. *J. Cell Biol.* **216**, 31–40 (2017).

32. Birgersdotter, A., Sandberg, R. & Ernberg, I. Gene expression perturbation in vitro—A growing case for three-dimensional (3D) culture systems. *Semin. Cancer Biol.* **15**, 405–412 (2005).

33. Pickl, M. & Ries, C. H. Comparison of 3D and 2D tumor models reveals enhanced HER2 activation in 3D associated with an increased response to trastuzumab. *Oncogene* **28**, 461–468 (2009).

34. Kodack, D. P. *et al.* Primary Patient-Derived Cancer Cells and Their Potential for Personalized Cancer Patient Care. *Cell Rep.* **21**, 3298–3309 (2017).
35. Dai, X., Cheng, H., Bai, Z. & Li, J. Breast Cancer Cell Line Classification and Its Relevance with Breast Tumor Subtyping. *J. Cancer* **8**, 3131–3141 (2017).
36. Kenny, P. A. *et al.* The morphologies of breast cancer cell lines in three-dimensional assays correlate with their profiles of gene expression. *Mol. Oncol.* **1**, 84–96 (2007).
37. Stock, K. *et al.* Capturing tumor complexity in vitro: Comparative analysis of 2D and 3D tumor models for drug discovery. *Sci. Rep.* **6**, 28951 (2016).
38. Nguyen, H. T. L. & Soragni, A. Patient-Derived Tumor Organoid Rings for Histologic Characterization and High-Throughput Screening. *STAR Protoc.* **1**, (2020).
39. Vlachogiannis, G. *et al.* Patient-derived organoids model treatment response of metastatic gastrointestinal cancers. *Science* **359**, 920–926 (2018).
40. Ooft, S. N. *et al.* Patient-derived organoids can predict response to chemotherapy in metastatic colorectal cancer patients. *Sci. Transl. Med.* **11**, eaay2574 (2019).
41. Yao, Y. *et al.* Patient-Derived Organoids Predict Chemoradiation Responses of Locally Advanced Rectal Cancer. *Cell Stem Cell* **26**, 17-26.e6 (2020).
42. Ganesh, K. *et al.* A rectal cancer organoid platform to study individual responses to chemoradiation. *Nat. Med.* **25**, 1607–1614 (2019).
43. de Witte, C. J. *et al.* Patient-Derived Ovarian Cancer Organoids Mimic Clinical Response and Exhibit Heterogeneous Inter- and Intrapatient Drug Responses. *Cell Rep.* **31**, 107762 (2020).
44. Lukonin, I., Zinner, M. & Liberali, P. Organoids in image-based phenotypic chemical screens. *Exp. Mol. Med.* **53**, 1495–1502 (2021).
45. Nguyen, T. L. *et al.* Quantitative Phase Imaging: Recent Advances and Expanding Potential in Biomedicine. *ACS Nano* **16**, 11516–11544 (2022).

46. Zangle, T. A. & Teitell, M. A. Live-cell mass profiling: an emerging approach in quantitative biophysics. *Nat. Methods* **11**, 1221–1228 (2014).

47. Majeed, H. *et al.* Quantitative phase imaging for medical diagnosis. *J. Biophotonics* **10**, 177–205 (2017).

48. Park, Y., Depeursinge, C. & Popescu, G. Quantitative phase imaging in biomedicine. *Nat. Photonics* **12**, 578–589 (2018).

49. Popescu, G. *et al.* Optical imaging of cell mass and growth dynamics. *Am. J. Physiol. Cell Physiol.* **295**, C538-544 (2008).

50. Barer, R., Ross, K. F. A. & Tkaczyk, S. Refractometry of Living Cells. *Nature* **171**, 720–724 (1953).

51. Barer, R. & Joseph, S. Refractometry of Living Cells : Part I. Basic Principles. *J. Cell Sci.* **s3-95**, 399–423 (1954).

52. Zhao, H., Brown, P. H. & Schuck, P. On the distribution of protein refractive index increments. *Biophys. J.* **100**, 2309–2317 (2011).

53. Davies, H. G. & Wilkins, M. H. F. Interference microscopy and mass determination. *Nature* **169**, 541 (1952).

54. Reed, J. *et al.* Rapid, Massively Parallel Single-Cell Drug Response Measurements via Live Cell Interferometry. *Biophys. J.* **101**, 1025–1031 (2011).

55. Cooper, K. L. *et al.* Multiple phases of chondrocyte enlargement underlie differences in skeletal proportions. *Nature* **495**, 375–378 (2013).

56. Mir, M., Bergamaschi, A., Katzenellenbogen, B. S. & Popescu, G. Highly Sensitive Quantitative Imaging for Monitoring Single Cancer Cell Growth Kinetics and Drug Response. *PLoS ONE* **9**, e89000 (2014).

57. Rappaz, B. *et al.* Noninvasive characterization of the fission yeast cell cycle by monitoring dry mass with digital holographic microscopy. *J. Biomed. Opt.* **14**, 034049 (2009).

58. Huang, D. *et al.* Identifying fates of cancer cells exposed to mitotic inhibitors by quantitative phase imaging. *The Analyst* **145**, 97–106 (2019).

59. Polanco, E. R. *et al.* Multiparametric quantitative phase imaging for real-time, single cell, drug screening in breast cancer. *Commun. Biol.* **5**, 794 (2022).

60. Vicar, T., Raudenska, M., Gumulec, J. & Balvan, J. The Quantitative-Phase Dynamics of Apoptosis and Lytic Cell Death. *Sci. Rep.* **10**, 1566 (2020).

61. Pavillon, N. *et al.* Early Cell Death Detection with Digital Holographic Microscopy. *PLoS ONE* **7**, e30912 (2012).

62. Jabs, J. *et al.* Screening drug effects in patient-derived cancer cells links organoid responses to genome alterations. *Mol. Syst. Biol.* **13**, 955 (2017).

63. Zhang, L. *et al.* Quantifying the drug response of patient-derived organoid clusters by aggregated morphological indicators with multi-parameters based on optical coherence tomography. *Biomed. Opt. Express* **14**, 1703–1717 (2023).

64. Gil, D. A., Deming, D. A. & Skala, M. C. Volumetric growth tracking of patient-derived cancer organoids using optical coherence tomography. *Biomed. Opt. Express* **12**, 3789–3805 (2021).

65. Gillette, A. A. *et al.* Autofluorescence Imaging of Treatment Response in Neuroendocrine Tumor Organoids. *Cancers* **13**, 1873 (2021).

66. Huang, D. *et al.* High-Speed Live-Cell Interferometry: A New Method for Quantifying Tumor Drug Resistance and Heterogeneity. *Anal. Chem.* **90**, 3299–3306 (2018).

67. Pu, Y. *et al.* Drug-tolerant persister cells in cancer: the cutting edges and future directions. *Nat. Rev. Clin. Oncol.* **20**, 799–813 (2023).

68. Recasens, A. & Munoz, L. Targeting Cancer Cell Dormancy. *Trends Pharmacol. Sci.* **40**, 128–141 (2019).

69. Vallette, F. M. *et al.* Dormant, quiescent, tolerant and persister cells: Four synonyms for the same target in cancer. *Biochem. Pharmacol.* **162**, 169–176 (2019).

70. Ramirez, M. *et al.* Diverse drug-resistance mechanisms can emerge from drug-tolerant cancer persister cells. *Nat. Commun.* **7**, 10690 (2016).

71. Murray, G. F. *et al.* Live Cell Mass Accumulation Measurement Non-Invasively Predicts Carboplatin Sensitivity in Triple-Negative Breast Cancer Patient-Derived Xenografts. *ACS Omega* **3**, 17687–17692 (2018).

72. Nguyen, H. T. L. *et al.* A rapid platform for 3D patient-derived cutaneous neurofibroma organoid establishment and screening. Preprint at https://doi.org/10.1101/2022.11.07.515469 (2022).

73. Murray, G. F., Guest, D., Mikheykin, A., Toor, A. & Reed, J. Single cell biomass tracking allows identification and isolation of rare targeted therapy-resistant DLBCL cells within a mixed population. *The Analyst* **146**, 1157–1162 (2021).

74. Saleh, T. *et al.* Tumor cell escape from therapy-induced senescence. *Biochem. Pharmacol.* **162**, 202–212 (2019).

75. Murray, G. F. *et al.* QPI Allows in vitro Drug Screening of Triple Negative Breast Cancer PDX Tumors and Fine Needle Biopsies. *Front. Phys.* **7**, 158 (2019).

76. Murray, G. F., Guest, D., Mikheykin, A., Toor, A. & Reed, J. Single cell biomass tracking allows identification and isolation of rare targeted therapy-resistant DLBCL cells within a mixed population. *The Analyst* **146**, 1157–1162 (2021).

77. Lampart, F. L., Iber, D. & Doumpas, N. Organoids in high-throughput and high-content screenings. *Front. Chem. Eng.* **5**, 1120348 (2023).

78. Sockell, A. *et al.* A microwell platform for high-throughput longitudinal phenotyping and selective retrieval of organoids. *Cell Syst.* **14**, 764-776.e6 (2023).

79. Bhola, P. D. *et al.* High-throughput dynamic BH3 profiling may quickly and accurately predict effective therapies in solid tumors. *Sci. Signal.* **13**, (2020).

80. Ma, Y.-S. *et al.* The power and the promise of organoid models for cancer precision medicine with next-generation functional diagnostics and pharmaceutical exploitation. *Transl. Oncol.* **14**, 101126 (2021).

81. Drost, J. & Clevers, H. Organoids in cancer research. *Nat. Rev. Cancer* **18**, 407–418 (2018).

82. Guillen, K. P. *et al.* A human breast cancer-derived xenograft and organoid platform for drug discovery and precision oncology. *Nat. Cancer* **3**, 232–250 (2022).

83. Tiriac, H. *et al.* Organoid Profiling Identifies Common Responders to Chemotherapy in Pancreatic Cancer. *Cancer Discov.* **8**, 1112–1129 (2018).

84. Sachs, N. *et al.* A Living Biobank of Breast Cancer Organoids Captures Disease Heterogeneity. *Cell* **172**, 373-386.e10 (2018).

85. Friedman, A. A. *et al.* Feasibility of Ultra-High-Throughput Functional Screening of Melanoma Biopsies for Discovery of Novel Cancer Drug Combinations. *Clin. Cancer Res.* **23**, 4680–4692 (2017).

86. Lam, S. S.-Y., He, A. B.-L. & Leung, A. Y.-H. Treatment of acute myeloid leukemia in the next decade – Towards real-time functional testing and personalized medicine. *Blood Rev.* **31**, 418–425 (2017).

87. Kapałczyńska, M. *et al.* 2D and 3D cell cultures – a comparison of different types of cancer cell cultures. *Arch. Med. Sci. AMS* **14**, 910–919 (2018).

88. Jensen, C. & Teng, Y. Is It Time to Start Transitioning From 2D to 3D Cell Culture? *Front. Mol. Biosci.* **7**, (2020).

89. Cheon, D.-J. & Orsulic, S. Mouse Models of Cancer. *Annu. Rev. Pathol. Mech. Dis.* **6**, 95–119 (2011).

90. Day, C.-P., Merlino, G. & Van Dyke, T. Preclinical mouse cancer models: a maze of opportunities and challenges. *Cell* **163**, 39–53 (2015).

91. Cekanova, M. & Rathore, K. Animal models and therapeutic molecular targets of cancer: utility and limitations. *Drug Des. Devel. Ther.* **8**, 1911–1922 (2014).

92. Bleijs, M., van de Wetering, M., Clevers, H. & Drost, J. Xenograft and organoid model systems in cancer research. *EMBO J.* **38**, e101654 (2019).

93. Al Shihabi, A. *et al.* The landscape of drug sensitivity and resistance in sarcoma. Preprint at https://doi.org/10.1101/2023.05.25.542375 (2023).

94. Mazzocchi, A., Soker, S. & Skardal, A. 3D bioprinting for high-throughput screening: Drug screening, disease modeling, and precision medicine applications. *Appl. Phys. Rev.* **6**, 011302 (2019).

95. Daly, A. C., Prendergast, M. E., Hughes, A. J. & Burdick, J. A. Bioprinting for the Biologist. *Cell* **184**, 18–32 (2021).

96. Mao, S. *et al.* Bioprinting of in vitro tumor models for personalized cancer treatment: a review. *Biofabrication* **12**, 042001 (2020).

97. Kang, Y., Datta, P., Shanmughapriya, S. & Ozbolat, I. T. 3D Bioprinting of Tumor Models for Cancer Research. *ACS Appl. Bio Mater.* **3**, 5552–5573 (2020).

98. Liu, T., Delavaux, C. & Zhang, Y. S. 3D bioprinting for oncology applications. *J. 3D Print. Med.* **3**, 55–58 (2019).

99. Yi, H.-G. Introduction to bioprinting of in vitro cancer models. *Essays Biochem.* (2021) doi:10.1042/EBC20200104.

100. Bon, P., Maucort, G., Wattellier, B. & Monneret, S. Quadriwave lateral shearing interferometry for quantitative phase microscopy of living cells. *Opt. Express* **17**, 13080–13094 (2009).

101. Murray, G. *et al.* Application of Quantitative Phase Imaging mass accumulation measurements to research and clinical problems in cancer. in *Quantitative Phase Imaging V* (eds. Popescu, G. & Park, Y.) 49 (SPIE, San Francisco, United States, 2019). doi:10.1117/12.2514597.

102. Barer, R. Interference Microscopy and Mass Determination. *Nature* **169**, 366–367 (1952).

103. Ross, K. F. A. *Phase Contrast and Interference Microscopy for Cell Biologists*. (Edward Arnold, 1967).

104. Barer, R. & Tkaczyk, S. Refractive Index of Concentrated Protein Solutions. *Nature* **173**, 821–822 (1954).

105. Chun, J. *et al.* Rapidly quantifying drug sensitivity of dispersed and clumped breast cancer cells by mass profiling. *The Analyst* **137**, 5495 (2012).

106. Alam, A. U., Howlader, M. M. R. & Deen, M. J. The effects of oxygen plasma and humidity on surface roughness, water contact angle and hardness of silicon, silicon dioxide and glass. *J. Micromechanics Microengineering* **24**, 035010 (2014).

107. Nair, K. *et al.* Characterization of cell viability during bioprinting processes. *Biotechnol. J.* **4**, 1168–1177 (2009).

108. Boularaoui, S., Al Hussein, G., Khan, K. A., Christoforou, N. & Stefanini, C. An overview of extrusion-based bioprinting with a focus on induced shear stress and its effect on cell viability. *Bioprinting* **20**, e00093 (2020).

109. Szymański, P., Markowicz, M. & Mikiciuk-Olasik, E. Adaptation of High-Throughput Screening in Drug Discovery—Toxicological Screening Tests. *Int. J. Mol. Sci.* **13**, 427–452 (2011).

110. Miles, B. & Lee, P. L. Achieving Reproducibility and Closed-Loop Automation in Biological Experimentation with an IoT-Enabled Lab of the Future. *SLAS Technol. Transl. Life Sci. Innov.* **23**, 432–439 (2018).

111. Kroll, T. *et al.* Molecular characterization of breast cancer cell lines by expression profiling. *J. Cancer Res. Clin. Oncol.* **128**, 125–134 (2002).

112. Comşa, Ş., Cîmpean, A. M. & Raica, M. The Story of MCF-7 Breast Cancer Cell Line: 40 years of Experience in Research. *Anticancer Res.* **35**, 3147–3154 (2015).

113. Lee, A. V., Oesterreich, S. & Davidson, N. E. MCF-7 Cells—Changing the Course of Breast Cancer Research and Care for 45 Years. *JNCI J. Natl. Cancer Inst.* **107**, (2015).

114. Ayoub, N. M., Ibrahim, D. R., Alkhalifa, A. E. & Al-Husein, B. A. Crizotinib induced antitumor activity and synergized with chemotherapy and hormonal drugs in breast cancer cells via downregulating MET and estrogen receptor levels. *Invest. New Drugs* **39**, 77–88 (2021).

115. Bush, S. J., Chen, L., Tovar-Corona, J. M. & Urrutia, A. O. Alternative splicing and the evolution of phenotypic novelty. *Philos. Trans. R. Soc. B Biol. Sci.* **372**, 20150474 (2017).

116. Liu, Y. *et al.* Impact of Alternative Splicing on the Human Proteome. *Cell Rep.* **20**, 1229–1241 (2017).

117. Climente-González, H., Porta-Pardo, E., Godzik, A. & Eyras, E. The Functional Impact of Alternative Splicing in Cancer. *Cell Rep.* **20**, 2215–2226 (2017).

118. Chuang, T.-J. *et al.* Integrative transcriptome sequencing reveals extensive alternative trans-splicing and cis-backsplicing in human cells. *Nucleic Acids Res.* **46**, 3671–3691 (2018).

119. Ronneberger, O., Fischer, P. & Brox, T. U-Net: Convolutional Networks for Biomedical Image Segmentation. in *Medical Image Computing and Computer-Assisted Intervention – MICCAI 2015* (eds. Navab, N., Hornegger, J., Wells, W. M. & Frangi, A. F.) 234–241 (Springer International Publishing, Cham, 2015). doi:10.1007/978-3-319-24574-4_28.

120. He, K., Zhang, X., Ren, S. & Sun, J. Deep Residual Learning for Image Recognition. in 770–778 (2016).

121. Barer, R. & Ross, K. F. A. Refractometry of living cells. *J. Physiol.* **118**, 38P-39P (1952).

122. Ershov, D. *et al.* Bringing TrackMate into the era of machine-learning and deep-learning. 2021.09.03.458852 Preprint at https://doi.org/10.1101/2021.09.03.458852 (2021).

123. TrackMate: An open and extensible platform for single-particle tracking - ScienceDirect. https://www.sciencedirect.com/science/article/pii/S1046202316303346.

124. Chen, T. & Guestrin, C. XGBoost: A Scalable Tree Boosting System. in *Proceedings of the 22nd ACM SIGKDD International Conference on Knowledge Discovery and Data Mining* 785–794 (Association for Computing Machinery, New York, NY, USA, 2016). doi:10.1145/2939672.2939785.

125. Tamaoki, T. *et al.* Staurosporine, a potent inhibitor of phospholipidCa++dependent protein kinase. *Biochem. Biophys. Res. Commun.* **135**, 397–402 (1986).

126. Feldinger, K. & Kong, A. Profile of neratinib and its potential in the treatment of breast cancer. *Breast Cancer Targets Ther.* **7**, 147–162 (2015).

127. Johnston, S. R. D. & Leary, A. Lapatinib: a novel EGFR/HER2 tyrosine kinase inhibitor for cancer. *Drugs Today Barc. Spain 1998* **42**, 441–453 (2006).

128. Liston, D. R. & Davis, M. Clinically Relevant Concentrations of Anticancer Drugs: A Guide for Nonclinical Studies. *Clin. Cancer Res.* **23**, 3489–3498 (2017).

129. Keyvanjah, K. *et al.* Pharmacokinetics of neratinib during coadministration with lansoprazole in healthy subjects. *Br. J. Clin. Pharmacol.* **83**, 554–561 (2017).

130. Park, J. J. H., Hsu, G., Siden, E. G., Thorlund, K. & Mills, E. J. An overview of precision oncology basket and umbrella trials for clinicians. *CA. Cancer J. Clin.* **70**, 125–137 (2020).

131. Senft, D., Leiserson, M. D. M., Ruppin, E. & Ronai, Z. A. Precision Oncology: The Road Ahead. *Trends Mol. Med.* **23**, 874–898 (2017).

132. Schwartzberg, L., Kim, E. S., Liu, D. & Schrag, D. Precision Oncology: Who, How, What, When, and When Not? *Am. Soc. Clin. Oncol. Educ. Book* 160–169 (2017) doi:10.1200/EDBK_174176.

133. Morgan, G., Aftimos, P. & Awada, A. Current-day precision oncology: from cancer prevention, screening, drug development, and treatment – have we fallen short of the promise? *Curr. Opin. Oncol.* **28**, 441–446 (2016).

134. Xu, R., Zhou, X., Wang, S. & Trinkle, C. Tumor organoid models in precision medicine and investigating cancer-stromal interactions. *Pharmacol. Ther.* **218**, 107668 (2021).

135. Kane, K. I. W. *et al.* Determination of the rheological properties of Matrigel for optimum seeding conditions in microfluidic cell cultures. *AIP Adv.* **8**, 125332 (2018).

136. Hospodiuk, M., Dey, M., Sosnoski, D. & Ozbolat, I. T. The bioink: A comprehensive review on bioprintable materials. *Biotechnol. Adv.* **35**, 217–239 (2017).

137. Zangle, T. A., Teitell, M. A. & Reed, J. Live Cell Interferometry Quantifies Dynamics of Biomass Partitioning during Cytokinesis. *PLoS ONE* **9**, e115726 (2014).

138. Reed, J. *et al.* Live Cell Interferometry Reveals Cellular Dynamism During Force Propagation. *ACS Nano* **2**, 841–846 (2008).

139. Reed, J. *et al.* High throughput cell nanomechanics with mechanical imaging interferometry. *Nanotechnology* **19**, 235101 (2008).

140. Ledwig, P. & Robles, F. E. Epi-mode tomographic quantitative phase imaging in thick scattering samples. *Biomed. Opt. Express* **10**, 3605–3621 (2019).

141. Wardwell-Swanson, J. *et al.* A Framework for Optimizing High-Content Imaging of 3D Models for Drug Discovery. *SLAS Discov.* **25**, 709–722 (2020).

142. Kwee, E., Peterson, A., Halter, M. & Elliott, J. Practical application of microsphere samples for benchmarking a quantitative phase imaging system. *Cytometry A* **99**, 1022–1032 (2021).

143. Brassard, J. A., Nikolaev, M., Hübscher, T., Hofer, M. & Lutolf, M. P. Recapitulating macro-scale tissue self-organization through organoid bioprinting. *Nat. Mater.* **20**, 22–29 (2021).

144. Lawlor, K. T. *et al.* Cellular extrusion bioprinting improves kidney organoid reproducibility and conformation. *Nat. Mater.* **20**, 260–271 (2021).

145. Jiang, S. *et al.* An Automated Organoid Platform with Inter-organoid Homogeneity and Inter-patient Heterogeneity. *Cell Rep. Med.* **1**, 100161 (2020).

146. Swaminathan, S., Hamid, Q., Sun, W. & Clyne, A. M. Bioprinting of 3D breast epithelial spheroids for human cancer models. *Biofabrication* **11**, 025003 (2019).

147. Martelotto, L. G., Ng, C. K., Piscuoglio, S., Weigelt, B. & Reis-Filho, J. S. Breast cancer intra-tumor heterogeneity. *Breast Cancer Res.* **16**, 210 (2014).

148. Stanta, G. & Bonin, S. Overview on Clinical Relevance of Intra-Tumor Heterogeneity. *Front. Med.* **5**, (2018).

149. Dentro, S. C. *et al.* Characterizing genetic intra-tumor heterogeneity across 2,658 human cancer genomes. *Cell* **184**, 2239-2254.e39 (2021).

150. Espiritu, S. M. G. *et al.* The Evolutionary Landscape of Localized Prostate Cancers Drives Clinical Aggression. *Cell* **173**, 1003-1013.e15 (2018).

151. Somasundaram, R., Villanueva, J. & Herlyn, M. Chapter Eleven - Intratumoral Heterogeneity as a Therapy Resistance Mechanism: Role of Melanoma Subpopulations. in *Advances in Pharmacology* (ed. Smalley, K. S. M.) vol. 65 335–359 (Academic Press, 2012).

152. Auffinger, B., Spencer, D., Pytel, P., Ahmed, A. U. & Lesniak, M. S. The role of glioma stem cells in chemotherapy resistance and glioblastoma multiforme recurrence. *Expert Rev. Neurother.* **15**, 741–752 (2015).

153. Lacerda, L., Pusztai, L. & Woodward, W. A. The role of tumor initiating cells in drug resistance of breast cancer: Implications for future therapeutic approaches. *Drug Resist. Updat.* **13**, 99–108 (2010).

154. Choo, N. *et al.* High-Throughput Imaging Assay for Drug Screening of 3D Prostate Cancer Organoids. *SLAS Discov.* **26**, 1107–1124 (2021).

155. Matthews, J. M. *et al.* OrganoID: A versatile deep learning platform for tracking and analysis of single-organoid dynamics. *PLoS Comput. Biol.* **18**, e1010584 (2022).

156. Chen, S., Zhou, Y., Chen, Y. & Gu, J. fastp: an ultra-fast all-in-one FASTQ preprocessor. *Bioinforma. Oxf. Engl.* **34**, i884–i890 (2018).

157. Dobin, A. *et al.* STAR: ultrafast universal RNA-seq aligner. *Bioinformatics* **29**, 15–21 (2013).

158. Auwera, G. A. V. der & O'Connor, B. D. *Genomics in the Cloud: Using Docker, GATK, and WDL in Terra*. (O'Reilly Media, Incorporated, 2020).

159. Sayols, S., Scherzinger, D. & Klein, H. dupRadar: a Bioconductor package for the assessment of PCR artifacts in RNA-Seq data. *BMC Bioinformatics* **17**, 428 (2016).

160. Li, B. & Dewey, C. N. RSEM: accurate transcript quantification from RNA-Seq data with or without a reference genome. *BMC Bioinformatics* **12**, 323 (2011).

161. Shen, S. *et al.* rMATS: Robust and flexible detection of differential alternative splicing from replicate RNA-Seq data. *Proc. Natl. Acad. Sci.* **111**, E5593–E5601 (2014).

162. Lo Giudice, C., Tangaro, M. A., Pesole, G. & Picardi, E. Investigating RNA editing in deep transcriptome datasets with REDItools and REDIportal. *Nat. Protoc.* **15**, 1098–1131 (2020).

163. Nicorici, D. *et al.* FusionCatcher – a tool for finding somatic fusion genes in paired-end RNA-sequencing data. *bioRxiv* 011650 (2014) doi:10.1101/011650.

164. P'ng, C. *et al.* BPG: Seamless, automated and interactive visualization of scientific data. *BMC Bioinformatics* **20**, 42 (2019).

165. Poplin, R. *et al.* Scaling accurate genetic variant discovery to tens of thousands of samples. 201178 Preprint at https://doi.org/10.1101/201178 (2018).

166. Cleary, J. G. *et al.* Comparing Variant Call Files for Performance Benchmarking of Next-Generation Sequencing Variant Calling Pipelines. 023754 Preprint at https://doi.org/10.1101/023754 (2015).

167. Davies, H. G. & Wilkins, M. H. F. Interference microscopy and mass determination. *Nature* **169**, 541 (1952).

168. Popescu, G. *et al.* Optical imaging of cell mass and growth dynamics. *Am. J. Physiol. Cell Physiol.* **295**, C538-544 (2008).

169. Deng, J. *et al.* ImageNet: A large-scale hierarchical image database. in *2009 IEEE Conference on Computer Vision and Pattern Recognition* 248–255 (2009). doi:10.1109/CVPR.2009.5206848.

170. Tebon, P., Wang, B. & Gonzalez, A. E. uclahs-soragnilab/hslci_pipeline: Release for Zenodo. Zenodo https://doi.org/10.5281/ZENODO.7787339 (2023).

171. Nguyen, H. T. L. *et al.* A platform for rapid patient-derived cutaneous neurofibroma organoid establishment and screening. *Cell Rep. Methods* **4**, 100772 (2024).

172. Liu, X., Oh, S., Peshkin, L. & Kirschner, M. W. Computationally enhanced quantitative phase microscopy reveals autonomous oscillations in mammalian cell growth. *Proc. Natl. Acad. Sci.* **117**, 27388–27399 (2020).

173. Murphy, S. V. & Atala, A. 3D bioprinting of tissues and organs. *Nat. Biotechnol.* **32**, 773–785 (2014).

174. Tebon, P. *et al.* Drug screening at single-organoid resolution via bioprinting and interferometry. *Nat Commun* (2023).

175. Mergenthaler, P. *et al.* Rapid 3D phenotypic analysis of neurons and organoids using data-driven cell segmentation-free machine learning. *PLOS Comput. Biol.* **17**, e1008630 (2021).

176. Ershov, D. *et al.* TrackMate 7: integrating state-of-the-art segmentation algorithms into tracking pipelines. *Nat. Methods* **19**, 829–832 (2022).

177. Tinevez, J.-Y. *et al.* TrackMate: An open and extensible platform for single-particle tracking. *Methods* **115**, 80–90 (2017).

178. Le Compte, M. *et al.* Single-organoid analysis reveals clinically relevant treatment-resistant and invasive subclones in pancreatic cancer. *Npj Precis. Oncol.* **7**, 128 (2023).

179. Dekkers, J. F. *et al.* Uncovering the mode of action of engineered T cells in patient cancer organoids. *Nat. Biotechnol.* **41**, 60–69 (2023).

180. Borten, M. A., Bajikar, S. S., Sasaki, N., Clevers, H. & Janes, K. A. Automated brightfield morphometry of 3D organoid populations by OrganoSeg. *Sci. Rep.* **8**, 5319 (2018).

181. Lee, S. *et al.* High-throughput formation and image-based analysis of basal-in mammary organoids in 384-well plates. *Sci. Rep.* **12**, 317 (2022).

182. Lin, S., Schorpp, K., Rothenaigner, I. & Hadian, K. Image-based high-content screening in drug discovery. *Drug Discov. Today* **25**, 1348–1361 (2020).

183. Booij, T. H., Price, L. S. & Danen, E. H. J. 3D Cell-Based Assays for Drug Screens: Challenges in Imaging, Image Analysis, and High-Content Analysis. *SLAS Discov.* **24**, 615–627 (2019).

184. Wang, F. *et al.* Organoid bioinks: construction and application. *Biofabrication* **16**, 032006 (2024).

185. Crocker, J. C. & Grier, D. G. Methods of Digital Video Microscopy for Colloidal Studies. *J. Colloid Interface Sci.* **179**, 298–310 (1996).

186. Harbeck, N. *et al.* Breast cancer. *Nat. Rev. Dis. Primer* **5**, 66 (2019).

187. Hill, S. J. *et al.* Prediction of DNA Repair Inhibitor Response in Short-Term Patient-Derived Ovarian Cancer Organoids. *Cancer Discov.* **8**, 1404–1421 (2018).

188. Blom, K., Nygren, P., Larsson, R. & Andersson, C. R. Predictive Value of Ex Vivo Chemosensitivity Assays for Individualized Cancer Chemotherapy: A Meta-Analysis. *SLAS Technol.* **22**, 306–314 (2017).

189. Kamiloglu, S., Sari, G., Ozdal, T. & Capanoglu, E. Guidelines for cell viability assays. *Food Front.* **1**, 332–349 (2020).

190. Sharma, S. V. *et al.* A chromatin-mediated reversible drug-tolerant state in cancer cell subpopulations. *Cell* **141**, 69–80 (2010).

191. Devaud, N. *et al.* Leiomyosarcoma. *Surg. Oncol. Clin. N. Am.* **31**, 527–546 (2022).

192. Serrano, C. & George, S. Leiomyosarcoma. *Hematol. Oncol. Clin. North Am.* **27**, 957–974 (2013).

193. Spalato-Ceruso, M., Ghazzi, N. E. & Italiano, A. New strategies in soft tissue sarcoma treatment. *J. Hematol. Oncol.J Hematol Oncol* **17**, 76 (2024).

194. Belayneh, R., Fourman, M. S., Bhogal, S. & Weiss, K. R. Update on Osteosarcoma. *Curr. Oncol. Rep.* **23**, 71 (2021).

195. Fritsch, C. *et al.* Characterization of the Novel and Specific PI3Kα Inhibitor NVP-BYL719 and Development of the Patient Stratification Strategy for Clinical Trials. *Mol. Cancer Ther.* **13**, 1117–1129 (2014).

196. André, F. *et al.* Alpelisib for PIK3CA-Mutated, Hormone Receptor–Positive Advanced Breast Cancer. *N. Engl. J. Med.* **380**, 1929–1940 (2019).

197. Lheureux, S., Gourley, C., Vergote, I. & Oza, A. M. Epithelial ovarian cancer. *Lancet Lond. Engl.* **393**, 1240–1253 (2019).

198. Berek, J. S., Renz, M., Kehoe, S., Kumar, L. & Friedlander, M. Cancer of the ovary, fallopian tube, and peritoneum: 2021 update. *Int. J. Gynaecol. Obstet. Off. Organ Int. Fed. Gynaecol. Obstet.* **155 Suppl 1**, 61–85 (2021).

199. Sisman, Y., Schnack, T., Høgdall, E. & Høgdall, C. Organoids and epithelial ovarian cancer - a future tool for personalized treatment decisions? (Review). *Mol. Clin. Oncol.* **16**, 29 (2022).

200. Nero, C. *et al.* Patient-derived organoids and high grade serous ovarian cancer: from disease modeling to personalized medicine. *J. Exp. Clin. Cancer Res. CR* **40**, 116 (2021).

201. Zangle, T. A., Burnes, D., Mathis, C., Witte, O. N. & Teitell, M. A. Quantifying Biomass Changes of Single CD8+ T Cells during Antigen Specific Cytotoxicity. *PLoS ONE* **8**, e68916 (2013).

202. Kim, D. N. H., Lim, A. A. & Teitell, M. A. Rapid, label-free classification of tumor-reactive T cell killing with quantitative phase microscopy and machine learning. *Sci. Rep.* **11**, 19448 (2021).

203. Schnalzger, T. E. *et al.* 3D model for CAR-mediated cytotoxicity using patient-derived colorectal cancer organoids. *EMBO J.* **38**, e100928 (2019).

204. Neal, J. T. *et al.* Organoid Modeling of the Tumor Immune Microenvironment. *Cell* **175**, 1972-1988.e16 (2018).

205. Dijkstra, K. K. *et al.* Generation of Tumor-Reactive T Cells by Co-culture of Peripheral Blood Lymphocytes and Tumor Organoids. *Cell* **174**, 1586-1598.e12 (2018).

206. Chalabi, M. *et al.* Neoadjuvant immunotherapy leads to pathological responses in MMR-proficient and MMR-deficient early-stage colon cancers. *Nat. Med.* **26**, 566–576 (2020).